ABSTRACT

Title of Dissertation: ADSORPTION HUMIDITY EFFECTS, MICROPARTICLE RATE BEHAVIOR AND THERMAL SWING ADSORPTION

John J. Mahle, Doctor of Philosophy, 2005

Dissertation Directed by: Professor Michael Harris
Department of Chemical Engineering
Purdue University

Application of adsorption processes for air purification requires an approach, which accounts for the presence of humidity. Four separate but related studies are conducted to examine the adsorption processes.

A new pure component adsorption isotherm is developed to describe Type 5 adsorption. The results are used to correlate data of water on activated carbon. This model derives from the concept that capillary condensation accounts for Type 5 behavior and is strongly dependent on the pore size distribution. The new model has the advantage over all other prior models of being invertible in terms of loading and partial pressure. The Henry's law limit and heat of adsorption effects are discussed.

A study of coadsorption of water and immiscible organics is also presented. Data for the system chloroethane water on two activated carbons is measured. A new coadsorption model is developed to describe immiscible vapors and water. This model has the advantage of at most one adjustable parameter and can also be solved without

iteration. Good agreement is demonstrated between this new model, data measured here and literature data.

The use of thermal swing adsorption for air purification is examined in this work. An experimental system is used to perform cycling experiments under dry and humid conditions. A dynamic simulation model is developed to describe several of cycling runs. Using the coadsorption model developed above the good agreement is found between the data and simulation profiles. Optimization of cycle parameters was investigated to show that some moderation of the feed water content is required to obtain high purification of a light vapor challenge at ambient temperature conditions.

The internal rate effects of commercial adsorbents have been reported in the literature. There is seldom an attempt to review the many approaches. Data was measured using a gravimetric technique for chloroethane and hexane on BPL activated carbon and 13X molecular sieve. A distributed parameter micropore diffusion model was solved to simulate this data. Regression of the adsorption and desorption data was used to determined micropore diffusion coefficients. These values were shown to compare well with literature values.

Adsorption Humidity Effects, Microparticle Rate Behavior and Thermal Swing Adsorption

by

John J. Mahle

Dissertation submitted to the Faculty of the Graduate School of the
University of Maryland, College Park in partial fulfillment
of the requirements for the degree of
Doctor of Philosophy 2005

Advisory Committee:

Professor Timothy Barbari, Chair
Professor Michael Harris
Professor Sheryl Ehrman
Professor Allan Davis
Professor M. Douglas Levan

Acknowledgements

I would like to thank many for assistance:

- My wife Caroline for encouragement and patience.
- My children Mandy, Lacey, Perry and Campbell for inspiration.
- My advisor Prof. Michael Harris your positive attitude toward all my efforts was most helpful. My regret is not being in closer contact.
- Prof. Timothy Barbari for providing support in navigating the program.
- Prof. M. Douglas LeVan for encouraging comments about relevance of this work.
- My coworkers Len Buettner, and Chris Karwacki for discussions and assistance. David Friday for discussion on all things TSA.

Table of Contents

Table of Figures

Table of Tables

List of Symbols

Adsorption Equilibrium Model for Type 5 Isotherms

A	isotherm centering parameter	
B	isotherm width parameter	
b	function width distribution parameter	
D	parameter defined in equation (2.11)	
H	Henry's law limit	
k	function centering distribution parameter	
N	number of data points	
n	adsorbed phase concentration	mol/wt
P	parameter value	
p	pressure	
p*	relative pressure	
R	gas constant	
r	radius	
T	temperature	K
V	volume	
V_m	molar volume	
x	independent distribution parameter	
y	dependent distribution parameter	

Greek Letters

γ	surface tension
δ	parameter sensitivity

η	deviation variable	

Subscripts

base	evaluated at base case condition	
diff	differential enthalpy	
exp	experimentally determined	
model	model determined	
new	evaluated at new condition	
s	saturated value	
vap	vaporization	

Superscripts

*	saturated	

Coadsorption Equilibria for Immiscible Vapors

A	Area term Gibbs isotherm	
n	solid phase concentration	mol/kg
E	potential theory energy	
F	free energy term	
$F_{hysteresis}$	water hysteresis function	
G	Gibb's energy	
H	enthalpy	
K	linear isotherm parameter	
p	partial pressure	
R	gas constant	
S_i	entropy	

T	temperature	K
U	internal energy	
V	volume adsorbed eqn 3.9	
W	potential theory adsorbed volume	
x	enthalpy fraction	

Greek letters

δ_{Dev}	deviation difference variable
ε	adsorption potential
β	potential theory parameter
Γ	Gibbs isotherm parameter
θ	dimensionless adsorbed phase loading
μ_i	chemical potential
π	spreading pressure
σ	summation deviation variable
ϕ	enthalpy ratio
ϕ'	surface potential
Ψ	fractional loading term equation (3.9)

Subscripts

ads	adsorbed
w	water
pure	pure component term
o	volume saturation
mix	mixture term

Superscripts

int	integrated value	

Studies of Temperature Swing Adsorption

A	cross-sectional area column	
C	total concentration	
C_i	fluid phase concentration	mol/volume
C_p	heat capacity	
C_t	integrated concentration	
D_c	surface diffusion coefficient	
D_m	molecular diffusivity	
E	activation energy equation (5.17)	
h	fluid phase enthalpy	
ha	particle heat transfer coefficient	
k_f	particle film coefficient	
L	length	
M	component mass of a stream	
N	molar flux	
N_{Re}	Reynolds number	
N_{Sc}	Schmidt number	
n	adsorbed phase concentration	mol/wt
P	pressure	
Pe	Peclet number	
R	gas constant	

R_P	particle radius	
S	energy source term	
T	temperature	K
t	time	
U	internal energy	
y_i	fluid phase mole fraction	
z	axial length	m
v	fluid phase velocity	

Greek letters

Δ	difference from experiment replicates	
δ	simulation parameter sensitivity	
ε	porosity	
λ	heat of adsorption	
ρ_b	bed density	kg/m3
τ	dimensionless time	
ϕ	purge to product mass flowrate ratio	

Subscripts

c	chemical
ref	at reference temperature

Particle Scale Transport

$\overline{\overline{A}}$	collocation matrix for first derivative
$\overline{\overline{B}}$	collocation matrix for first derivative
a	adsorbed phase chemical activity

B	inverted matrix of surface mobilities	
C_i	fluid phase concentration	mol/volume
cp	heat capacity	
D_K	Knudsen diffusion coefficient	
D_m	molecular diffusion coefficient	
D_p	macropore diffusion coefficient	
E	potential theory energy	
h_f	particle film heat transfer coefficient	
J	molar flux	
k_f	particle film mass transfer coefficient	
MW	molecular weight	
m	mass of adsorbent	
N_{Nu}	Nusselt number	
N_{Pr}	Prandtl number	
N_{Re}	Reynolds number	
N_{Sc}	Schmidt number	
Q	volumetric fluid flowrate	
q	heat flux	
N	molar flux	
R_g	gas constant	
T	temperature	K
t	time	
V	volume of basket	

v	fluid phase velocity	
y_i	fluid phase mole fraction	

Greek letters

β	concentration dependent parameter	
Γ	thermodynamic term equation 5.21	
δ	parameter sensitivity	
ε	porosity	
η	deviation variable	
κ	Darcy's law parameter equation (5.15)	
λ	heat of adsorption	
μ	Darcy's law parameter	
ρ_p	particle density	kg/m3
τ	particle shape factor	

Subscripts

trans	transport diffusivity	
o	zero loading diffusivity	

Chapter 1: Introduction

Air purification applications are associated with removal of trace contaminants from air streams. This is a classic example of a separation process. Typically high levels of separation in gas phase processes can be achieved with modest power demand through the use of physical adsorption processes.

Chapter 2 describes the development of a novel adsorption equilibria expression for Type 5 behavior. The most often considered example of Type 5 behavior is water adsorption on carbonaceous materials. All prior reported analytical expressions make use of implicit determination. It would be desirable to have an expression, which is both accurate and explicit in terms of partial pressure and loading.

Recently data has been reported on the multicomponent adsorption behavior for coadsorbed water and organics. A limited number of theoretical and empirical models have been proposed to describe such systems. Immiscible mixtures offer extreme challenges to most models. Chapter 3 details a proposed semi-empirical model to describe non-ideal coadsorption of immiscible mixtures.

Numerous industrial examples exist of thermal regeneration based adsorption applications. Cyclic behavior allows near indefinite operation under steady state conditions. There are limits to the cyclic behavior, which must be considered especially when rapid cycling is required. An analysis and parametric study of cyclic thermal swing filtration is presented in Chapter 4.

The modeling of adsorption systems for high purification levels requires knowledge of the mass transfer behavior. A review of the particle scale behavior is

examined through gravimetric experiments and modeling to identify meaningful diffusion coefficients and discuss these relative to literature values.

Chapter 2: An Adsorption Equilibrium Model for Type 5 Isotherms

2.1 Introduction

Physical adsorption of gases and vapors on porous adsorbents is influenced by several factors. Perhaps the most important among these are the adsorbate-adsorbent interaction energy, and pore size distribution. Strong adsorbate-adsorbent attractive forces favor high surface coverage consistent with Type 1 isotherms. For the case where adsorbate-adsorbate interaction is favored over adsorbate-adsorbent interactions, low surface coverage occurs until the capillary condensation effects lead to adsorption at high relative pressure as characterized by Type 5 isotherms. Adsorbate-adsorbent pairs with moderate interaction energy can display a combination of these behaviors. The pore size distribution effect can be significant for both molecular sieving as well as critical molecular cluster formation.

Recently, Brennan (2001) presented a review of water adsorption on activated carbon. The mechanism of adsorption is discussed in regard to previous experimental and molecular modeling studies. The experimental work cited included spectroscopic and surface chemistry measurements that were used to quantify functional groups and to analyze the pore geometry. Strong self-association of water due to hydrogen bonding limits adsorption on graphite surfaces. Water condensation is stabilized by the formation of clusters or oligomers in the liquid phase. In small pores there are geometric constraints on the oligomer formation, which limits the adsorption until high relative pressure is obtained. At low coverage, water adsorption on carbon surfaces is governed by polar site interactions. Specifically surface oxide sites are the dominant species, which allow H-bond formation with the surface. The various methods to measure this site density are

discussed. Rutherford (2003) proposed an implicit, isothermal analytical site model to describe Type 2 and Type 5 behavior.

Many of these fundamental observations have been used as a basis for molecular modeling of Type 5 adsorption. Brennan (2001) and McCallum (1999) describe several of these studies. These models consider a two-phase fluid which while descriptive does not reduce to a simple analytical solution. A less well studied yet significant aspect of Type 5 equilibria are hysteresis effects. A description of this behavior was provided by Mann (1995) through the use of network models. The observed hysteresis for water adsorption on activated carbon was shown to be consistent with a two-dimensional network modeled using the Kelvin equation. Both an increased interconnectivity and increased breadth of the distribution of pores were shown to result in an increase of the size of the hysteresis loop.

Engineering and design calculations of adsorption systems are aided by accurate descriptions of adsorption equilibrium. Typically measured data is correlated to two or three-term expressions, which can be solved explicitly or numerically. The resulting correlation allows for interpolation over the whole range of measured data. In addition if the adsorption equilibrium expression obeys the correct saturation and zero coverage limits, then extrapolation over the entire partial pressure and loading range is possible. The equilibrium expressions, most useful for the design models, are those that can be inverted i.e. be written explicitly in terms of either partial pressure or adsorbed phase loading. This allows for more stable and rapid adsorption equilibria calculations. While many adsorption equilibrium expressions have been proposed no widely accepted model has been found for Type 5 equilibrium that satisfies these criteria.

Several of the analytical models of Type 5 behavior have been formulated using a kinetic framework similar to the BET model, Gregg and Sing (1982). Dubinin and Serpinski (1981) developed an expression of Type 5 behavior, which is implicit in loading with parameters that correspond to the surface oxide site density. Barton et al. (1992) proposed an extension of this model for systems with very steep transitions. Using kinetic arguments consistent with association theory Talu and Meunier (2001) developed an expression for Type 1 and Type 5 isotherms that is also implicit in adsorbed phase loading. Parameter values are related to a Henry's constant, primary site density and saturation capacity. Do and Do (2000) proposed still another model that describes the formation of water clusters on activated carbon. This expression is implicit in water relative pressure with parameter values related to functional group concentration and micropore volume. Recently Lodewyckx and Vansant (1999) demonstrated the capability of the Dubinin-Astakov (DA) model to represent Type 5 water adsorption behavior by expanding on the work of Stoeckli (1994). This expression can be inverted to explicitly calculate partial pressure or loading. However it was noted that the DA can be inaccurate in describing the sigmoidal shape over a wide relative pressure range and can lead to some undefined values in the Henry's law limit. Salame and Bandosz (1999) reported water adsorption on activated carbons showing accurate correlation using the Viral equation. However, the Virial equation also possesses the characteristic of implicit determination of loading.

Earlier Mahle (1989) described water adsorption as the integrated pore distribution expressed as an incomplete Gamma function. Solution of the model in terms of the incomplete Gamma function becomes cumbersome and the model is implicit in

relative pressure. However this approach suggests that other formulations of the pore distribution function could be obtained. If a distribution that resulted in a simple integrated form was identified then it would possible to expand that distribution into an adsorption equilibrium expression by incorporating the correct temperature dependence. It can be noted that water adsorption on activated carbon is often represented on relative pressure and relative loading coordinates, because this serves to coalesce data over a wide range of temperatures. This does not completely account for the temperature dependence of the heat of adsorption. However it is an observation, which can be used in constructing a generalized expression.

2.2 Model Development

An adsorbed volume, V, can equally well be described as the integrated volume distribution function based on the adsorbent radius, r,

$$V = \int \frac{dV}{dr} dr \tag{2.1}$$

Knowledge of the functional form of the distribution could be obtained using an independent method or it could be determined from the adsorption equilibrium. For systems controlled by capillary condensation the Kelvin equation (2.2) applies

$$r = \frac{2V_m \gamma}{RT \ln\left(\frac{p}{p_s}\right)} \tag{2.2}$$

where V_m is the molar volume, γ the surface tension. A simple distribution function would have a quadratic form, which exhibits a single maximum and can be written as the algebraic expression (2.3)

$$y = \frac{2}{\left(x^2 + b^2\right)} = \frac{1}{b^2\left(\left(\frac{x}{b}\right)^2 + 1\right)} \tag{2.3}$$

This function is representative of a distribution of y as a function of the independent variable x, when the distribution is centered at the origin. The parameter b determines the breadth of the distribution. In order to consider a distribution in the range 0-1 corresponding to the relative pressure range, the variable x in equation (2.3) can be modified to change the center of the distribution,

$$x' = x - k \tag{2.4}$$

For values of x between 0 and 1, the parameter k in that same range would represent the value of x corresponding to the maximum of the distribution.

Integration of the distribution function is required in order to determine the cumulative capacity. The integral of equation (2.3) can be obtained from tables of integrals. The cumulative function in terms of x and k when integrated from 0 to x is

$$\int y dx = \frac{1}{b}\left(\tan^{-1}\left(\frac{x-k}{b}\right) - \tan^{-1}\left(\frac{-k}{b}\right)\right) \tag{2.5}$$

This integral can be normalized by satisfying the following constraint.

$$\int y dx = 1 \qquad when \qquad x = 1 \tag{2.6}$$

so that equation (2.5) becomes

$$\int ydx = \frac{\left(\tan^{-1}\left(\frac{x-k}{b}\right) - \tan^{-1}\left(\frac{-k}{b}\right)\right)}{\left(\tan^{-1}\left(\frac{1-k}{b}\right) - \tan^{-1}\left(\frac{-k}{b}\right)\right)} \tag{2.7}$$

A plot of equation (2.3) using (2.4) can be seen in Figure 2.1 as a function of parameter b, with k equal to 0.5. Increasing values of b leads to a broader distribution. Functions (2.3-2.5) satisfy the requirement to model the distribution function and equilibria for Type 5 isotherms.

If x is replaced with relative humidity, $p/p_s=p^*$, as suggested by the Kelvin equation and the cumulative distribution variable is replaced by relative adsorbed loading, n/n_s, an equilibrium expression can be obtained. Relative adsorbed volume could just as easily be used as relative adsorbed loading. However for water adsorption over a moderate temperature range the liquid density can be assumed to be constant. The expression of adsorption of Type 5 equilibrium then becomes

$$\frac{n}{n_s} = \frac{C}{B}\left(\tan^{-1}\left(\frac{p^*-A}{B}\right) - \tan^{-1}\left(\frac{-A}{B}\right)\right) \tag{2.8}$$

In order to force the cumulative isotherm loading to a specific value while varying the isotherm distribution shape parameter, B, and the isotherm centering parameter, A, a third parameter must be introduced. Here C is determined from the requirement that at saturation

$$\frac{n}{n_s} = 1 \qquad when \qquad p^* = 1 \tag{2.9}$$

so that

$$C = \frac{B}{\tan^{-1}\left(\frac{1-A}{B}\right) - \tan^{-1}\left(\frac{-A}{B}\right)} \tag{2.10}$$

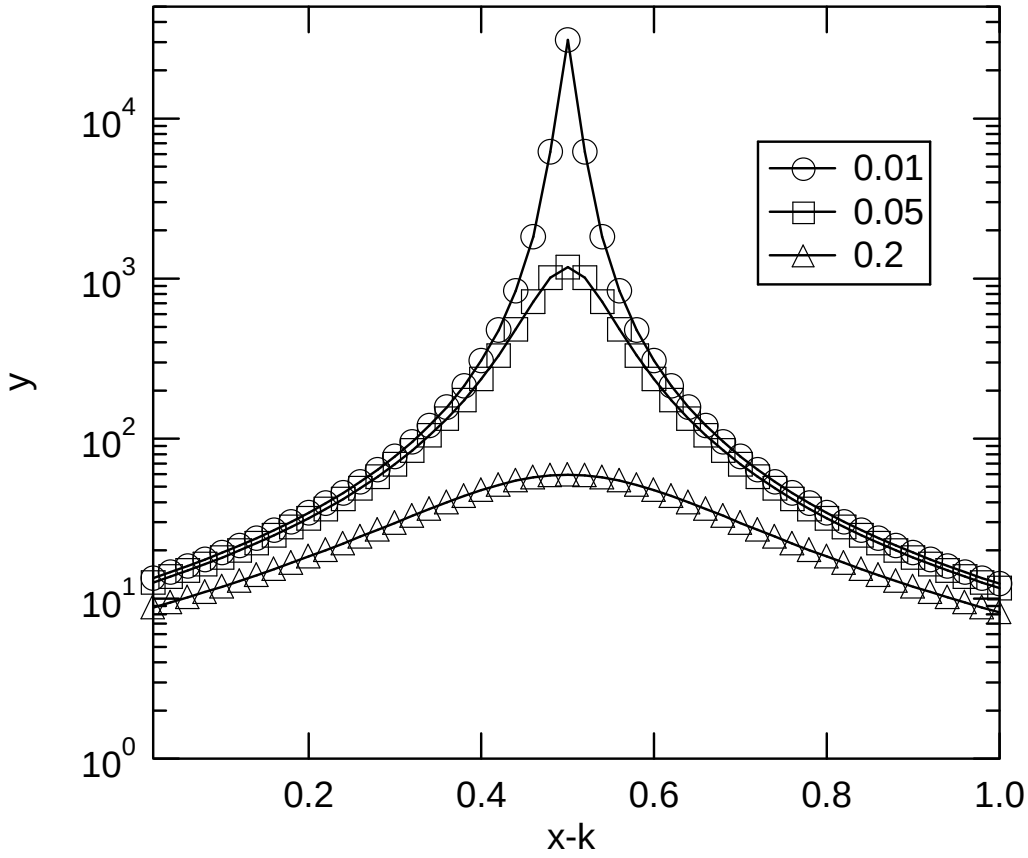

Figure 2.1 Distribution function, equation (3), plotted as a function of parameter b with parameter k=0.5.

and with the definition

$$D = \tan^{-1}\left(\frac{1-A}{B}\right) - \tan^{-1}\left(\frac{-A}{B}\right) \tag{2.11}$$

the final form of the equation then becomes

$$\frac{n}{n_s} = \frac{1}{D}\left(\tan^{-1}\left(\frac{p^*-A}{B}\right) - \tan^{-1}\left(\frac{-A}{B}\right)\right) \tag{2.12}$$

Note that the parameter A is bounded between zero and one so that (2.12) never becomes undefined. Equation (2.12) is the new adsorption equilibrium expression which contains three parameters, A the locus of the maximum of the distribution function in terms of relative humidity, B the breadth of the distribution and n_s the saturation capacity.

The important advantage of this expression compared to many other published models for Type 5 equilibria is that it can be written explicitly in terms of partial pressure or relative humidity as

$$p^* = B\tan\left(\frac{n}{n_s}D + \tan^{-1}\left(\frac{-A}{B}\right)\right) + A \tag{2.13}$$

A Henry's law limit can be evaluated for this expression

$$H = \frac{dp^*}{dn/n_s} = BD\left(\tan^2\left(\frac{n}{n_x}D + \tan^{-1}\left(\frac{-A}{B}\right)\right) + 1\right) \tag{2.14}$$

so that in the zero coverage limit, H, the Henry's law constant takes the form

$$H = BD\left(1 + \left(\frac{A}{B}\right)^2\right) \tag{2.15}$$

For the case where $(A/B)^2 >> 1$ this reduces to

$$H = \frac{A^2 D}{B} \tag{2.16}$$

where the parameters A and B are dimensionless.

Non-isothermal equilibrium behavior can be obtained through temperature dependent parameters of the model. One obvious choice would be to modify the A term which accounts for the centering of the distribution. The standard approach would be to redefine the parameter A through an exponential of inverse temperature

$$A = \exp\left(A_o + \frac{A_1}{T} \right) \tag{2.17}$$

The non-isothermal form of the model contains four parameters, A_o, A_1, B, n_s. The parameters can be referenced to the distribution function (2.3), so that the relative loading distribution can be calculated as

$$\frac{d\frac{n}{n_s}}{dp*} = \frac{1}{BD\left(\left(\frac{p*-A}{B}\right)^2 + 1\right)} \tag{2.18}$$

Note that the loading and relative humidity coordinates can be transformed into distribution coordinates by making use of the Kelvin equation (2.2) to yield the following relationship

$$\frac{dV}{dr} = -\left(\frac{d\frac{n}{n_s}}{dp*} \right) \frac{n_s V_m}{r} p* \ln(p*) \tag{2.19}$$

The new adsorption model must exhibit the correct temperature and loading dependence of the heat of adsorption in order to describe data over a wide range of temperatures. It is

instructive to consider the differential heat of adsorption as the contribution due to adsorption. This is defined by equation (2.20)

$$\Delta H_{diff} = RT^2 \frac{\partial \ln p}{\partial T} - \Delta H_{vap} \tag{2.20}$$

Solution of equation (2.20) by substitution of equation (2.13) can be achieved through the use of trigonometric identities and some algebraic manipulation to result in the following expression for the loading-dependent differential heat of adsorption.

$$\frac{\Delta H_{diff}}{R} = \frac{A_1 \frac{A}{B}}{1+\left(\frac{A}{B}\right)^2}\left[\tan\left(\frac{n}{n_s}D + \tan^{-1}\left(\frac{-A}{B}\right)\right) - \frac{A}{B}\right] \tag{2.21}$$

In the limit at zero coverage the differential heat of adsorption expression can be reduced to

$$\frac{\Delta H_{diff}}{R} = \frac{-2A_1\left(\frac{A}{B}\right)^2}{1+\left(\frac{A}{B}\right)^2} \tag{2.22}$$

for the case where $(A/B)^2 >> 1$ the differential heat of adsorption at zero coverage becomes

$$\frac{\Delta H_{diff}}{R} = -2A_1 \tag{2.23}$$

This result is consistent with the concept that the term A_1 in equation (2.13) is equivalent to the temperature correction term in an Antoine-type expression, which determines the heat of vaporization. Striolo et al. (2005) used experimental and simulation studies to examine the temperature effects of water adsorption on activated carbons.

2.3 Results

The new adsorption equation developed above can be used to describe experimental data. Water adsorption on activated carbon, the most common example of Type 5 equilibria will be considered. Due to the organic origin of many activated carbons high concentrations of polar sites exist. These could include organic and inorganic oxides. Water adsorption on BPL carbon would not be expected to exhibit behavior completely consistent with capillary condensation especially at low surface coverage and at low temperatures on such adsorbents. This effect is described by Talu and Meunier (2001) using the data of Rudisill (1992) for BPL carbon (Calgon Carbon Corp.).

Correlation of the water adsorption data on BPL carbon using the new adsorption model was performed. Considering only the data at 298 K on BPL carbon, a least squares regression was performed. When fitting data with multiple transitions, care must be taken to devise an appropriate weighting scheme. If the residual is computed using differences in loading then the center of the uptake slope will be heavily weighted. If the residual is computed using the differences in relative pressure then the ends of the isotherm will be more heavily weighted. A residual of the following form was chosen to fairly weight all the data points:

$$\mathrm{Re}\,sidual = \frac{\sqrt{\sum abs\left(\left(\left.\frac{n}{n_s}\right|_{\exp} - \left.\frac{n}{n_s}\right|_{\mathrm{mod}\,el}\right)\left(\left.p^*\right|_{\exp} - \left.p^*\right|_{\mathrm{mod}\,el}\right)\right)}}{N} \qquad (2.24)$$

The data together with the resulting correlation are presented in Figure 2.2. The fit parameters for the model are listed in Table 2.1 together with the computed residual. Figure 2.3 displays the data and model results for the case when BPL adsorption data at

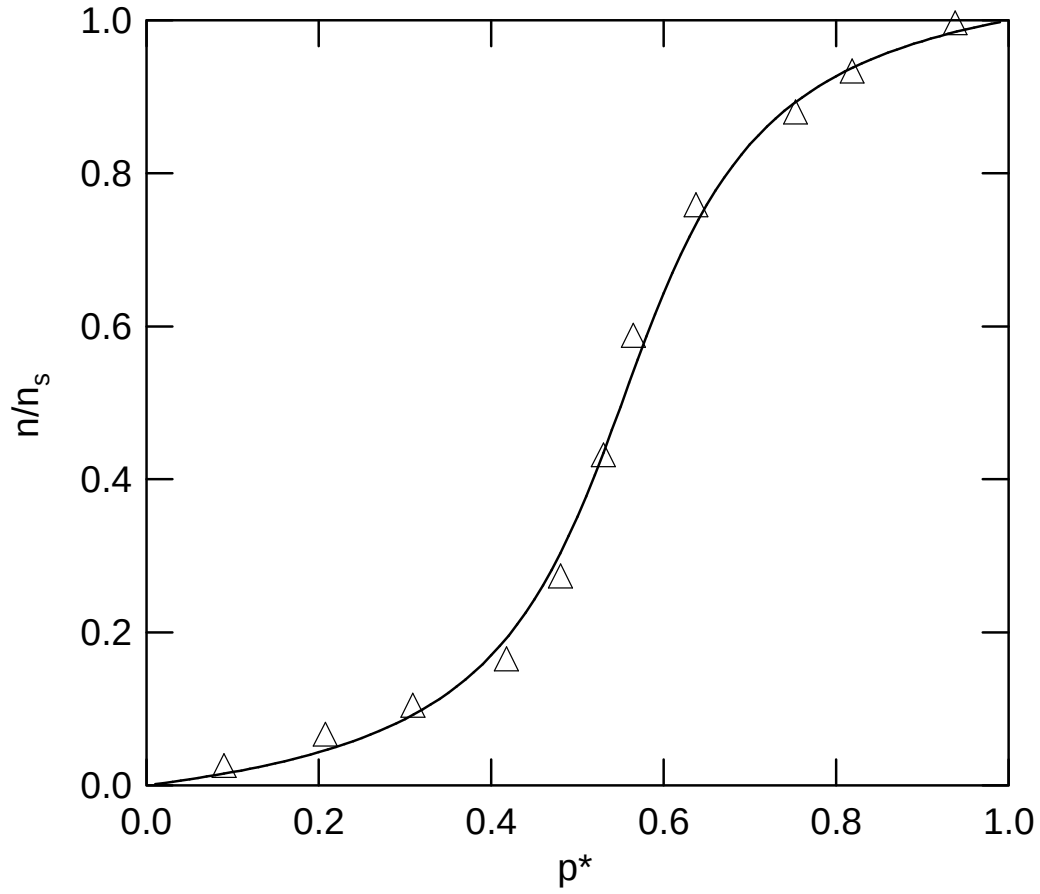

Figure 2.2 Water adsorption on BPL carbon at 25^{o}C represented by symbols. The line obtained by correlation of eqn (2.12) to the adsorption data.

Table 2.1 Regression parameters for three activated carbons using equations 2.12, 2.13, 2.17 and 2.24.

		Temp (K)	A_o	A_1 (K)	A	B	n_s (mol/kg)	Residual
BPL	ads	298			0.55	0.122	21.8	0.006
BPL	ads	298, 323, 348, and 373	0.55	-331		0.116	22.6	0.006
BPL	des	298			0.48	0.064	23.0	0.009
Charcoal (Gregg & Sing[14])	ads				0.71	0.056	31.3	0.011
Charcoal (Gregg & Sing [14])	des				0.58	0.026	31.1	0.008
Ambersorb 572	ads	298			0.62	0.077	18.5	0.010
Ambersorb 572	des	298			0.52	0.040	17.3	0.011

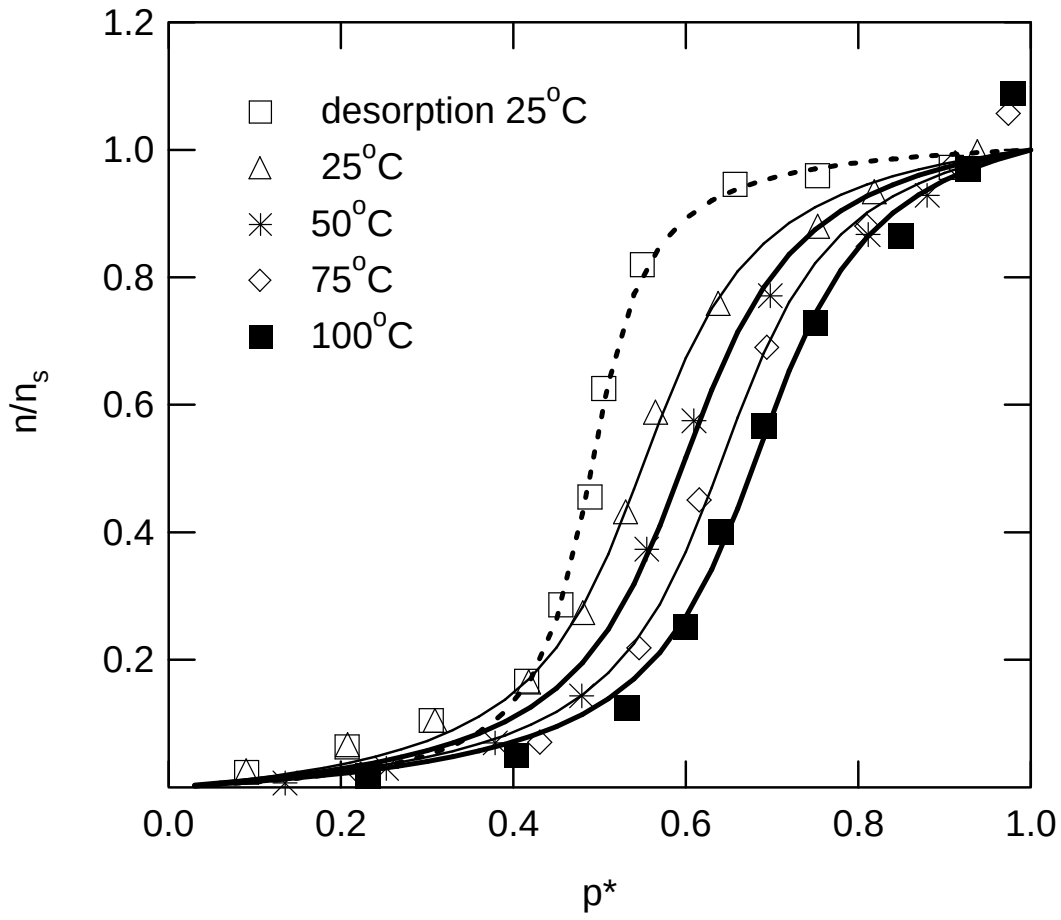

Figure 2.3 Water adsorption data on BPL carbon at four temperatures, 2 results for the case when BPL adsorption data at four temperatures 298 K and desorption at 298 K, represented symbols. The rightmost lines correspond to a single correlation to all adsorption data with equation (2.12). The leftmost lines correspond to a correlation of desorption data.

four temperatures 298, 323, 348, and 373 K are correlated together. In this case both an A_o and A_1 parameter are obtained as listed in Table 2.1. Also shown is the data and model result for correlation of the desorption data measured at 298 K. The desorption data with the resulting model fit are shown as the leftmost curves in Figure 2.3.

For the region where $p^* < 0.3$ at 298 K a significant loading is observed as compared to higher temperatures. Much lower loadings are observed in the same relative pressure range at 323 K and higher. The model gives an excellent fit to the data except at the lowest and highest relative pressures. At low relative pressure the model tends to underestimate the loading at 298 K, which would be expected in that the data for 323-373 K does not exhibit such pronounced adsorption in that relative pressure range. Near the saturation limit $p^*>0.95$ the data exhibits a secondary condensation corresponding to filling of the meso and macropores at 348 and 373 K, while the model predicts a lower saturation value. The single distribution function forming the basis of this new model cannot capture the effect of this secondary distribution in BPL carbon. A comparison of the fit obtained to 298 K data by correlating the 298 K and the combined 298, 323, 348, and 373 K is apparent from a plot of the residuals, Figure 2.4. The residual based on loading differences between model and experiment is shown. The residual is small at the lowest loadings and largest in the transition region. It should be noted that the single temperature correlation does not provide the lowest residual at every data point.

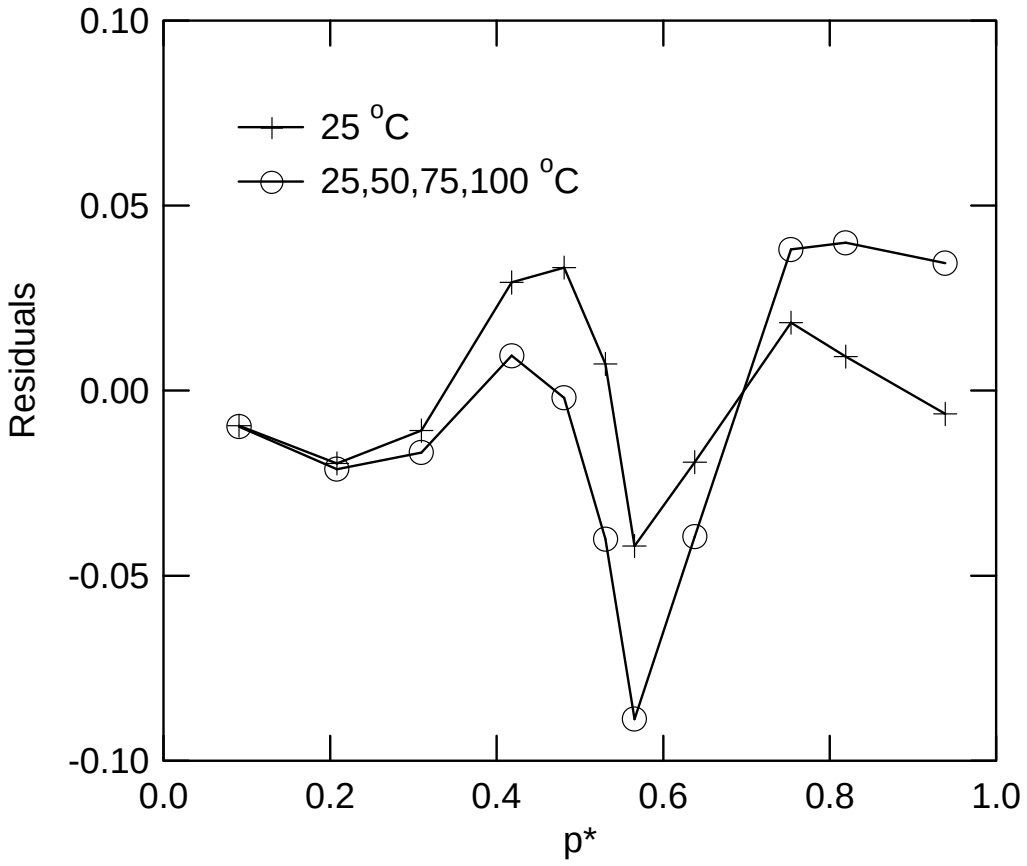

Figure 2.4 Residual based on loading difference for correlation of eqn (2.12) to BPL adsorption data at 298 K and at 298, 323, 348, and 373 K.

At the low concentration limit this model approaches the origin with a finite slope. The corresponding behavior of the Dubinin-Astakhov equation when correlated to the BPL data results in an abrupt convergence to a zero loading limit at approximately 0.3 relative humidity. That type of non-linear behavior is difficult to incorporate into numerical models for filter design. Nor does the DA equation fit describe the data as well.

Water adsorption data measured by Kiselev on another activated carbon was taken from Gregg and Sing (1982). Relative pressure and loading are plotted in Figure 2.5. No reference to the temperature of the experiment was provided. However the temperature is not required in order to employ the present model. Correlation with the new model to that data shows good agreement for both the adsorption and desorption branches. Another data set for water on a commercial synthetic adsorbent, Ambersorb 572 (Rohm and Haas Inc.), is plotted in Figure 2.6. Again good agreement is obtained with this adsorbent, which does not exhibit significant loadings at low relative pressures.

Several points can be noted about these results. It will be remembered that the parameter A, corresponds to the center of the distribution function, which for all the systems studied also corresponds to the relative humidity at 50% relative loading. If single temperature isotherms of BPL are correlated then a unique value of A would be obtained for each temperature. However when the data for BPL at all temperatures is correlated, the temperature dependence is captured by regressing for parameters A_o and A_1. Also the saturation capacity determined by this model for all three adsorbents is reasonable and agrees fairly well between adsorption and desorption branches. If the saturation capacity could be obtained independently then only 3 parameters would need

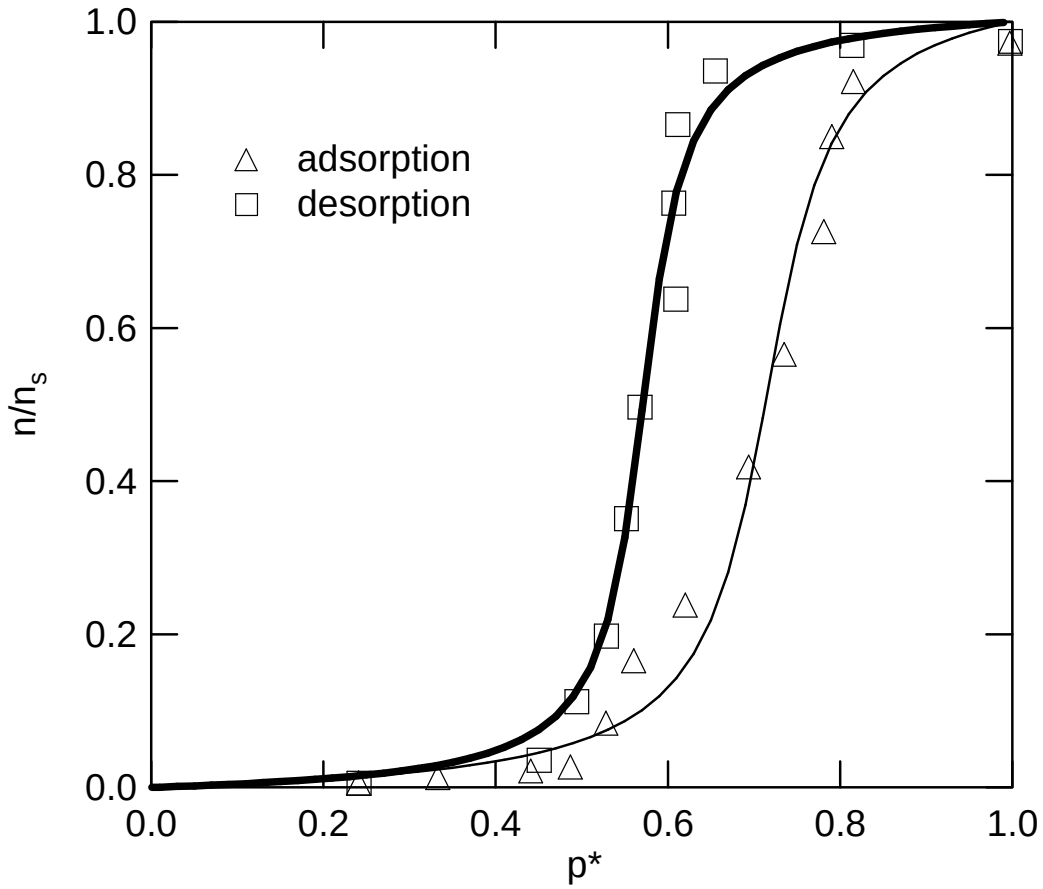

Figure 2.5 Water adsorption on charcoal by Kiselev, symbols are data, lines correlated by equation (2.12), leftmost curve corresponds to desorption.

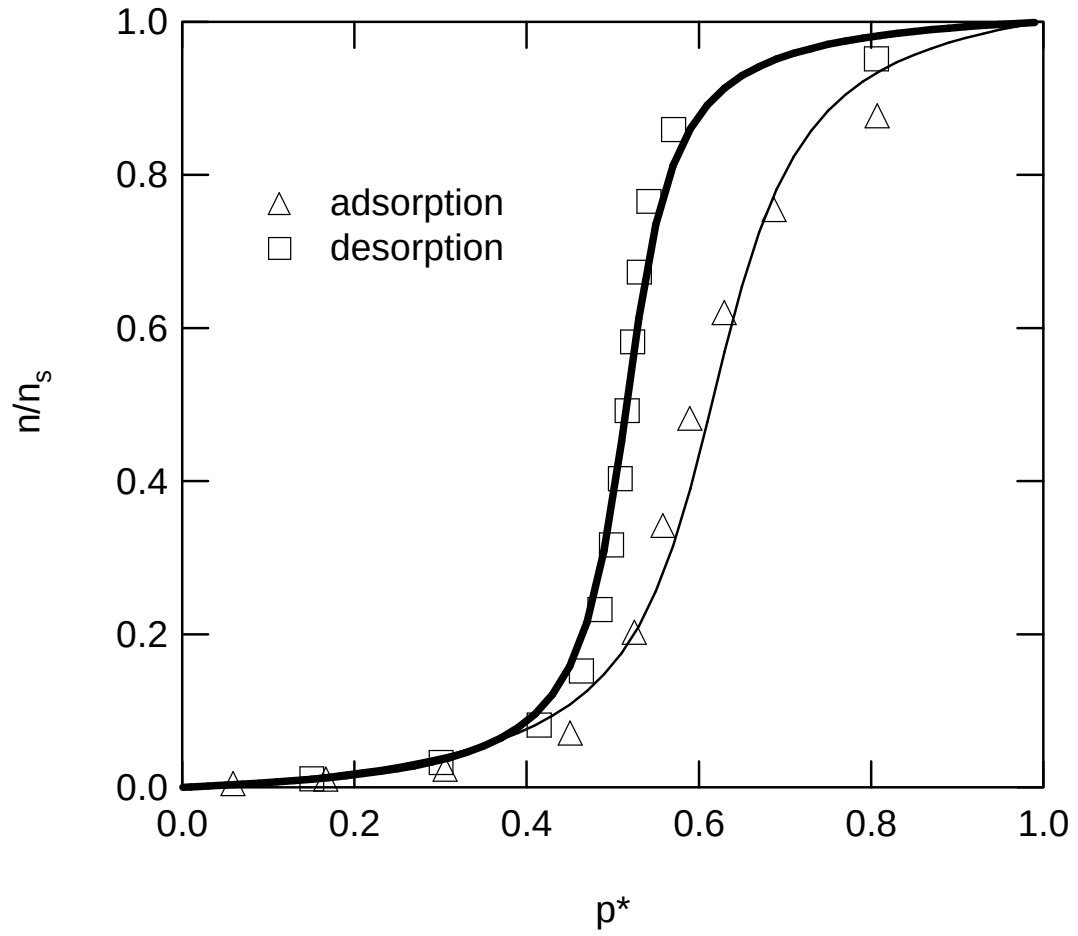

Figure 2.6 Water adsorption on Ambersorb 572 at 298 K, symbols are data, lines correlated by equation (2.12), leftmost curve corresponds to desorption.

to be regressed. The adsorption side of the hysteresis loop is characterized by a broader distribution function, larger B, for all three carbons than the desorption side. It is also possible to see that the term $(A/B)^2$ is much greater than 1.0, which allows the approximations, discussed above. Attempts to apply this expression to Type I equilibria was not successful, e.g. it would not describe methanol or nitrogen data on BPL carbon.

Salame and Bandosz (1999) reported low relative pressure water adsorption data on activated carbons. A higher loading and favorable low end isotherm shape was observed for a wood based carbon and lower capacity and unfavorable low end isotherm shape for a coal based carbon. This observation was attributed to larger micropore diameters and higher acid site content of the wood carbon. The present adsorption model cannot capture the favorable approach to zero loading but can represent unfavorable or linear low end behavior. This effect may not be significant in many practical applications in that the observed favorable region occurred below 0.5% relative humidity in their data. It was shown that the heat of adsorption could be easily calculated from the new model. This is performed using the correlation parameters for BPL carbon and plotted in Figure 2.7. Also shown are the corresponding results using the model of Talu and Meunier (2001). The differential heat of adsorption is presented because this gives a better representation of the influence of adsorption when the heat of vaporization is large. Although the average values are similar, the present model exhibits much weaker interaction at low coverage. This is a result of the absence of any loading dependence in the temperature dependent term A. For activated carbon adsorbents with a high number of oxide sites, there would be a favorable water adsorption behavior at low partial pressure in addition to the capillary condensation effects at high relative humidity. That is

the case that Talu and Meunier addressed. Any modification of the current model to include that behavior would likely not be mathematically invertible. The heat of adsorption versus loading distribution for this model is the same shape as the partial pressure versus loading distribution. Also shown in Figure 2.7 is the integrated differential heat of adsorption obtained by numerically integrating the differential heat of adsorption. This exhibits nearly linear behavior over the entire loading regime again as a result of the loading independent temperature term.

The starting assumption for the present model intended to describe a pore distribution, which would be filled by capillary condensation. It is a simple matter to examine the resulting distribution using equations (2.18-2.19) and the regression parameters. Figure 2.8 presents the distribution as determined by the model and by numerically differentiating the desorption data for BPL at 298 K. As expected very good agreement is obtained. Perhaps even better agreement would be possible with more data and reduced derivative increment for the data. While the assumptions inherent in applying the Kelvin equation to micropores have been challenged, this model does provide a tool for easy calculation of capillary condensation of vapors other than water on larger pore adsorbents.

A parameter sensitivity analysis was performed for the new type 5 isotherm model. Two base conditions were considered a single isotherm to assess sensitivity of A and B and multiple temperature isotherms to assess A_0, A_1, and B. The base case parameters corresponded to BPL carbon at 298K and BPL carbon at 298, 323, 348 and 373 K. A difference value, η, was computed using the base case loadings and the loadings obtained with an incrementally changed parameter

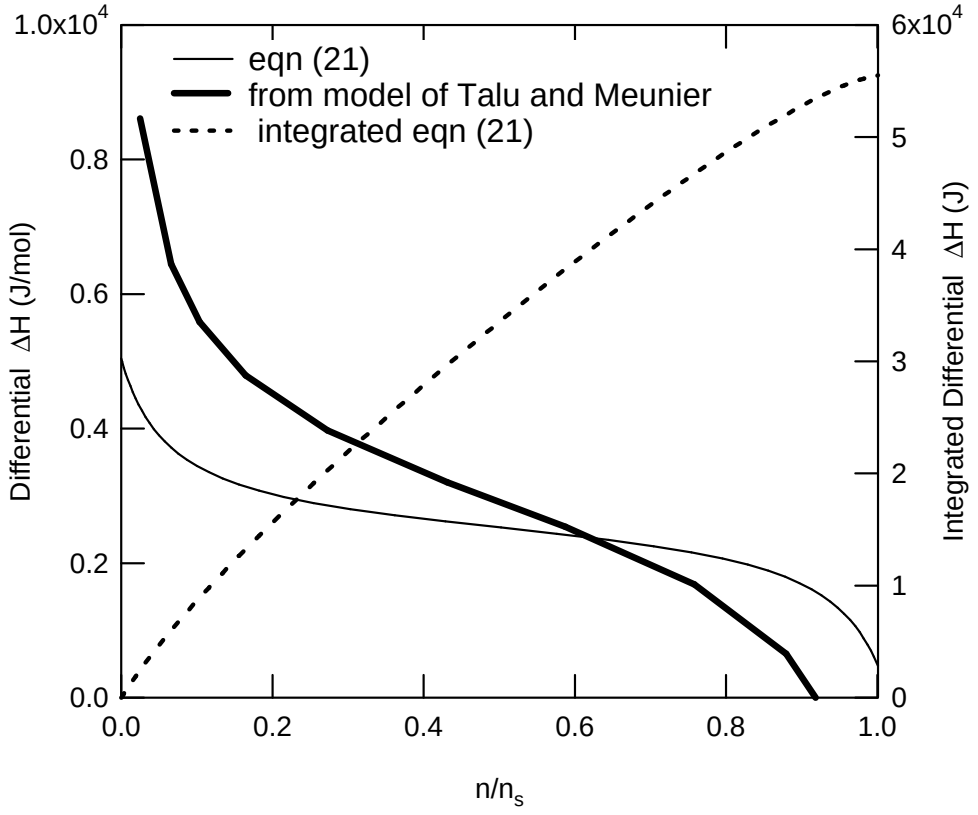

Figure 2.7 Differential heat of adsorption as calculated from the equation (2.21), and the model of Talu and Muenier. Also shown is the integrated differential heat of adsorption from equation (2.21).

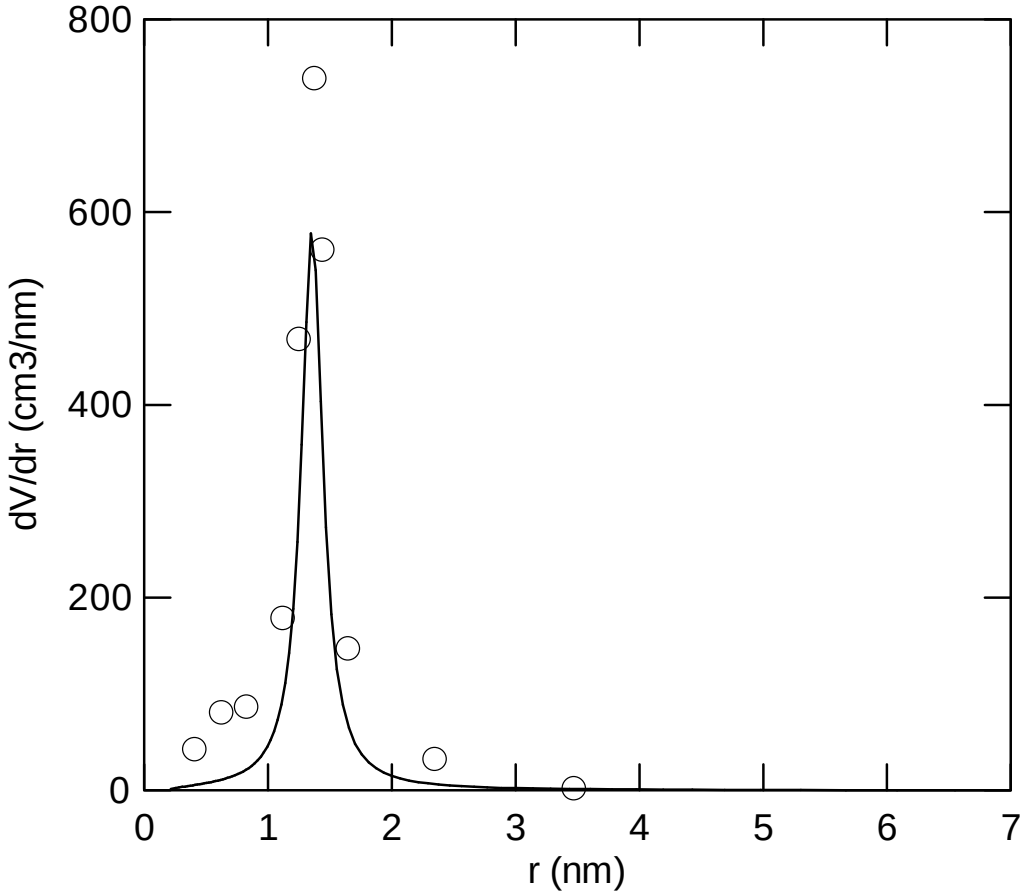

Figure 2.8 Pore size distribution function obtained from water desorption on BPL carbon at 298 K, line obtained using equations (2.18-2.19), symbols are from differentiating measured data.

$$\eta = \frac{\sum abs(n_{new} - n_{base})}{N} \tag{2.25}$$

where the parameter sensitivity, δ_i, is defined as

$$\delta_i = \frac{\partial \eta}{\partial P_i} P_i \tag{2.26}$$

The sensitivity parameters are listed in Table 2.2. Nearly an order of magnitude greater sensitivity is associated with the A than the B parameter because the sharp transition must be captured by correct centering of the distribution. The A_1 and A_0 parameters have similar sensitivity indicating that the temperature effect and centering have similar influence in location the sharp transition.

2.4 Conclusions

An equation has been developed which is capable to representing the sigmoidal behavior of Type 5 adsorption isotherms. This equation possesses the useful property that either partial pressure or loading can be determined explicitly. The parameters in this expression are shown to be related to a pore distribution function for adsorption systems, which are described by the Kelvin equation. The heat of adsorption expression has been derived for this model. Correlation of the model to water adsorption data on activated carbon is shown to exhibit quantitative agreement over the range of 10-90% relative humidity.

Table 2.2 Type 5 isotherm parameter sensitivity.

	Base Case Parameter	η	δ
298 K parameters			
A	0.55	0.091	0.46
B	0.122	0.013	0.063
298, 323, 348, 373 K parameters			
A0	0.55	0.060	0.30
A1	-331	0.096	0.48
B	0.116	0.013	0.064

Chapter 3: Coadsorption Equilibria for Immiscible Vapors

3.1 Introduction

Trace organic vapor contaminant removal from air streams is effectively accomplished using activated carbon based adsorption processes. Water vapor present as an adsorbable component in air exhibits Type 5 behavior while adsorbable organic vapor contaminants exhibit Type 1 behavior. Knowledge of adsorption equilibria aids in the selection of appropriate adsorbents and conditions for adsorption separations. Methods to estimate adsorption equilibria for water coadsorption on activated carbon, which are not purely correlative, would be valuable in fixed bed adsorption models, because a wide range of concentration and temperatures must often be described. Various approaches to correlate and predict this type of adsorption equilibria behavior have been proposed. Of interest in adsorber design is an approach, which offers rapid solution while minimizing the need for measured adsorption data by incorporating some thermodynamic basis. A design limiting condition for practical adsorption systems is the case of moderate to high volatility water insoluble vapors coadsorbing in the presence of humidity. Methods to describe these systems will be discussed.

3.2 Water Coadsorption Literature Review

Activated carbon exhibits a non-specific affinity for organic vapors and gases, which is manifested by adsorption equilibria being well correlated to vapor pressure. Higher volatility species are in general more weakly adsorbed due to physical adsorption than

low volatility species. Coadsorption of water vapor on activated carbons tends to diminish the adsorption of organic vapors in the case of insoluble components. A number of experimental studies of coadsorption of water and organic vapors have been presented. Rudisill and LeVan(1992) described hexane/water and acetone/water coadsorption on BPL activated carbon. They observed that hexane loading was not independent of the water loading, but rather that the hexane and water compete for adsorption sites. No model was offered to describe those results. In a continuation of that work Eissmann and LeVan (1993) reported adsorption data for CFC-113/water and dichloromethane and water on BPL carbon. They observed that the solubility of the compound in water affects the extent of pore filling. Greater solubility leads to increased pore filling as a more water-soluble species can provide a site for formation of water clusters and further water adsorption. Again no model was offered to describe the observed results. More recently Russell and LeVan (1997) reported coadsorption of ethane/water and propane/water on BPL activated carbon. Again water adsorption was shown to diminish the adsorption of the organic compared to the pure component behavior. In order to describe their data and the earlier coadsorption results. They proposed a power-law mixing model

$$n_c = n_c^* \left(1 - \frac{n_w}{n_{w_{sat}}} \right)^i \tag{3.1}$$

$$n_w = n_w^* \left(1 - \frac{n_c}{n_{c_{sat}}} \right)^k \tag{3.2}$$

which provided quantitative agreement with several sets of multicomponent adsorption data. However the approach was purely correlative, implicit in loading and iterative.

Taqvi et al. (1999) proposed a method to describe multicomponent adsorption equilibria derived from viral equations. They examined the hexane and water data cited above. The model resulted in expressions implicit in loading. The curvature of the water equilibria required fitting with up to fourth order parameters. They noted that the polynomial form of the model could lead to numerical solution difficulties when implemented in fixed bed models. They also reported coadsorption measurements for several simple alcohols on BPL carbon. They applied the multicomponent virial equation model and found good agreement.

Observations of the water carbon interaction in the presence of coadsorbed benzene and chloroform was examined by NMR by Turov et al. (2002). They showed that the immiscible organic resulted in the inability of water to occupy the higher energy micropores. A similar conclusion was reached by Zimny et al. (2005) who by experiments showed that for the coadsorption pair naphthalene and water on activated carbon organic allows only large water clusters to form in mesopores. They employed the Type 5 isotherm model presented in Chapter 2. A molecular simulation of ethane and water coadsorption was performed by Jorge and Seaton (2003) which showed good agreement with experiment but was dependent on correlating the pure water equilibria to a polar size distribution.

The water adsorption behavior on activated carbon is characterized by the presence of hysteresis. This phenomenon implies that the path used to approach equilibrium affects the thermodynamics of water adsorption. Greater capacity is observed when approaching water equilibrium from saturation. This suggests that in the case of organic and water coadsorption the equilibria for each component could be affected not

only by the path that water equilibrium is approached but also by the order of water and chemical exposure. In the data of Rudisill water desorption profiles were measured at fixed hexane and acetone loadings. The methods employed to determine the data all rely on either loading the organic first or simultaneously with water, where simultaneous adsorption probably has the same effect as loading the organic first because water adsorption is initially unfavorable and thus slower than the favorable adsorption of organic. The propane and ethane data was measured under simultaneous exposure but always from the case of an initially clean adsorbent. There is no reported data for the effect of the order of adsorption.

Other models to describe multicomponent adsorption equilibria for the non-ideal mixtures associated with organics and water have been proposed. The good agreement reported with the potential theory models for pure component equilibria has led to several proposed extensions to multicomponent equilibria. The thermodynamic assumption of ideal gas behavior suggests that some empirical correlation based on the adsorption potential

$$\varepsilon = RT \ln\left(\frac{p}{p_o}\right) \tag{3.3}$$

can be formulated. Observations by Dubinin verified that the following relationship

$$\varepsilon = \beta E(-\ln(\theta))^{1/2} \tag{3.4}$$

applied for activated carbon systems over a wide range of concentrations and temperatures. The heat of adsorption can be calculated for this expression as

$$\Delta H_{ads} = -\left.\frac{Rd\ln(p)}{d1/T}\right|_n = RT^2 \left.\frac{d\ln(p)}{dT}\right|_n \cong RT^2 \left.\frac{d\ln(p)}{dT}\right|_\theta \tag{3.5}$$

If the saturation vapor pressure can be represented by an Antoine expression of the form $\ln(p_o)$=A-B/T then

$$\Delta H_{ads} = \beta E(-\ln(\theta))^{1/2} + BR \tag{3.6}$$

and the differential heat of adsorption can be written as

$$\Delta H_{ads} = \beta E(-\ln(\theta)^{1/2} \tag{3.7}$$

For the case of immiscible organic and water adsorbed components Manes (1983) suggested that since organic vapor adsorption on activated carbon is correlated well by potential theory models that the adsorption potential of the organic would be diminished by competition with water vapor for available pore volume. He proposed a method in which the adsorption potential of the coadsorbed organic was calculated by subtracting the difference between the pure and mixture adsorption potential of water from the adsorption potential of the pure organic.

This extension to the potential theory model assumes that water contributes to a reduction in the adsorption potential of the organic and that the organic adsorbate preferentially adsorbs versus water, reducing the water capacity, such that no water adsorption is predicted if the organic loading is below the pure component water loading. Implicit in this approach is the assumption that the organic and water vapor adsorb to the same saturation volume, which is not a valid assumption for many adsorbents. This approach also required that the influence of water adsorption be ignored if the volume of organic loading exceeded the volume of water loading as pure components. The modified potential equation is written as

$$\frac{RT}{V_A}\ln\frac{p_{o,A}}{p_{mix,A}} = \frac{\varepsilon_A}{V_A} - \frac{RT}{V_w}\ln\frac{p_{o,w}}{p_{mix,w}} - \frac{\varepsilon_w}{V_w} \tag{3.8}$$

where ε is evaluated from the pure component potential plot of either the organic or water at the organic volume. Solution of this expression can be obtained given the water and organic mixture partial pressure by assuming an organic mixture volume for both ε_A and ε_w at that organic volume and iterating until eq. 3.8 is satisfied. This approach assumed that the water isotherm could be described on a potential plot, which is incorrect because the potential plot does not capture the sigmoidal shape of the water isotherm. The Manes model is essentially a correction to the heat of adsorption of the organic due to the adsorption of water because it has already been shown that the isosteric heat of adsorption for the potential model is the potential itself as seen in eq. 3.4 and 3.7.

Yang and Doong (1985) proposed a model based on a modified potential theory solution, which was written implicit in loading. Their model can be described as a volume reduction method. If potential relationships are written for both the organic and water where

$$V_i = V_{sat} * \exp\left(-\left(\frac{T}{\beta_i E}\right)\left(\ln\frac{P_{si}}{P_i}\right)^2\right) = V_{sat} * \Psi_i \tag{3.9}$$

The factor Ψ is the fractional loading term. In the Doong model the mixing rule for organic and water coadsorption is written as

$$\begin{aligned} V_{1,mix} &= \left(V_{sat} - V_{2,mix}\right) * \Psi_1 \\ V_{2,mix} &= \left(V_{sat} - V_{1,mix}\right) * \Psi_2 \end{aligned} \tag{3.10}$$

This can be solved to express the volume adsorbed in terms of the fractional loading

$$V_{1,mix} = V_{sat} * \Psi_1 * \left(\frac{1-\Psi_2}{1-\Psi_1 * \Psi_2}\right) \tag{3.11}$$

If component 2 is water then as the RH approaches zero Ψ_2 approach 0 and as RH approaches 1 then Ψ_2 approach 1 and $V_{1,mix}$ approaches zero. Russell and LeVan (1997) compared the power law model eq. 3.1-3.2, with the models of Manes and Yang. The latter two were shown to provide similar residuals with the greatest error in predicting the amount of coadsorbed water.

Methods to predict adsorption equilibria for multicomponent mixtures are well developed for the case of mixtures that form an ideal adsorbed phase on adsorbents with limited heterogeneous character. The IAST has been shown to be a thermodynamically consistent approach for such systems. Methods to describe coadsorbed water and an immiscible organic equilibria however are limited to the few described above. While the predictive methods for ideal adsorbed phase systems may not be applicable for immiscible systems the approach used to develop the theories can be considered as a basis from which to derive a practical if less rigorous theory for water organic coadsorption. A method is sought which can be readily implemented in fixed bed adsorber models. This implies that the model must be well behaved, and have a non-iterative solution.

Phase equilibrium theory is based on the concept that thermodynamic properties such as temperature, pressure and chemical potential are equated across the phases. Following the development of Young and Crowell (1962) the Fundamental Equation in terms of the internal energy of a system consisting of adsorbent in amount n_A and adsorbed gas, n_s, can be written as

$$dU = TdS - PdV + \mu_A dn_A + \sum \mu_{s,i} dn_{s,i} \qquad (3.12)$$

If a new function is written which represents the difference between the adsorbed system and the adsorbent alone, where difference variables are employed, corresponding to the property of the adsorbate, the resulting expression is

$$dU_s = TdS_s - PdV_s + (\mu_A - \mu_{0A})dn_A + \sum \mu_{s,i} dn_{s,i} \tag{3.13}$$

For the case of an inert adsorbent the surface area, A, is proportional to n_A, and new variable, π, can be defined as $-(dU_s/dA)_{Ss,Vs,ns}$. This new variable represents a chemical potential of the adsorbent in the presence of adsorbate in terms of surface area or

$$dU_s = TdS_s - PdV_s - \pi dn_A + \sum \mu_{s,i} dn_{s,i} \tag{3.14}$$

When the Gibbs free energy, G_s, is defined as $U_s+PV_s-TS_s$, then the following expression results

$$dG_s = -S_s dT + V_s dP - \pi dA + \sum \mu_{s,i} dn_{s,i} \tag{3.15}$$

If a new free energy term is defined $F_s = \Sigma \mu_{si} n_{si}$ then the following expression can be written

$$dF_s = \sum n_{s,i} d\mu_{s,i} + \sum \mu_{s,i} dn_{s,i} \tag{3.16}$$

Also by integrating eq. 3.11 above

$$F_s = G_s + \pi A \tag{3.17}$$

which leads to

$$dF_s = dG_s + \pi dA + Ad\pi \tag{3.18}$$

Combining eq. 3.12-13, and 3.15 an expression for $d\mu_s$

$$\sum n_{s,i} d\mu_{s,i} = -S_s dT + V_s dP + Ad\pi \tag{3.19}$$

At constant temperature and pressure this gives the Gibbs isotherm. If pure component behavior is considered then equilibrium between the gas and adsorbed phases can be written as $d\mu_s = d\mu_G$ which lead to the expression

$$-S_s dT + V_s dP + \left(\frac{1}{\Gamma}\right) d\pi = -S_G dT + V_G dP \tag{3.20}$$

where $\mathbf{S}_s = S_s/n_s$, $\mathbf{V}_s = V_s/n_s$ and $\Gamma = n_s/A$.

The Gibb's equation for spreading pressure defined at constant temperature then becomes

$$d\pi = \Gamma\left(V_G - V_s\right) dP_T \tag{3.21}$$

The form of this equation suggests that π is similar to a pressure term except that it is defined relative to the adsorbent surface area rather than volume. In the case of an ideal gas assumption and with $V_G >> V_s$

$$\pi = RT \int_0^{po} \Gamma d\left(\ln p\right) \tag{3.22}$$

where n is related to p through the pure component equilibria. Various choices for the functional form of Γ, the pure component adsorption isotherm, can be applied in eq. 3.19 to determine a two-dimensional equation of state, i.e. the relationship between spreading pressure and coverage.

For the case of multicomponent adsorption of an ideal mixture the following expression can be written for the mixture spreading pressure

$$A\pi = \sum RT \int_0^{p_i o} n_i d\left(\ln p_i\right) \tag{3.23}$$

The spreading pressure evaluated for pure component adsorption can be viewed in as a weighting function. To a first approximation Γ/p is the isotherm slope. When integrated over the partial pressure range, a more favorable equilibria would result in a larger

adsorbed phase pressure at equivalent spreading pressures. However this integration is not always possible especially if extrapolation is required beyond the saturation limit. If a non-ideal adsorbed phase or multiple adsorbed phases are formed then weighting methods other than the spreading pressure can be considered. One indication of separate phase behavior would be the case where adsorbed components exhibit different adsorbed phase saturation volumes. This is observed with water and organic adsorption on activated carbon.

The development of the IAS in terms of spreading pressure could have been approached in terms of surface potential, ϕ', and adsorbent volume, V_A so that the fundamental equation is written as

$$dU_s = TdS_s - PdV_s - \phi' dV_A + \sum \mu_{s,i} dn_{s,i} \tag{3.24}$$

The Gibbs adsorption isotherm then becomes

$$V_A d\phi' = \sum n_{s,i} d\mu_{s,i} \tag{3.25}$$

The chemical potential is related to the free energy change. By equating the chemical potential in the gas and adsorbed phase an expression for the surface potential can be obtained.

$$\phi' = \frac{1}{V_A} \int \sum n_i d \frac{\partial G}{\partial n_i} \tag{3.26}$$

All adsorption and mixing thermodynamics are captured in this expression. For the case of no mixing or ideal mixing the energy difference between adsorbed phase and vapor phase free energy can be approximated by a measurable quantity, a calorimetric heat, such as the differential or isosteric heat.

A two-dimensional equation of state can be constructed for multicomponent adsorption equilibria (Appel et al. 1998). This approach can be summarized as

$$\frac{\pi A}{RT} = \left.\frac{\pi A}{RT}\right|_{pure\,1} + \left.\frac{\pi A}{RT}\right|_{pure\,2} + \left.\frac{\pi A}{RT}\right|_{mixture} \tag{3.27}$$

which can be expressed in a thermodynamically consistent form. Solution of this expression can be obtained in terms of the partial pressure of each component of the mixture. Using a virial equation the mixing terms can be expressed as a series expansion of interaction terms. Correlation of mixture data is possible, which as with the virial expansion method discussed earlier can result in fourth order or higher terms, in order to capture non-linear behavior.

3.3 The Enthalpy Ratio Model for Coadsorbed Immiscible Mixtures

The thermodynamics of physical adsorption can be used to demonstrate that there exist is a relationship between energy terms such as Gibb's Free energy and enthalpy and phase equilibria. Derivation of a phase equilibrium expression is dependent on selection of a set of mixing rules which are not provided by the thermodynamics. The simplest method to compute multicomponent equilibria loadings given the mixture partial pressures would be to compute a correction factor, to be multiplied by the predicted pure component loading.

$$n_{mix} = n_{pure} * f(\Delta H_{ads,i}) \tag{3.28}$$

This approach is similar to that of most isotherm expressions where the computed loading is expressed as the saturation capacity multiplied by some function of the heat of adsorption

$$n_{pure} = n_{sat} * f(\Delta H_{ads}) \tag{3.29}$$

which may be an implicit relationship. The competition in coadsorption for adsorption sites would have to consider the affinity of each species at all sites. This can be accomplished with an integrated free energy expression or in this case integrated enthalpy

$$\Delta H^* = \int_0^{no} \Delta H(n)dn \tag{3.30}$$

where the integration limit is the loading corresponding to the mixture partial pressure. If the relative loading of each component is determined by an inverse relationship so that each component to exhibits an equal surface potential then the loading of the component with the larger heat of adsorption would yield the greater loading as expected.

The appropriate form of the enthalpy expression must describe the relative affinity of each component. The isosteric heat of adsorption is the loading dependent enthalpy calculated according to eq. 3.5, which includes all energy exchanged both from the phase change and surface interaction. The differential heat of adsorption represents the isosteric heat of adsorption minus the enthalpy of condensation, providing a better indication of the relative affinity of various components. This can be readily calculated for organic vapors which conform to the DR relationship. The heat of adsorption of water was discussed in chapter 2. The model suggested a nearly constant heat of adsorption over the entire range of loadings. However, the presence of hysteresis suggests that the heat of adsorption is actually greater at higher loadings than at lower loadings.

Hysteresis results from the formation of larger hydrogen bonded water clusters at progressively larger pore filling. The first patches of adsorbed water are further stabilized as the patches merge with other patches when larger pores are filled. This suggests that the heat of adsorption of would be a function of the fractional filling. The dual contributions to water adsorption from surface adsorption and hydrogen bonding suggests

also that the heat of adsorption of water can be represented by two terms. The first is a surface interaction energy which would represent water molecules that compete with favorably adsorbed species for surface sites. The second contribution to the water adsorption energy is from hydrogen bonding as a result of interaction of non-surface bound water molecules. Thus the energy term for water adsorption which must be considered in an organic water mixture can be expressed as

$$H_{w,surface} = H_{ads} - H_{hydrogen\quad bonding} \tag{3.31}$$

where H_{ads} is taken from the differential heat of adsorption.

The simplest method to compute mixing behavior using the integrated enthalpy approach is to write a correction factor to the pure component behavior based on a ratio rule. However this approach can be advanced beyond the loading ratio rule mentioned earlier by employing thermodynamic characteristics of the process. Two limits of behavior must be addressed miscible and immiscible adsorbed phases. When considering immiscible systems the lack of a single adsorbed phase suggests that the use of adsorbed phase mole fractions would be un-informative. For immiscible adsorbates competition for adsorption sites occur, or the adsorbate with the greater heat of adsorption then it would adsorb preferentially reducing the affinity of surface sites for the other adsorbates. Using the assumption that the organic vapor in an organic-water mixture adsorbed on activated carbon has the greater affinity then the mixing rule for organic adsorption can be written as a ratio of the component enthalpy versus the total enthalpy for both components

$$\phi_i = \frac{H^{\text{int}}_{i,mix}}{H^{\text{int}}_{i,pure}} \approx \frac{H^{\text{int}}_{i,pure}}{H^{\text{int}}_{i,pure} + H^{\text{int}}_{w,pure}} \tag{3.32}$$

where the numerator represents the enthalpy of the species considered and the denominator is the sum of the enthalpy of both adsorbed organic and water. Now the integrated heat of adsorption based on the Dubinin-Radushkevish equation and the water isotherm is approximately linear so that

$$H^{\text{int}}_{differential,i} = \int_0^{\theta} H_{differential,i}\, d\theta = K * n \tag{3.33}$$

so

$$\frac{n_{i,mix}}{n_{i,pure}} \approx \frac{H^{\text{int}}_{i,mix}}{H^{\text{int}}_{i,pure}} \tag{3.34}$$

The individual component loading would be expressed in the following form

$$n_{i,mix} = \phi_i n_{i,pure} \tag{3.35}$$

For miscible adsorbed phases a mixing rule based on adsorption enthalpy could be proposed where the resulting mixture enthalpy would correspond to the greatest for all components and the mixture ratio is governed by the fractional contribution of enthalpy of each component or the enthalpy fraction, x_i,

$$x_i = \frac{H^{\text{int}}_i}{\sum H^{\text{int}}_i} \tag{3.36}$$

It is unlikely that immiscible mixtures would conform to this simple linear relationship of eq. 3.32 between fractional organic loading and water coadsorption enthalpy contribution over all concentration and loading ranges. The regime of conditions for which eq. 3.34 is applicable must be investigated. The appropriate choice for the enthalpy of the organic would be the isosteric heat of adsorption, which is the sum of the differential heat of adsorption and the heat of vaporization.

Water adsorption is seen to result from capillary condensation. It is assumed that the adsorbed phase for water is not able to form the extensive network of hydrogen bonding that stabilizes liquid water. Therefore the heat of vaporization effect is minimized in water adsorption. Rather it is observed that hysteresis occurs in water adsorption suggesting that hydrogen bonding and adsorbed phase stability increases with increasing water loading. The heat of adsorption of water is lower at low loadings than at high loadings. Hysteresis leads to cooperative bonding such that at higher loadings the oligomers are better stabilized. Therefore any factors which limit the ability of the hydrogen bonded network to form would inhibit water adsorption. The water adsorption relationship in the case of organic-water coadsorption can be expressed as the pure component water loading multiplied by a correction factor which accounts for the adsorbed volume of the organic and the extent which the adsorbed organic has penetrated the pores required for hydrogen bonding or

$$n_{water}^{mix} = F_{hysteresis} n_{water}^{pure} \tag{3.37}$$

The correction factor $F_{hysteresis}$ can be calculated from the water isotherm. The fractional filling on desorption is a function of the fractional filling on adsorption

$$\theta_{desorption} = f(\theta_{adsorption}) \tag{3.38}$$

Given that the desorption loading of the water isotherm exhibiting hysteresis lies above the adsorption loading at the same partial pressure then there is a one to one relationship that maps the adsorption loading to the desorption loading for that isotherm. The hysteresis correction factor is computed as

$$F_{hysteresis} = 1 - \theta_{desorption} = 1 - f(\theta_{adsorption}) \tag{3.39}$$

This correction factor would be unity at low loadings and approach zero at loadings corresponding to the steepest part of the desorption isotherm. This hysteresis correction relationship can be calculated directly using the water adsorption correlation developed earlier for the adsorption and desorption branches. This relationship has been correlated for both BPL carbon as shown in Figure 3-1. The correlation parameters are listed in Table 3.1. There was no measurable hysteresis observed for water adsorption on Ambersorb 563.

If an organic vapor coadsorbed with water then it is proposed that the water loading is reduced by an amount corresponding to pure component water loading multiplied by the hysteresis factor, where the hysteresis factor is computed from the organic adsorption loading

$$n_{w\ mix} = n_{w,\,pure} F_{hysteresis} \tag{3.40}$$

The integrated differential heat of adsorption used to compute the coadsorbed organic loading in eq. 3.32 can be corrected using the hysteresis factor and the fractional organic loading. At low fractional organic loadings the effect of adsorbed water should to be minimal so that the organic loading approaches the pure component loading. The corrected water adsorption enthalpy becomes

$$H_{w,corrected} = H^{\text{int}}_{w,\,pure} F_{hysteresis} \theta_{i,\,pure} \tag{3.41}$$

which is used in the denominator of eq. 3.32.

The current model eq. 3.28-3.36 for organic and eq. 3.37-3.39 for water represent a semi-empirical approach to co-adsorption equilibria, however the solution does not require any fit parameters. The integrated heat of adsorption can be calculated for both

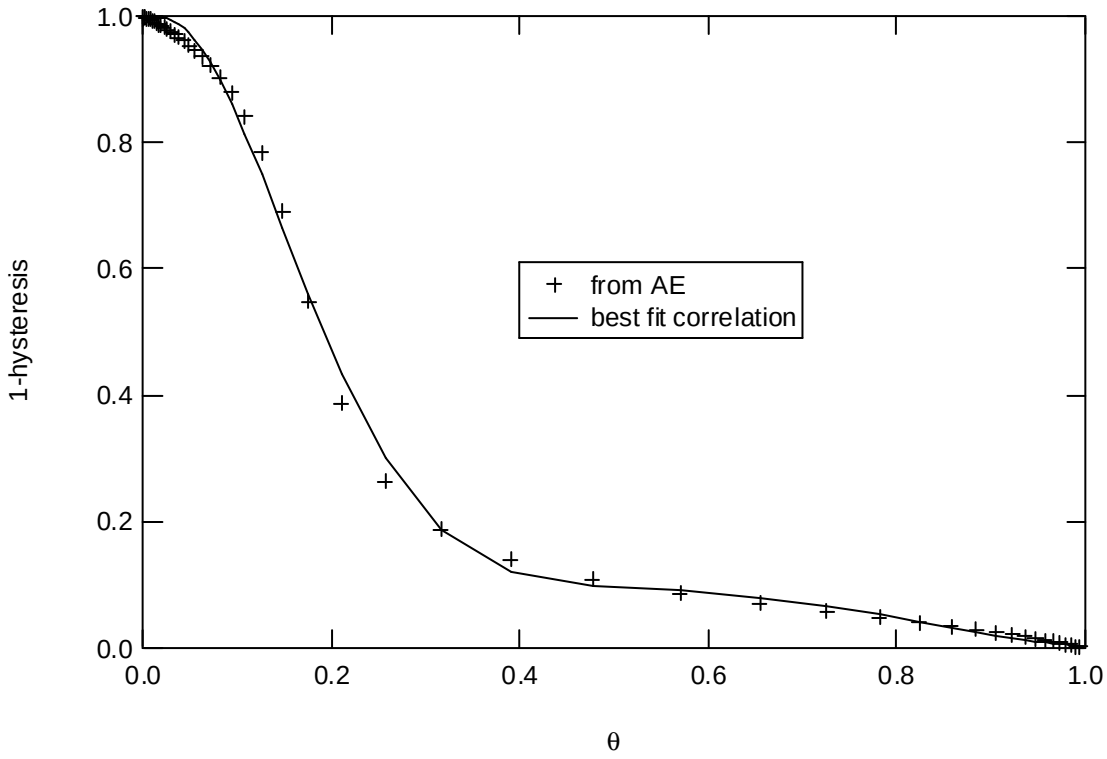

Figure 3-1 Hysteresis correction function for BPL carbon defined by eq. 3.39.

Table 3.1 Hysteresis Correction Factor Parameters

	BPL	Ambersorb 563
F_0	0.9804	0.9907
F_1	1.253	0.1679
F_2	-31.391	-15.52
F_3	101.12	50.862
F_4	-140.84	-71.827
F_5	91.909	47
F_6	-23.033	-11.669

the organic and the water components. For organic vapors described by the Dubinin-Radushkevich equation the heat of adsorption is calculated from eq. 3.6 which can be integrated with respect to the fractional loading

$$H_i^{\text{int}} = \int H_{differential,i}\, d\theta \tag{3.42}$$

This equation can be integrated numerically for the DR model and expressed using a quadratic fit of the form

$$H_i^{\text{int}} = \left(1.68\theta - 0.811\theta^2\right)\beta En_{sat,i} \tag{3.43}$$

which can be used to calculate the integrated heat of adsorption for all vapors described by the DR equation. For water the heat of adsorption is obtained from eq. 2.21. This new Type 5 isotherm allows water coadsorption to be easily implemented. Again a numerical integration of that function can be expressed in quadratic form as

$$H_{water}^{\text{int}} = \left(4.67x10^2\theta - 1.48x10^2\theta^2\right)Rn_{sat,water} \tag{3.44}$$

Figure 3-2 and Figure 3-3 present plots of the differential and integrated differential heat of adsorption versus loading for hexane and water on BPL activated carbon.

Together these equations can be used to construct an adsorption equilibria model. The proposed approach can be implemented with or without iteration given the partial pressure of the mixture components. It would allow limited extrapolation in terms of temperature and concentration changes beyond the range of measured data. It is possible to implement this approach using the Type 5 isotherm expression presented in Chapter 2. This approach differs from that of Manes (1983) by allowing water loadings corresponding to partial pressures less than the organic loading.

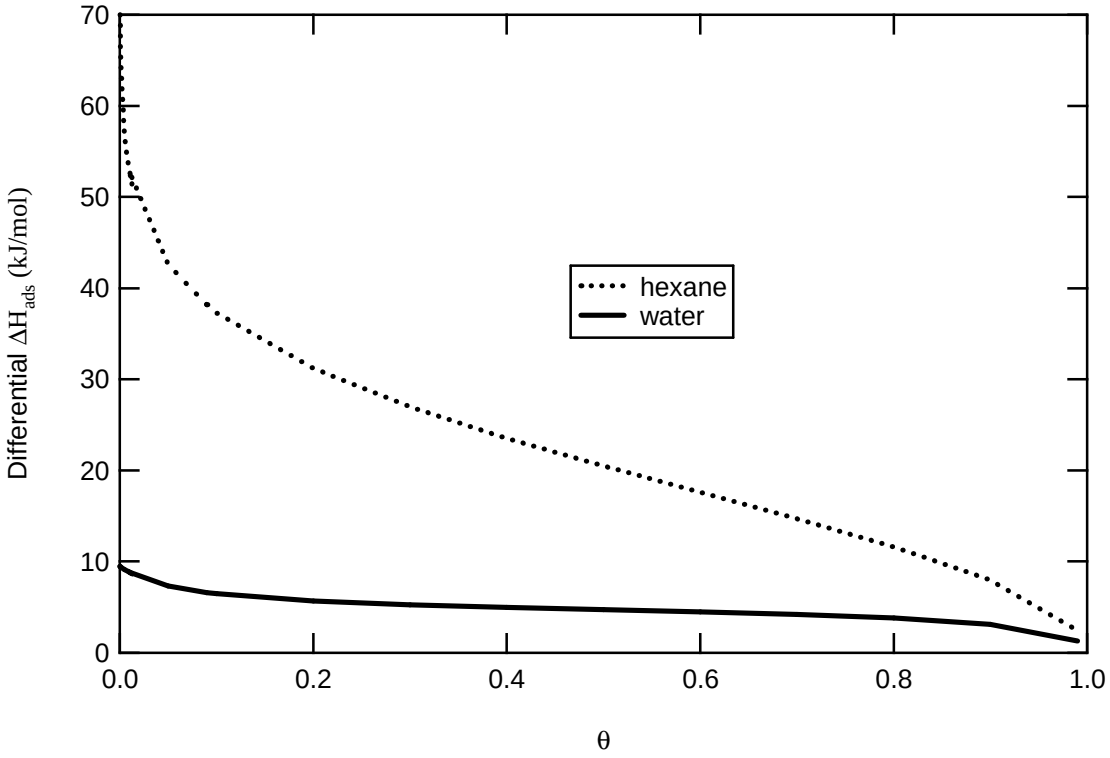

Figure 3-2 Differential heat of adsorption versus fractional pore filling.

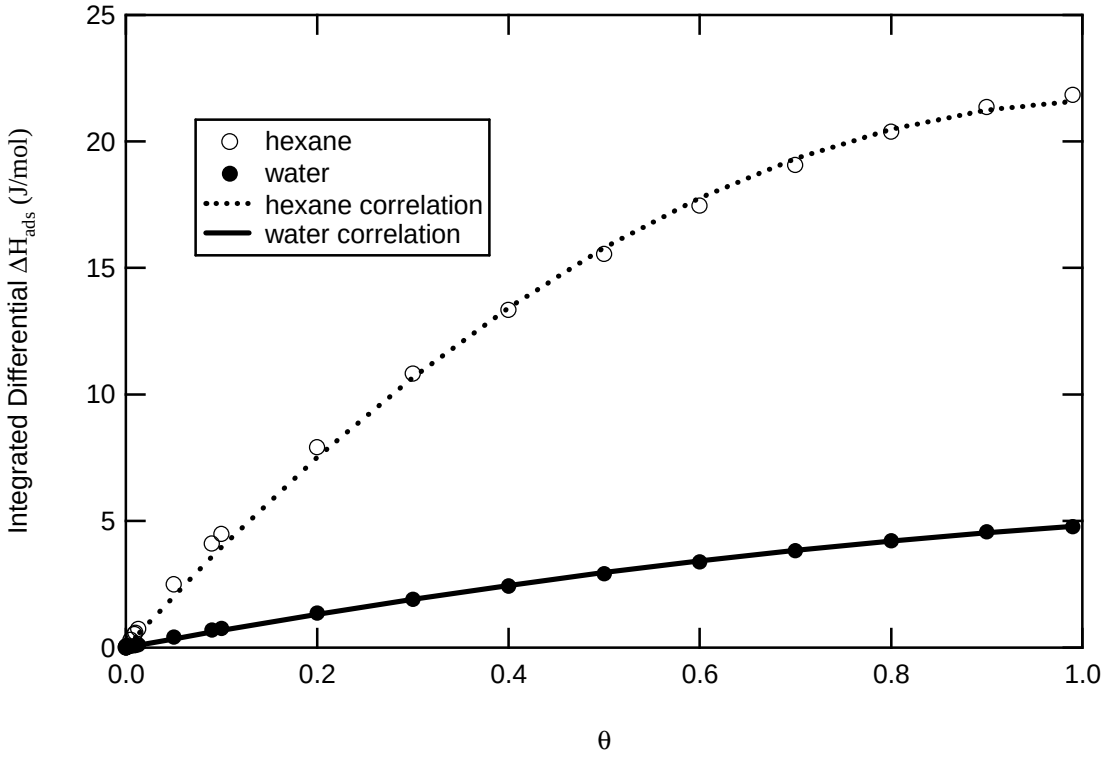

Figure 3-3 Integrated differential heat of adsorption versus fractional pore filling, lines represent best-fit correlation to the numerically integrated result.

Implementation of this approach over a range of temperatures would require that the hysteresis function be calculated which can be done without iteration because of the functional form of the water isotherm.

3.4 Water Organic Coadsorption Experiments

Coadsorption equilibria data can be measured by adopting the same techniques employed for single component measurements. The closed loop apparatus of Mahle et al. (1991) was demonstrated to measure data over a wide range of concentration by performing automated sequential chemical injections and implementing an algorithm for equilibrium determination. Adsorption of high and moderate volatility vapors was reported.

The apparatus, Figure 3-4, consists of a closed recirculating loop. The main loop employs a ballast tank and diaphragm pump. Chemical injections are directed into this loop by shunting a small flow through 1/32 inch tubing to a series of six port valves (Valco Inc.). Sample loops across each of these three valves are filled from a chemical reservoir then alternately directed inline with the flow from the main circulation loop. Similarly chemical analysis is performed by shunting a small flow to a gas-sampling loop of a gas chromatograph. An adsorbent sample of approximately 300 mg is placed in a 3-inch length of 3/8 stainless steel tubing. The adsorbent sample holder is placed in a coiled length copper tubing through which water is circulated from a thermostatic bath. The temperature of the sample is sensed using a thermocouple inserted into the sample holder. Water vapor concentration measurements are obtained from a chilled mirror dewpoint sensor (Edgetech Inc.) which is placed in-line with the ballast loop. System pressures are

determined using a flowthrough transducer (ECI) placed directly downstream of the adsorbent sample in the adsorbent loop. Two four-way valves are used one selects system

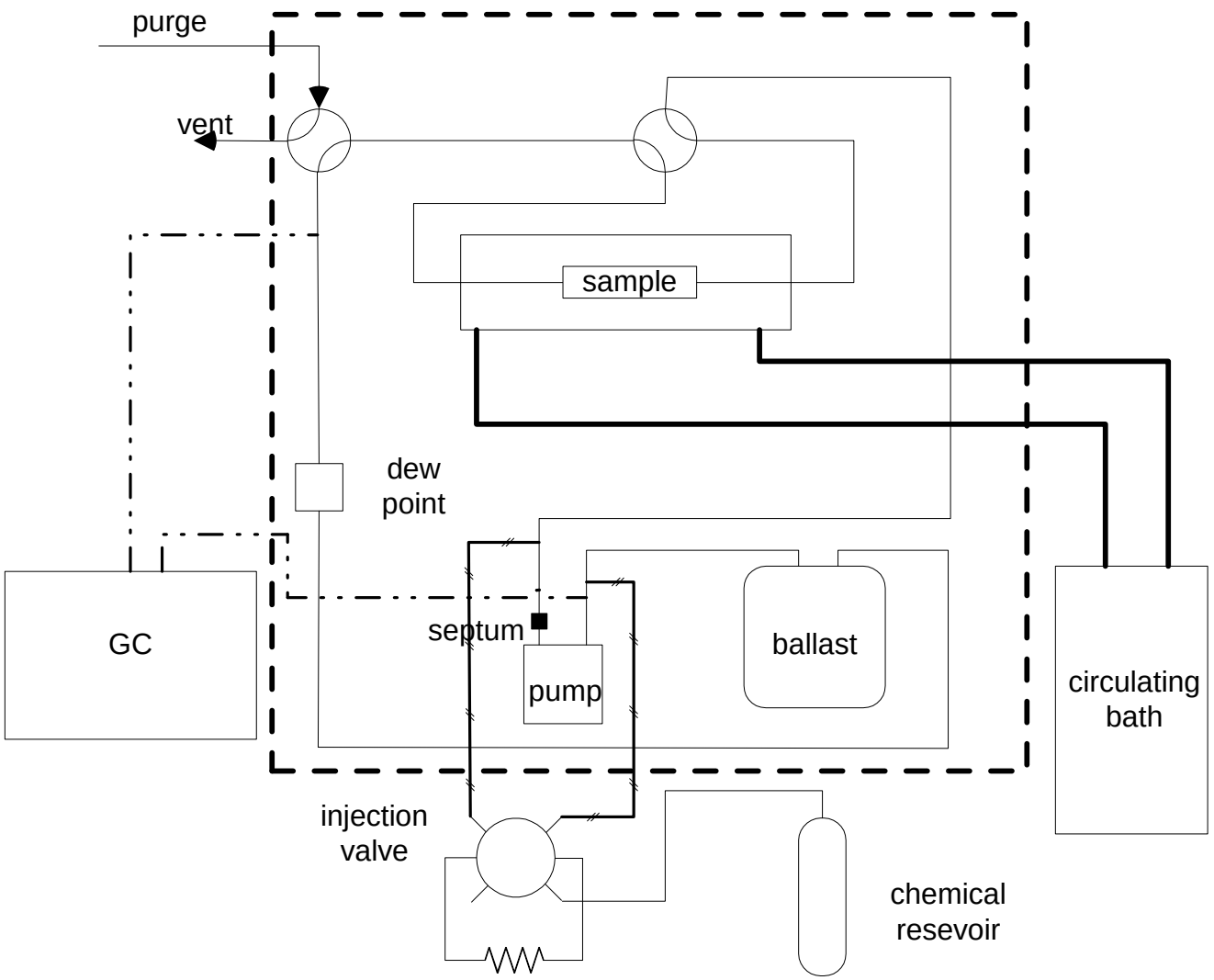

Figure 3-4 Schematic of adsorption equilibria apparatus.

purge or isolation the second places the adsorbent sample either online or in isolation mode.

Several system calibration steps are required. The system sub-volumes are determined by connecting known evacuated volumes and measuring the pressure differences using pressure transducer (Baratron, MKS Inc.). The ballast volume was found to be 6.17 l and the bed volume 0.09 l. The chemical vapor sampling calibration was performed by injecting measured volumes of vapor with a gas tight syringe into the ballast volume. Circulating with the pump equilibrated the mixture in the ballast. Linear calibration behavior was observed over the concentration range using a FID detector on an HP5890 GC. The accuracy of the dewpoint meter was verified by injecting a measured mass of liquid water with a syringe into the ballast volume, which had been purged with dry air (dewpoint < -253 K). The calculated and measured water concentrations agreed within 0.2 K.

Two types of experiments were conducted: either initial equilibration of adsorbent with water followed by subsequent chemical dosages, or initial equilibration with chemical vapor followed by subsequent water dosages. The former had been implemented as an automated algorithm using Labview based PC control. The latter was performed manually. In both cases the water injections were performed manually by measuring the mass of injected water. The purge gas for all experiments was dry air.

3.5 Results

Measured data from the volumetric adsorption equilibria apparatus and other sources is analyzed using the coadsorption model developed above. Two adsorbents are considered: BPL and Ambersorb 563. The former is a highly porous commercial gas phase adsorbent

derived from activated coal, the latter a synthetic carbonaceous adsorbent used in VOC removal. Some selected physical properties of chloroethane together with other adsorbates for the immiscible coadsorption pairs are listed in Table 3.2. Both chloroethane and dichloromethane possess the highest solubility of approximately 1 wt%. The water adsorption correlation parameters using the Type 5 isotherm model of Chapter 2 are listed in Table 3.3. Note the much reduced water capacity of Ambersorb 563 versus BPL carbon.

Measured adsorption data for chloroethane on the two adsorbents at 298 K was obtained using the volumetric apparatus. Figure 3-5 and Figure 3-7 present pure and multicomponent loadings as a function of partial pressure for chloroethane on the two adsorbents BPL carbon and Ambersorb 563. The water adsorption data obtained in the same experiments is presented in Figure 3-6 and Figure 3-8. In order to plot both chloroethane and water pure component loading corresponding to the mixture partial pressure the pure component loadings were obtained from a correlation of the pure component data. Two types of experiments were conducted consisting of either sequential injection of chloroethane or sequential injection of water. The largest effect of coadsorption on chloroethane loading is seen to be at lowest chloroethane loadings, with pure component loadings approached at higher partial pressures. The relative effect of coadsorption is seen to be much less on Ambersorb 563 as compared to BPL at similar vapor phase water concentrations. This is consistent with the observation that the water isotherm of Ambersorb 563 shows one-third the saturation capacity of BPL while the pure component chloroethane capacity on each adsorbent is nearly the same.

Table 3.2 Adsorbate properties.

	Water solubility (wt%)	H_{vap} (kJ/mol at 298 K)
chloroethane	0.447	$2.4x10^2$
dichloromethane	1.3	$2.8x10^2$
hexane	0.014	$3.0x10^2$
CFC-113	0.017	$3.0x10^2$
propane	0.013	$1.4x10^2$
ethane	0.013	4.0

Table 3.3. Water adsorption isotherm correlation parameters for BPL and Ambersorb 563 at 25ºC.

	A	B	n_{sat}
BPL ads	0.55	0.12	22
BPL des	0.48	0.064	22
Ambersorb 563 ads/des	0.65	0.20	7.1

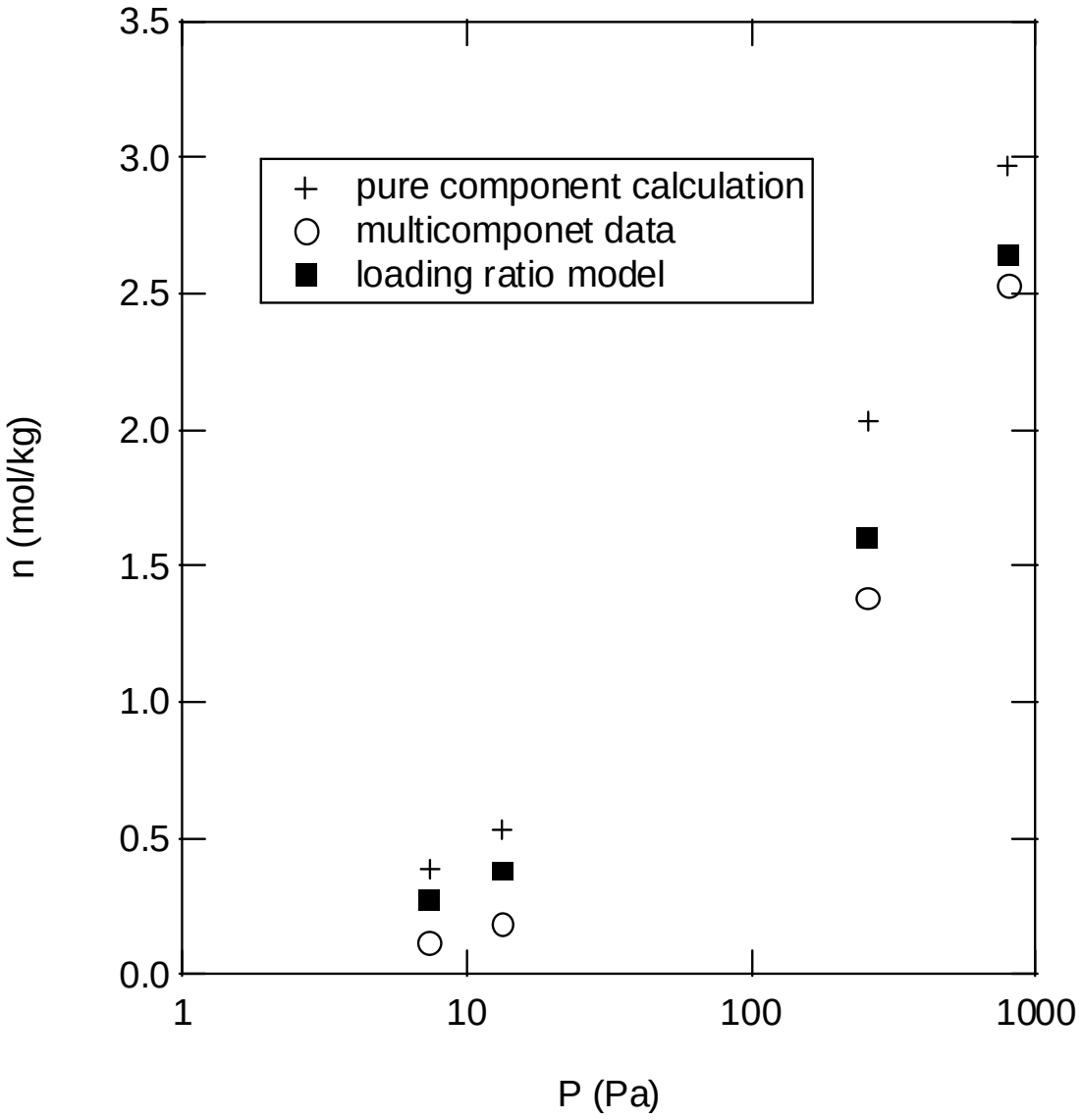

Figure 3-5 Chloroethane adsorption loading versus partial pressure on BPL carbon for pure component (obtained from correlation of pure component data), coadsorption with water data and predicted values from the enthalpy ratio model.

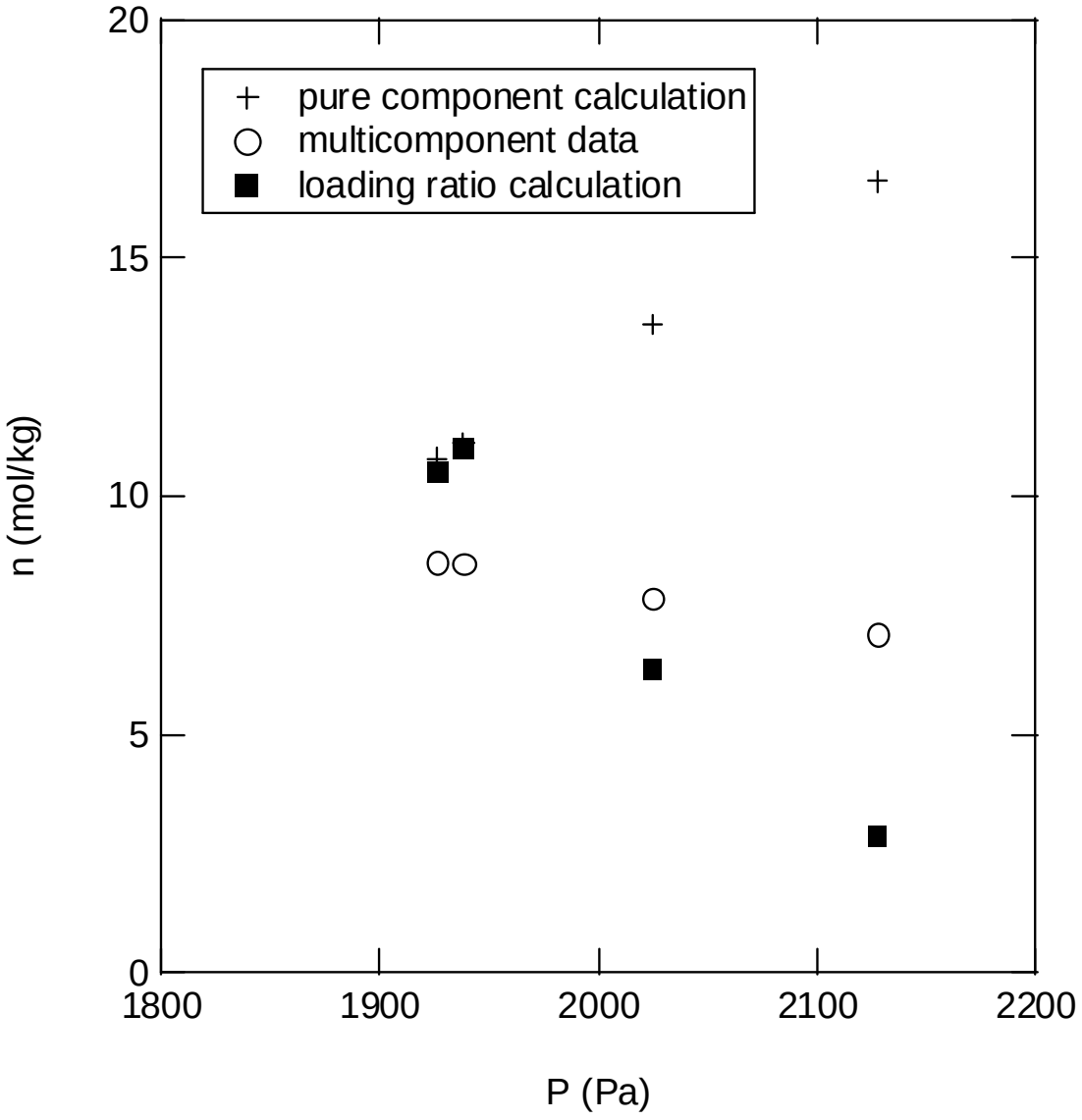

Figure 3-6 Water adsorption loading versus partial pressure on BPL carbon for pure component (obtained from correlation of pure component data), coadsorption with water data and predicted values from the enthalpy ratio model.

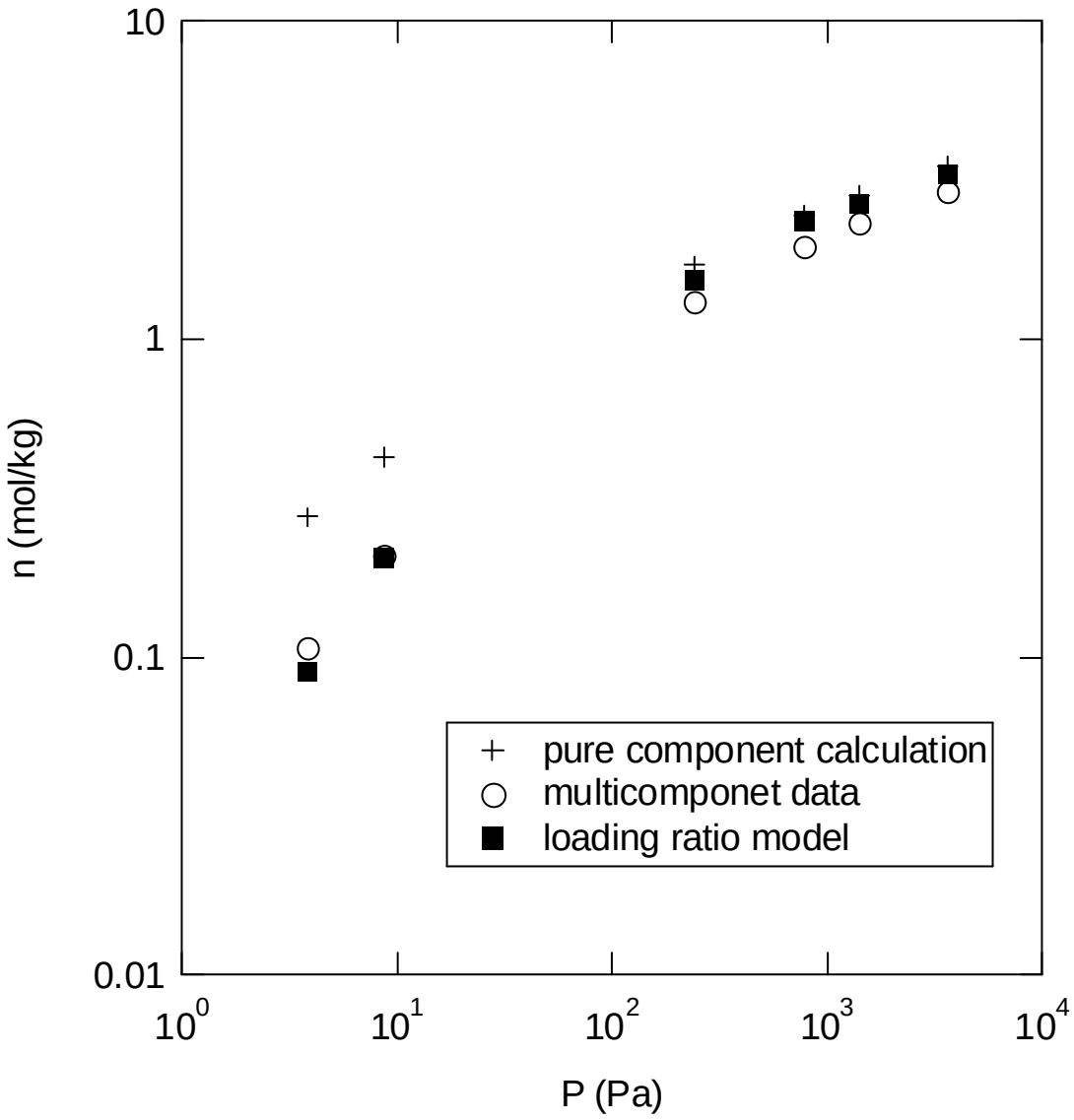

Figure 3-7 Chloroethane adsorption loading versus partial pressure on Ambersorb 563 carbon for pure component (obtained from correlation of pure component data), coadsorption with water data and predicted values from the enthalpy ratio model.

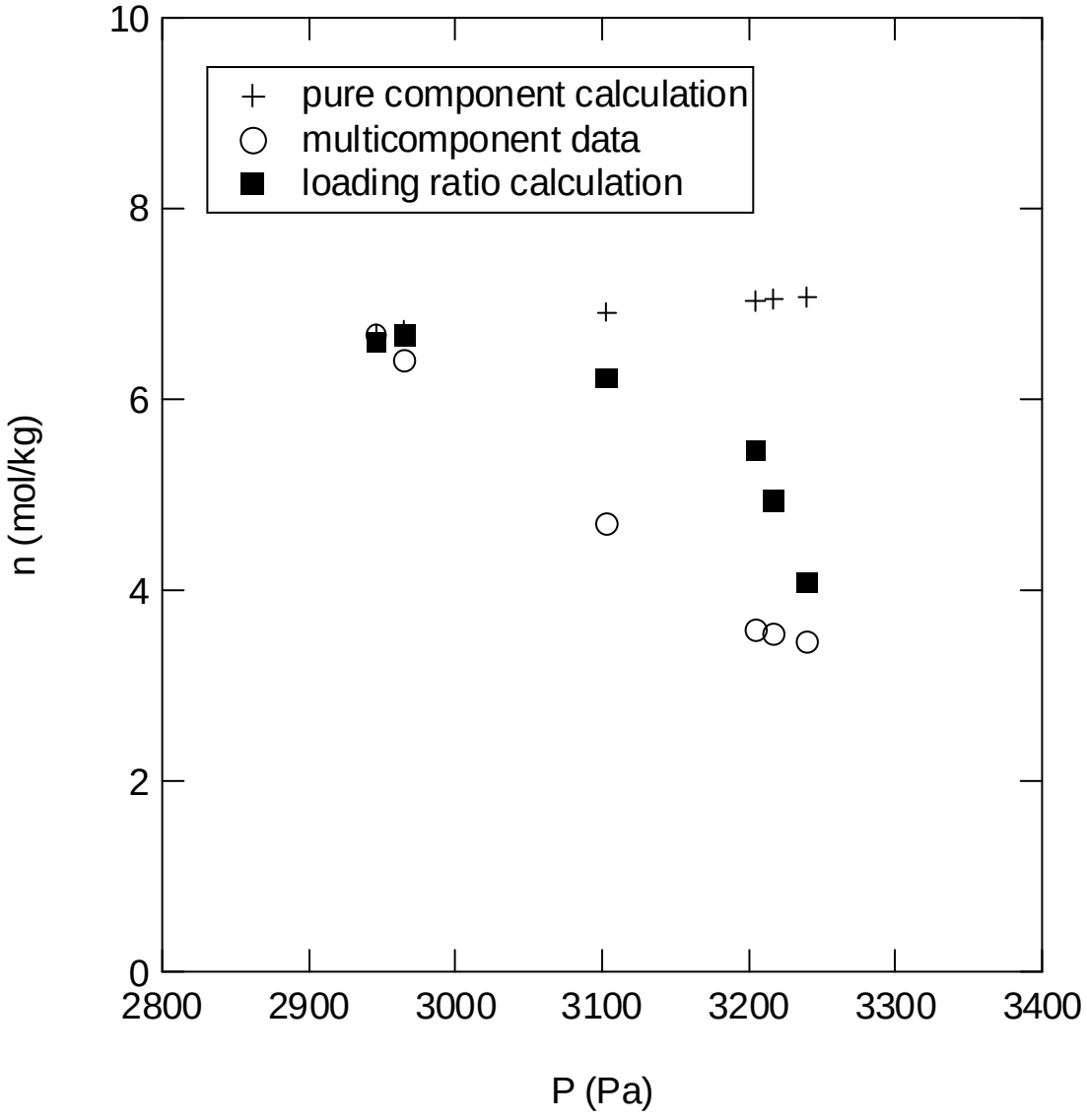

Figure 3-8 Water adsorption loading versus partial pressure on Ambersorb 563 carbon for pure component (obtained from correlation of pure component data), coadsorption with water data and predicted values from the enthalpy ratio model.

The effect of the order of adsorption of water and organic was investigated using the chloroethane and water system. Figure 3-9 presents stacked plots of partial pressure of water, chloroethane loading and water loading versus chloroethane partial pressure. There are both organic loaded first and water loaded first data. By locating the point of intersection of the various data sets it is possible to interpolate to a condition where the partial pressure of water and organic would be the same for the two experiments. It is then possible to note the corresponding chloroethane loading from both the water first and organic first experiments. For instance at a chloroethane partial pressure of 6 Pa an intersection is noted for the water and chloroethane partial pressure curves. However the organic loadings, 0.2 mol/kg for the chloroethane first and 0.05 mol/kg for the water first runs, do not agree from these two experiments. The greater adsorption of the organic first case is observed for all the cases. Clearly this path dependent equilibria behavior would be impossible to incorporate in an equilibrium model that does not employed path history dependence.

In addition to the data for chloroethane several other immiscible coadsorption data sets were examined using the multicomponent model described by eq. 3.28-3.39. These data sets (hexane, dichloromethane, CFC113, propane and ethane) are useful in that they were measured on the adsorbent, BPL activated carbon. The organic pure component adsorption DR correlation parameters are listed in

Table 3.4. In order to implement the enthalpy ratio model the pure component enthalpy terms needed to be calculated. In the present case the partial pressures for a

given mixture are selected then the pure component loadings for water and organic are calculated. Based on those pure

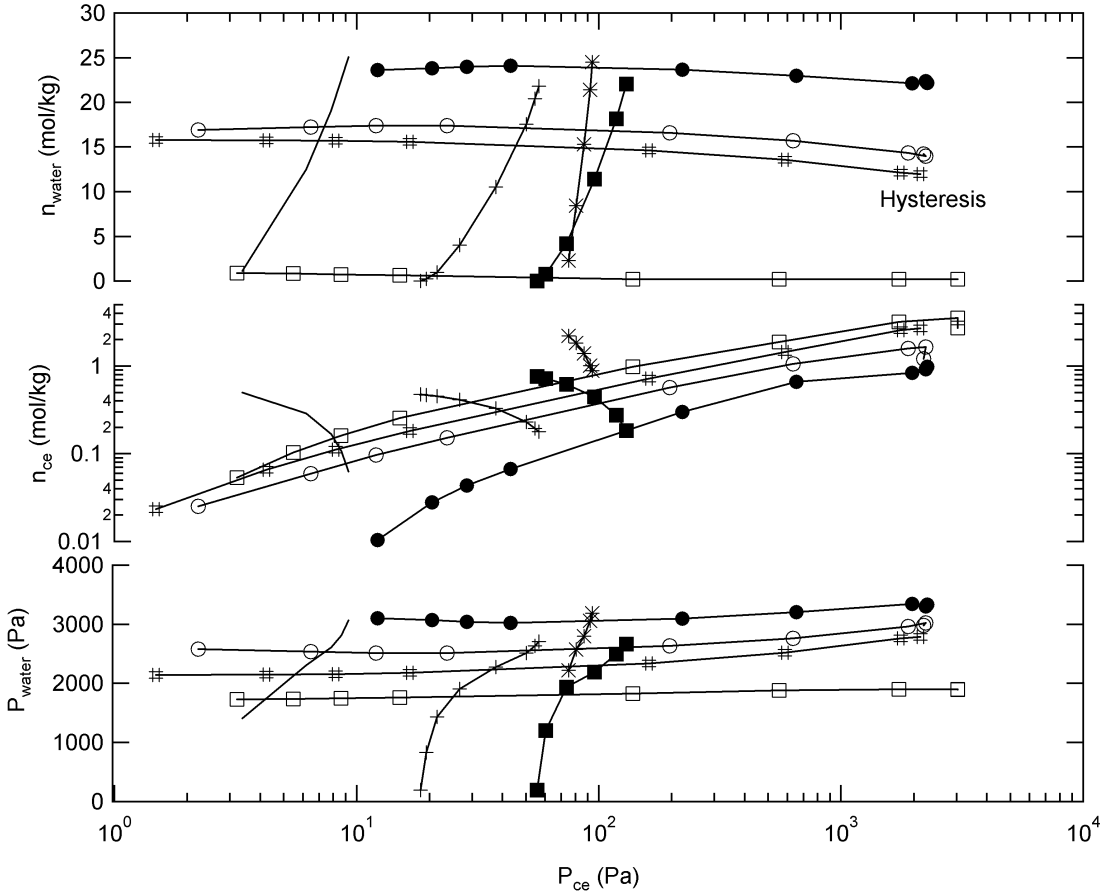

Figure 3-9 Compilation of humid chloroethane adsorption data on BPL carbon at 298 K, partial pressure of chloroethane versus partial pressure of water, chloroethane and water loading.

Table 3.4 Pure organic component adsorption parameters

	adsorbent	Wo (cm^3/kg)	βE/R (K)	n
CFC113	BPL	477	2437	2
hexane	BPL	477	2860	2
dichloromethane	BPL	477	1477	2
propane	BPL	477	1863	2
ethane	BPL	477	1440	2
chloroethane	BPL	477	1764	2
chloroethane	Ambersorb 563	357	1853	2

component loadings the fractional loading of organic is determined. The residual is defined as

$$\text{Re}\,sidual = \sum (n_i - n_{i,\exp}) / n_{\exp} \tag{3.45}$$

keeping with the work of Russell and LeVan (1997). Both organic and water data is included in the residual calculation.

The proposed approach to describe multicomponent equilibria can be summarized by three rules (1) calculate the organic correction based on the enthalpy ratio between the organic phase and the water phase, (2) apply a correction factor to the pure component loading calculated at the mixture partial pressure, (3) calculate the water loading correction based on the intrusion of organic into the hysteresis region. The model equations can lead to a non-iterative solution starting from the partial pressures. However the results can also be refined through an iterative solution by employing the calculated organic loading in the heat of adsorption calculation for water rather than the pure component organic loading. It is found that this iterative approach provides a better agreement with the measured data as compared to the result obtained using the mixture organic loading.

These concepts have been implemented using the measured coadsorption data. The hysteresis correction factor was presented in Figure 3-1. It is possible to calculate the predicted water loading using the pure component water loading, and the hysteresis factor equation based on the experimental organic loading. The accuracy of the loading ratio model can be seen by comparison with measured data. Again the reported loading from the loading ratio model is reported at the mixture partial pressure. Model results for chloroethane and water on BPL carbon are shown in Figure 3-5 and Figure 3-6. There is good qualitative agreement between the coadsorption data and the model for

chloroethane. The largest deviation occurs and the lowest loadings for both chloroethane and water. Figure 3-10-Figure 3-13 present both the measured adsorption results and model predictions for both hexane and dichloromethane with water on BPL. Good agreement is noted over the range of relative pressure for all three systems. Similar agreement was observed for the other systems considered where the organic component of the mixture was equilibrated first and water was allowed to adsorb later and also where the relative humidity was less than approximately 70%. Some error in multicomponent mixture prediction was observed for samples of BPL carbon equilibrated initially at high relative humidity. The model under-predicted the effect of water on chloroethane adsorption and over-predicted the effect of chloroethane on water adsorption. This is consistent with the observed hysteresis effects. A revised form of the model is thus required which inputs the prior history of adsorbent conditioning.

The calculated residuals of the power law method of Russell and LeVan (1997), Table 3.5 are in good agreement with those of the present model Table 3.6. A comparison of the predicted results with measured data is shown in Figure 3-14 for chloroethane. It must be noted that the results for propane and ethane have been obtained using a correction factor to the heat of adsorption. Since the heat of vaporization tends to zero as the critical point is approached the heat of adsorption can be assumed to behave similarly. The heat of adsorption cannot be obtained from the pure component data because the temperature range is narrow. Good agreement between the measured data and the model for ethane and propane is obtained if the heat of adsorption is reduced by a factor 0.2 relative to that obtained from the differential heat of adsorption predicted from the DR relationship.

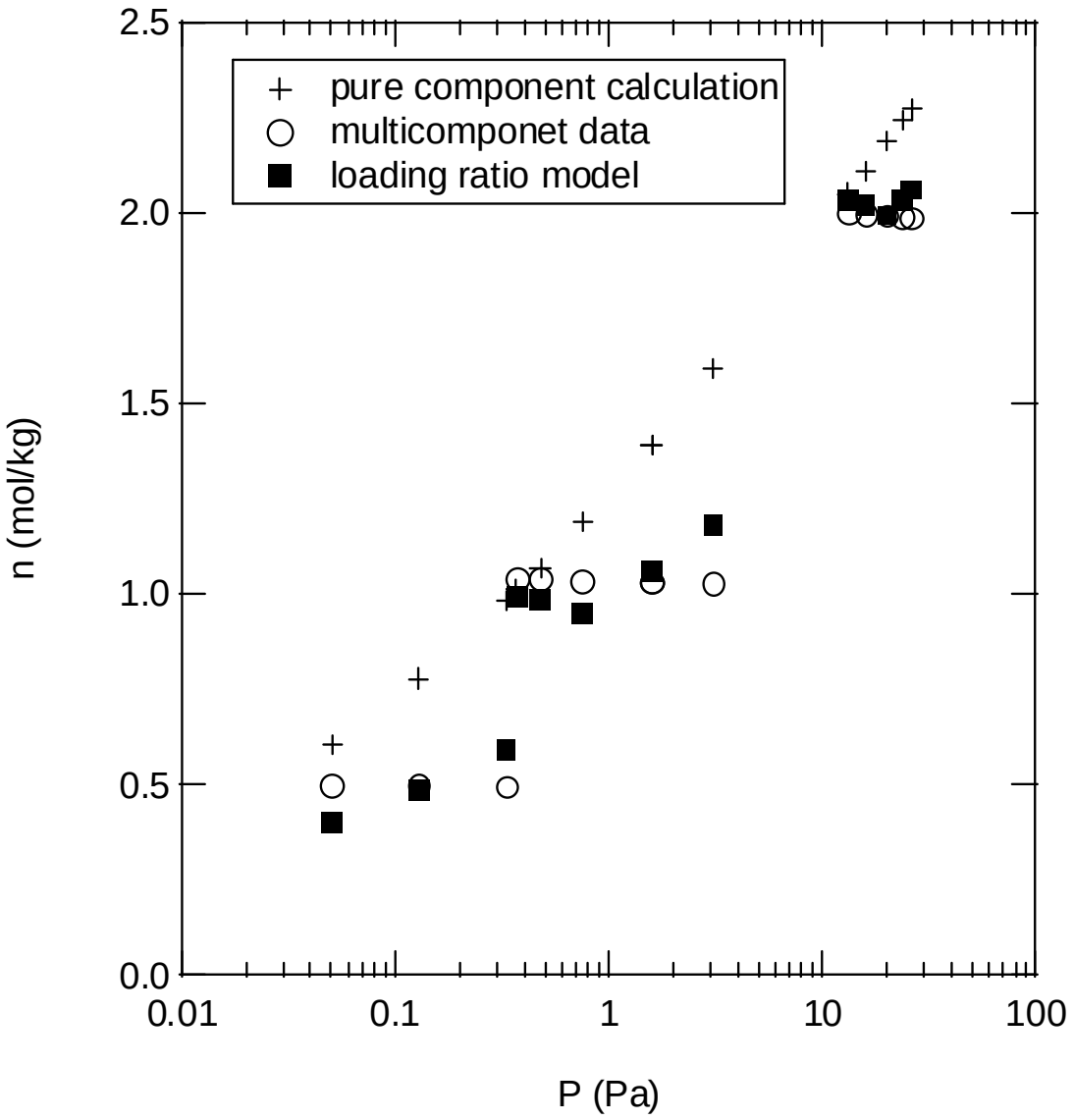

Figure 3-10 Hexane adsorption loading versus partial pressure on BPL carbon at 298 K for pure component data (obtained from correlation of pure component data), coadsorption with water data (Rudisill and LeVan(1992)) and predicted values from the enthalpy ratio model.

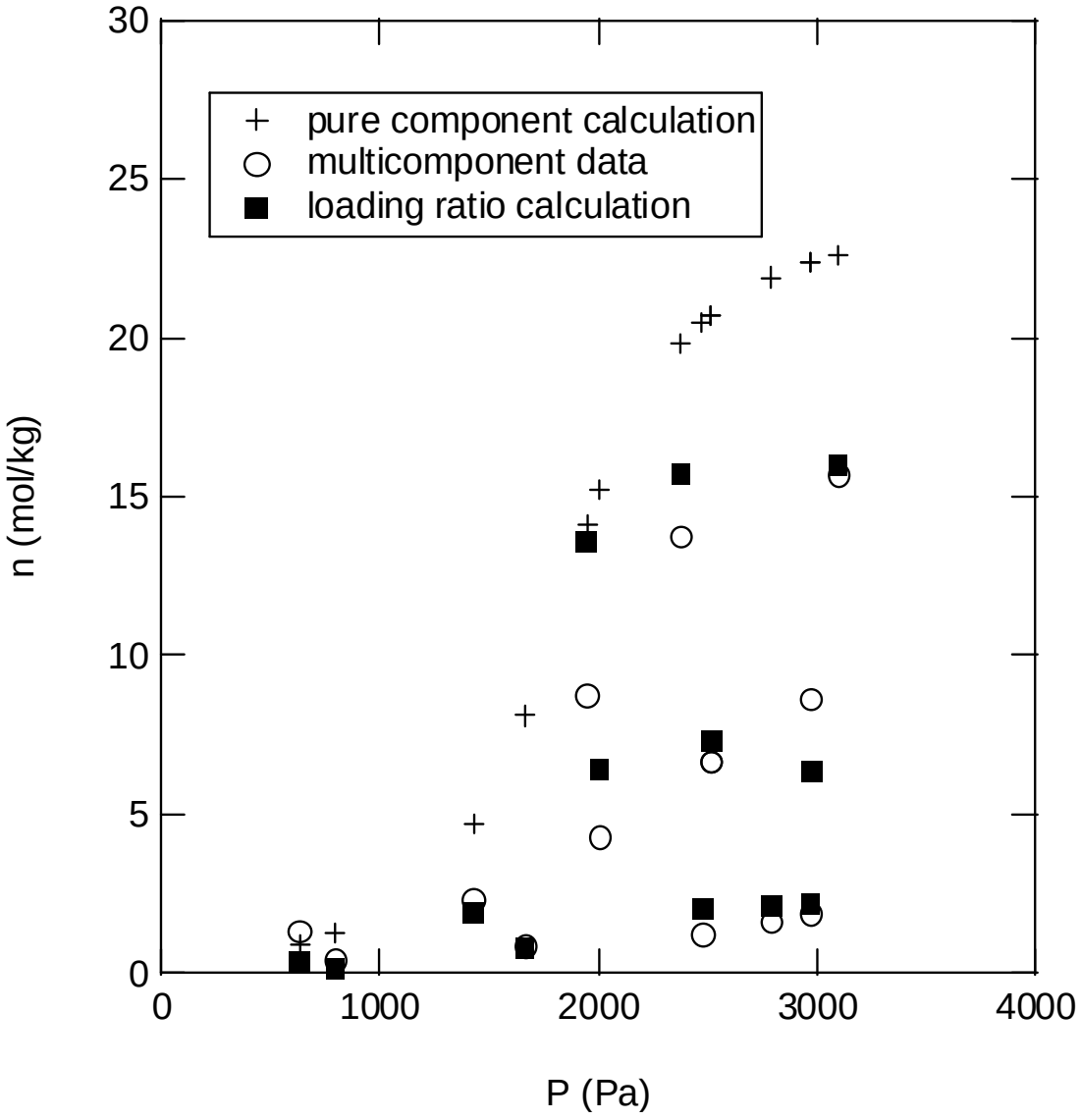

Figure 3-11 Water adsorption loading versus partial pressure on BPL carbon at 298 K for pure component data (obtained from correlation of pure component data), coadsorption with hexane data (Rudisill and LeVan (1992)) and predicted values from the enthalpy ratio model.

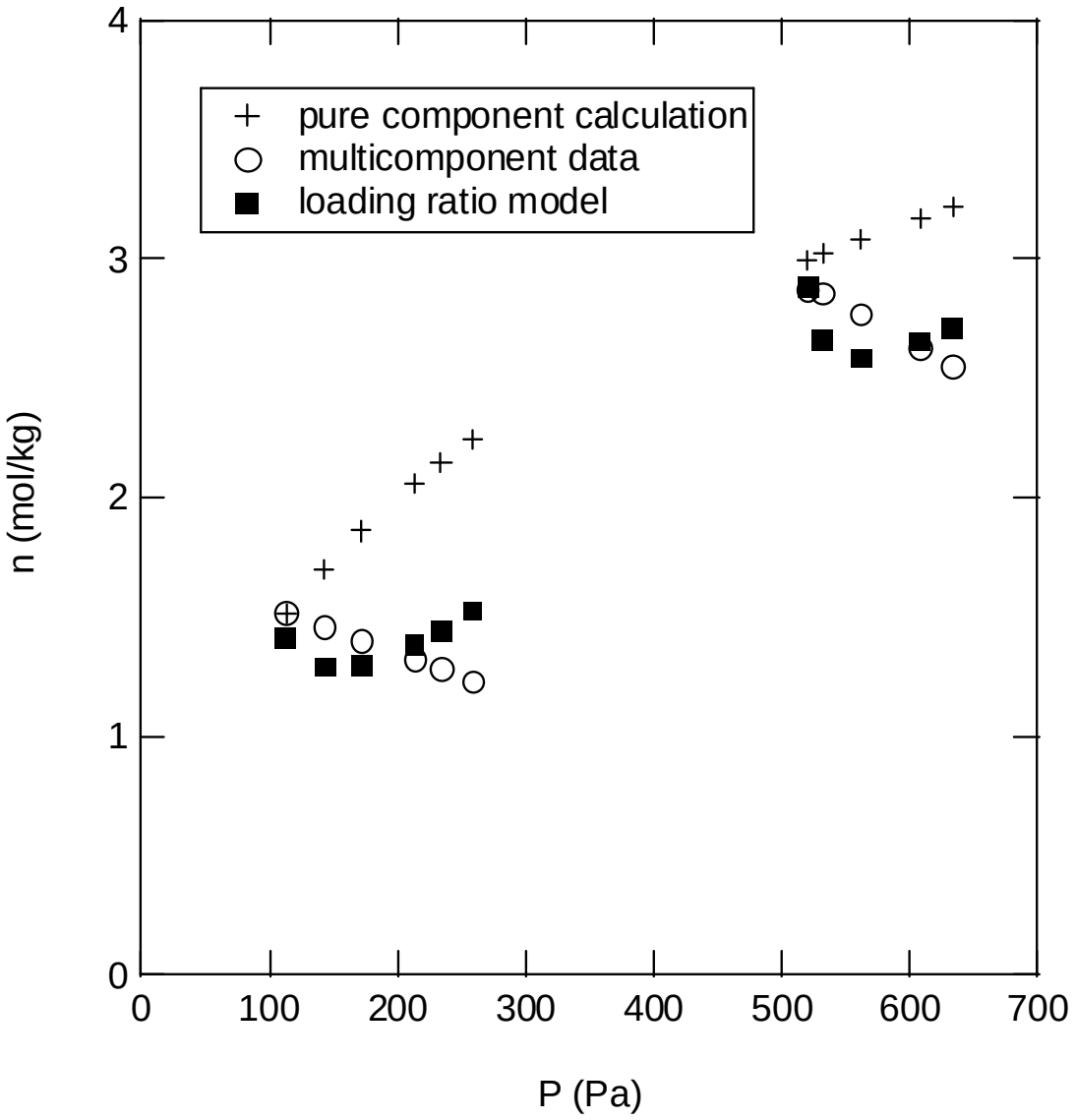

Figure 3-12 Dichloromethane adsorption loading versus partial pressure on BPL carbon at 298 K for pure component data (obtained from correlation of pure component data), coadsorption with water data (Eissmann and LeVan (1993)) and predicted values from the enthalpy ratio model.

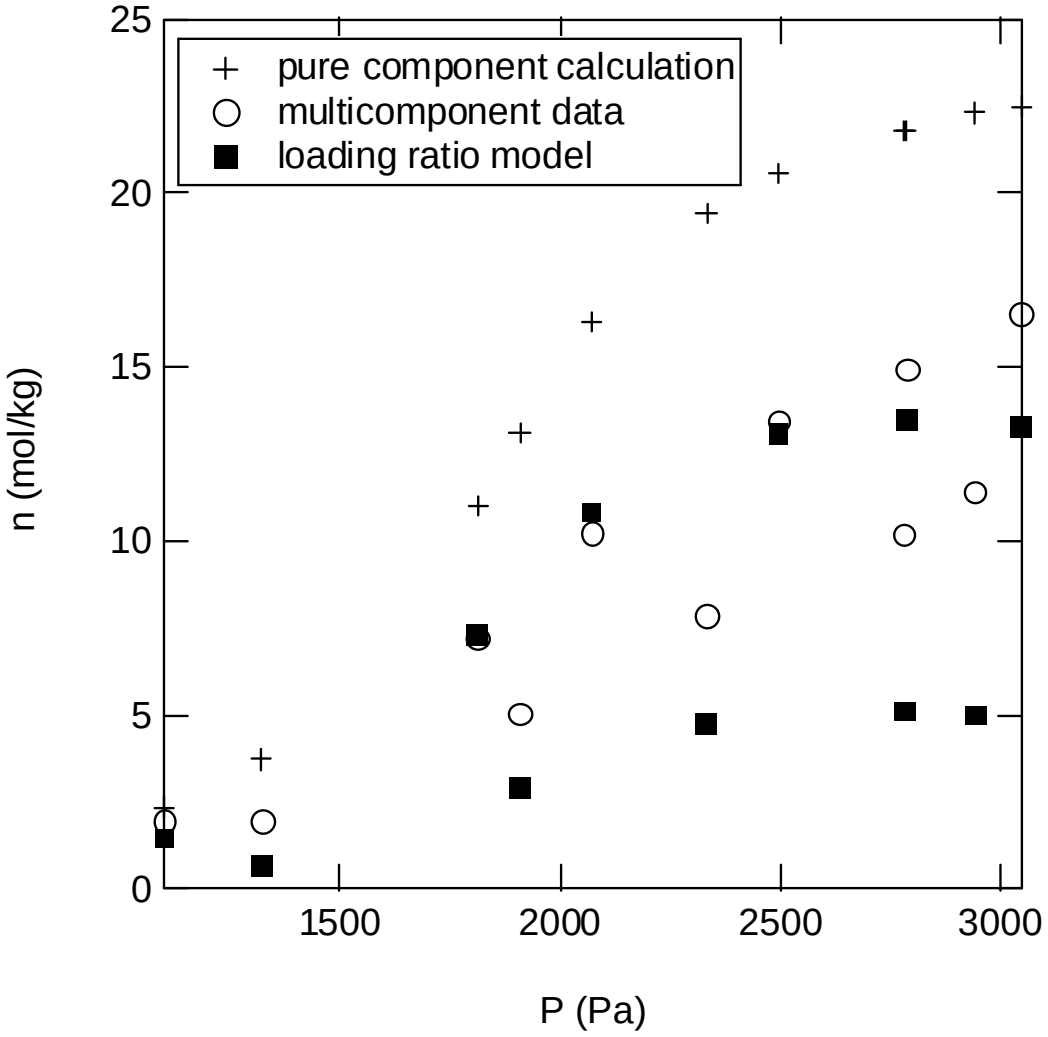

Figure 3-13 Water adsorption loading versus partial pressure on BPL carbon at 298 K for pure component data (obtained from correlation of pure component data), coadsorption with dichloromethane data (Eissmann and LeVan (1993)) and predicted values from the enthalpy ratio model.

Table 3.5 Residuals for power law model.

Adsorbate Pair	*Adsorbent*	R_i	R_w
CFC113-water	BPL	37	36
hexane-water	BPL	16	46
dichloromethane-water	BPL	9.8	20
propane-water	BPL	11	41
ethane-water	BPL	16	30

Table 3.6 Residuals hysteresis coadsorption model based iteration.

Adsorbate Pair	Adsorbent	R_i	R_w
CFC113-water	BPL	14	44
hexane-water	BPL	9	32
dichloromethane-water	BPL	7	29
propane-water	BPL	14	54
ethane-water*	BPL	9	31
chloroethane-water	BPL	39	51
chloroethane-water	Ambersorb 563	12	25

* enthalpy of ethane adsorption taken as 0.2*DR model prediction

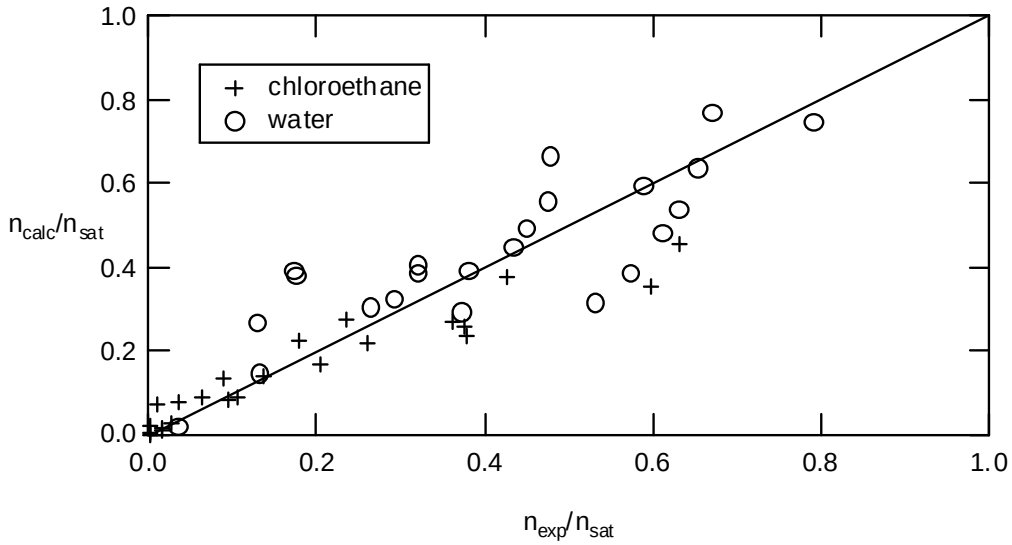

Figure 3-14 Comparison of the enthalpy ratio model and data of the relative loading of chloroethane/water coadsorption on BPL carbon.

For the case of chloroethane adsorption on Ambersorb 563 the saturation capacity for water and chloroethane differed. The saturation volume for chloroethane was 357 cm^3/kg while for water it is 126 cm^3/kg. The pore structure for Ambersorb 563 is known to exhibit a narrow distribution, which would further limit close packing. For a given heat of adsorption some species occupy a larger adsorbed volume, leaving less volume for water adsorption. Using the approach described for BPL to predict adsorption behavior was not possible because of the difference in saturation capacity. A modified approach for Ambersorb 563 has been developed where the heat of adsorption of water in eqn 3.17 is corrected by fractional loading of water based on the organic saturation volume rather than the fractional loading of organic based on the organic saturation volume. This is seen to give excellent agreement for both data sets. Similarly the correction for water loading is obtained calculating the hysteresis correction factor using the organic loading multiplied by the ratio of the saturation volume of water over the saturation volume of organic. This modified approach for water adsorption is also seen to provide good agreement for both data sets. The residuals for chloroethane and water adsorption on Ambersorb 563 are listed in Table 3.6. Part of the reason that these residuals are lower than was observed with BPL is that the coadsorption effect is less on Ambersorb 563.

There were a small number of coadsorption experiments performed. The reproducibility of the data could only be evaluated from two experiments with overlapping conditions. These results are shown in Figure 3-15 for chloroethane and water loading. Comparison of this limited data suggest approximately 20% variation in CE loading and 5% variation in water loading.

Analysis of the model sensitivity was conducted. There are not correlation terms in the model for which standard parameter sensitivities can be calculated, rather the effect

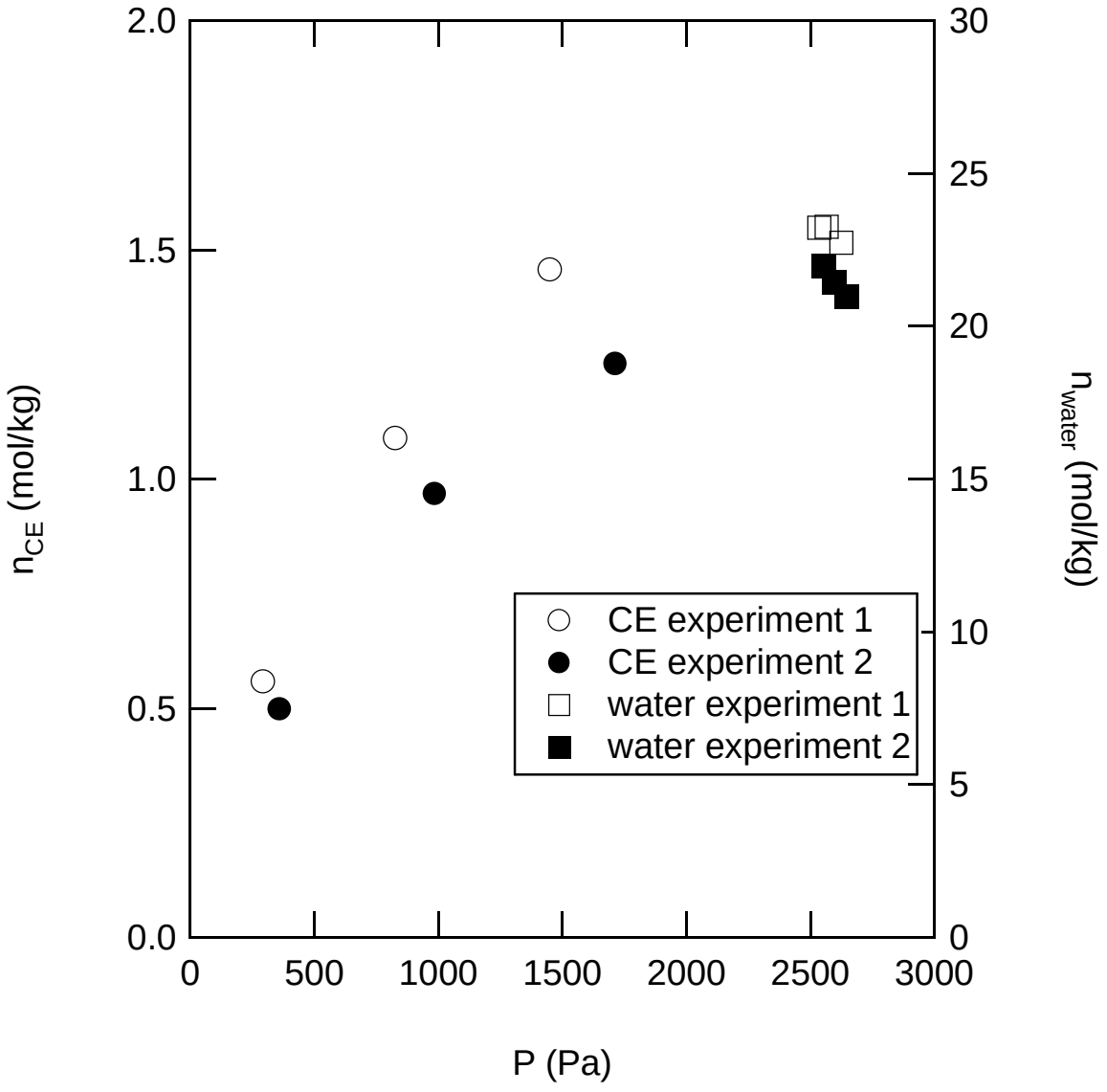

Figure 3-15 Two repeat coadsorption runs for chloroethane on BPL carbon.

of variation in computed inputs is considered. Given the mixture partial pressure the model can be reduced to five input terms: (1-4) pure component loading and heat of adsorption of organic and water, (5) hysteresis factor. A base case condition was chosen, dichloromethane-water on BPL carbon. The effect of a 20% change in each of the input terms (1-5) was then examined for the impact on the computed value of both the organic and water loading. The predicted values of the enthalpy ratio model for the eleven data points were used to calculate a deviation variable, based on a normalized absolute value

$$\delta_{Dev} = \frac{abs(n_{calc} - n_{base})}{n_{base}} \tag{3.46}$$

The sum of the deviation variables was then calculated

$$\sigma = \frac{\sum \delta_{Dev}}{N} \tag{3.47}$$

The calculated values of σ for both dichloromethane and water are presented in Table 3.7. These results indicate that both the organic and water loading are not very sensitive to the heat of adsorption calculation, but the water loading is very sensitive to the hysteresis function. Also the computed loadings are highly dependent on the pure component loading more so than a linear dependence, because a linear dependence would result in a 0.2 value for σ.

Future work would include measurement of more data especially for the case where equilibria is compared for organic pre-adsorption and water pre-adsorption in the same partial pressure regime. Further work to refine this approach would include accurate measurement of the heat of adsorption for water on activated carbon, evaluation of the model at other temperatures, and the estimation of the packing efficiency of larger molecules in micropores. Also a refinement of the hysteresis correction factor can be made if the hysteresis of the water behavior can be correlated for intermediate water

Table 3.7 Sensitivity values for Enthalpy Ratio model.

	σ_{MeCl}	σ_{water}
$\Delta H^{\text{int}}_{ads,diff,MeCl}$	0.048	0.063
$\Delta H^{\text{int}}_{ads,diff,water}$	0.058	0.084
$n_{pure,MeCl}$	3.01	355
$n_{pure,water}$	0.36	2.8
$F_{\text{hysteresis}}$	0.058	0.30

loadings. Because water adsorption exhibits a sharp transition it will always be difficult to model the water behavior accurately.

3.6 Conclusions

A study of multicomponent adsorption equilibria has been presented. The particular case of coadsorption of water with immiscible vapors was considered from three perspectives: review of prior experimental systems and coadsorption models, measurement of coadsorption data and description of a novel coadsorption model. Multicomponent data was measured using a closed loop volumetric system for chloroethane and water.

A new semi-empirical model has been proposed here. It is derived by assuming that a correction factor for the pure component loading is a function of the relative heats of adsorption. This new coadsorption model uses only one parameter, which is only required for weakly adsorbed vapors. It has been show to describe multiple data sets representing a wide range of isotherm favorability and relative pressure. Model shows good agreement with measured coadsorption data.

Chapter 4: Studies of Temperature Swing Adsorption

4.1 Background

Air purification applications are associated with removal of trace concentrations of contaminants. Efficient operation requires a high throughput process with modest energy demand. Under certain applications additional constraints may be imposed such as limited size for integration of a device within a larger process. Most common among the air purification systems are driers. At ambient temperatures the water content of air is no more than a few percent. Water vapor removal requirements for driers can vary from one to three orders of magnitude. Additional contaminants introduced as either a constant low-level emission or an intermittent pulse may be present along with water.

The selective removal of these vapor components may be achieved with or without the associated removal of water vapor. High selectivity in vapor phase separations with minimal energy input can be achieved through adsorption processes. Alternative separation processes such as membranes and absorption typically fail to offer the efficiency or scalability of the adsorption alternative. Cyclic regenerative adsorption processes have been developed which provide increased capacity and selectivity compared to single pass filters. A system may or may not reach a steady state (periodic state) at the feed conditions.

Cyclic adsorption processes must operate so that the feed step is conducted short of breakthrough, followed by countercurrent or co-current regeneration. Pressure swing adsorption systems are well suited to light gas separations due to a significant loading difference resulting from a partial pressure change. Thermal regeneration is favored when the adsorbed concentration does not significantly vary with partial pressure or the cost of

mechanical compression is significant. The former is often the case when the feed component is present in low concentration and the isotherm is strongly concave downward. Typically it is achieved by either steam or convection heating of packed beds. The convection approach can be implemented by a wide variety of techniques such as heating elements embedded in the adsorber, heated purge, gas fired heat input where hydrocarbon combustion is used to directly or indirectly heat a purge stream.

Many parameters influence the behavior of a thermal swing process. The quantity of purge flow is related to the adsorbent mass if the velocity in the adsorption step is fixed. Knowledge of this relationship is necessary for optimization. Bed depth, velocity and cycle time for an adiabatic system are not independent but represent the number of column volumes of processes gas. If the amount of energy input is represented by the time for heating then an objective would be to minimize the heating fraction of the purge step and the number of purge column volumes or if the heating to cooling time is fixed then only the purge column volumes is minimized.

Numerous authors have studied thermally regenerated adsorption systems. These systems are best described by considering each adsorption column as undergoing a series of steps. The progress of all steps results in a cycle. The various adsorption columns are connected and this represented on a flowsheet. Most early papers discussed single bed adiabatic behavior. For example Friday and LeVan (1985) examined benzene recovery. Davis and LeVan (1989) presented both experimental and modeling studies of the complete regeneration of n-hexane from air using countercurrent purge. The results suggested that short heating times at higher temperatures was most effective in reducing the overall heating duty. Earlier Davis and LeVan (1987) had found that proper timing of

the cooling step could reduce heating requirements. That work concerned solvent recovery and the application to trace gas removal was not discussed. Schweiger and LeVan (1993) examined hexane recovery using steam, but did not consider cycling. Davis and LeVan did not employ a multi-bed system.

Process design is dependent on adsorption equilibria. Optimized adsorbent columns often employ layered adsorbents. Pigorini and LeVan (1997) examined the layering scheme for pressure swing adsorption systems. It was shown that less favorable equilibria could lead to increased throughput performance. The corresponding rules for adsorbent layering of thermally regenerated systems are not well recognized. The heater placement relative to the adsorbent layers must be considered. Ahn and Lee (2003) examined air drying by thermal swing adsorption with a layered bed. An approach to reduce adsorber sizing based on dimensional analysis was discussed by Wankat (1987). The reduced bed length was obtained through rapid thermal cycling and reduced particle size. The affects of adsorber heat losses on bed sizing were also examined by a similar approach, (Chen, 1991).

Inefficiencies arise when rapid thermal cycling is desired. Only a small fraction of particles contact other particles and large bed voidage of granular packed adsorbent columns leads to low thermal and electrical conductivity of conventional adsorption beds. A limitation associated with the heat capacity of air tends to result in long heating and cooling steps and large adsorbent inventories. Increased heat input for bed purging can reduce the purge gas requirement but higher temperature cycling can prematurely degrade adsorbent performance. More recently several novel methods of heat input have been investigated which provide for rapid heat transfer and generation using activated

carbon cloths, Petkovska (1991), and adsorbent coated surfaces allowing high thermal conductivity exchange with a fluid phase for rapid heating and cooling. Similarly, coated adsorbent surfaces have been packaged as plates with endplate contact to thermoelectric devices for both heating and cooling (Bonnissel, 2001). These devices likely do not offer a significant enough capacity for high levels of separation. Therefore it would be valuable to consider the efficiency of conventional packed beds at the limit of cyclic thermal regeneration. Recently Bonjour et al. (2002) described an experimental study of an adsorption bed with an integral finned heat exchanger. The system was demonstrated for ethane nitrogen separation with steam regeneration because of the high heat transfer rate with condensation. The adsorption was conducted to the warm bed, but a long bed, 1 m, was used.

Ko et al. (2001) discussed a jacketed column design. The cooling step was aided by the use of coolant flow through the jacket of the vessel and the jacket was emptied during the heating step. They showed through simulation of a BTX separation that increased capacity could be obtained by use of the cooling jacket. A multiobjective optimization algorithm for a 2-step TSA system was described by Ko and Moon (2002a) and demonstrated for that same BTX problem. A Pareto curve was generated based on the amount of purge energy versus the amount adsorbed during the feed step. Ko, Moon and Choi (2002b) further analyzed the BTX problem to note that for long contact time the regeneration efficiency was nearly the same for changes in bed length or purge velocity.

It is of interest here to consider the performance of a thermal swing adsorption system of organics in the presence of humidity. This has not been extensively studied previously due to the difficulty of describing the equilibria effects. This important

industrial application may be studied more readily now by employing the equilibria adsorption models developed in this work. The feed to be purified, considered here, consists of high volatility vapor in the presence of various levels of humidity. Several adsorbents will be used to achieve the separation. Experimental data will be obtained over a range of conditions including coadsorption of water and organic component. Simulation results will be compared to experimental data in order to identify an optimum leading to rapid regeneration.

4.2 Fixed Bed Model

A numerical model for cyclic adsorption and thermal regeneration will be used to simulate thermal cycling, trace gas purification. The material and energy balance relationships are developed for a packed bed, multicomponent adsorption system. Multiple bed operation is simulated by using the product compositions from the feed bed as input to the purging bed. The adsorption column is assumed to be well insulated and adiabatic so that heat losses could be ignored. The heat input is implemented as a generic power source, which can be distributed throughout the bed length.

The mass and heat transfer resistances associated with packed beds include dispersion, film transfer and particle scale diffusivities. Accurate simulation of packed bed behavior can be is enhanced by knowledge of the contribution of each of these terms. A linear driving force resistance describes the solid phase mass transfer, while a film resistance describes the heat transfer.

The material balance in the fluid phase for each adsorbable component is given by

$$\varepsilon \frac{\partial Cy_i}{\partial t} + N_i = \frac{1}{Pe} \frac{\partial^2 Cy_i}{\partial z^2} - \varepsilon \frac{\partial v Cy_i}{\partial z} \tag{4.1}$$

where the rate of uptake to the particle can include mass transfer

$$N_i = \rho_b \frac{\partial n_i}{\partial t}_i \tag{4.2}$$

Particle scale mass transfer rates are expressed by linear driving force models

$$\frac{\partial n_i}{\partial t} = \frac{15 D_{ci}}{R_p^2} \left(n_i^* - n_i \right) \tag{4.3}$$

while the film resistance is written as

$$\rho_b \frac{\partial n_i}{\partial t} = k_{fi} a (c_i - c_i^*) \tag{4.4}$$

The overall phase energy balance can be written as follows with terms for fluid phase enthalpy, solid phase internal energy, axial conduction and convection.

$$\sum \varepsilon \frac{\partial (Cy_i h_{fi})}{\partial t} + N_h = \frac{1}{Pe_T} \frac{\partial^2 T}{\partial z^2} - \sum \varepsilon \frac{\partial (v Cy_i h_{fi})}{\partial z} \tag{4.5}$$

where the fluid phase enthalpy is

$$h_{fi} = C_{pfi} \left(T_f - T_{ref} \right) \tag{4.6}$$

and the heat transfer rate to the particle is

$$N_h = (1 - \varepsilon) h a \left(T_f - T_p \right) = \frac{\partial U_s}{\partial t} \rho_b \tag{4.7}$$

and the axial thermal Peclet number is vL/K_L. The internal energy of a particle includes terms for heat capacity of the adsorbent, heat of adsorption and adsorbed phase heat capacity.

$$U_s = C_{ps}(T_p - T_{ref}) + \sum [C_{pai} n_i)\left(T_p - T_{ref}\right) - \lambda_i n_i] \tag{4.8}$$

Dankwerts boundary conditions were imposed for the dispersion case. These equations are made dimensionless in terms of column volumes of feed by the introduction of the dimensionless time,

$$\tau = \frac{tL}{\mathrm{v}_o} \tag{4.9}$$

This set of coupled partial differential equations can be integrated by the method of lines. The model was written in order to solve both the axial dispersion and the plug flow case. The distance coordinate is discretized using a backward difference approach for plug flow, while a centered difference model was used for the dispersion case.

The mass transfer resistance, which is controlling for adsorption has been studied previously. Solid phase diffusion resistance is controlling at higher loadings while film transfer is significant at low gas phase concentrations. Axial dispersion effects are neglected in this analysis in order to avoid the computational overhead of the second partial derivatives. The intraparticle uptake rate with the film coefficient determined by the correlation of Wakao.

$$\frac{k_{fi} D_p}{D_{mi}} = 2.0 + 1.1 N_{\mathrm{Re}}{}^{0.6} N_{Sc\,i}{}^{1/3} \tag{4.10}$$

Particle diffusion is obtained from the correlation of Gilliland et al. (1974). All physical properties are taken as bulk properties.

A source term is included for the power input. The source term for heating can be evaluated for 2 cases. When a fixed power input is specified then the source term can be input directly into the overall energy balance eq. 3.7. When a fixed temperature input is

employed then a steady state heat balance can be written as follows to describe the heating density for a stage of the bed.

$$\frac{S}{\mathrm{v}_o A} = \frac{PC_p}{R}\frac{\Delta T}{T_{ref}} \tag{4.11}$$

in units of J/m^3 where the source term has been made dimensionless in time based on the feed velocity.

There can be inaccuracies introduced into a simulation by a weak understanding of the adsorption equilibria. This would be the case for multicomponent behavior of a non-ideal mixture such as organic and water coadsorption. Also there is not any multicomponent equilibria data at the desorption temperature; however, the water adsorption should be greatly reduced resulting in little multicomponent effect at the higher temperatures. The adsorption equilibria were described using the approach suggested in Chapter 2. Organic component adsorption was correlated to a Potential theory expression, water adsorption was described by either the distribution function for activated carbon or an additional potential plot for silica gel adsorption. Condensation in the voids of the bed could result due to roll up in the purge step. The condensation condition was included in the model by increasing the adsorption capacity to include the bed voidage for all relative pressures greater than 1.0, although a linear patch function was employed between 1.0 and 1.01 relative pressure in order to eliminate the discontinuity.

Implementing the multicomponent equilibria requires that the equilibrium concentration be evaluated at each point in space and time. This could be done through a root finding mechanism or by carrying the equilibrium as an integration variable. The former requires that a good guess be provided to initialize the solver while the latter

suffers from the loss of information associated with derivatives, which can lead to the calculation of negative concentrations. The second approach was employed in this work because the highly non-linear nature of the multicomponent equilibria did not suggest a stable basis to supply the good guess to the root solver. Therefore the following set of equations, forms a linear system which is solved for equilibria derivatives given that the actual fluid and solid concentration and temperature derivatives are evaluated from the material and energy balances

$$k_{fi}a\left(\frac{\partial c_i}{\partial t}-\frac{\partial c_i^*}{\partial t}\right)-\rho_b k_{pi}a\left(\frac{\partial n_i^*}{\partial t}-\frac{\partial n_i}{\partial t}\right)=0 \tag{4.12}$$

where eq. 4.12 is the differential of the rate equations

$$\frac{\partial n_i^*}{\partial t}-\frac{\partial n_i^*}{\partial c_1^*}\frac{\partial c_1^*}{\partial t}-\frac{\partial n_i^*}{\partial c_2^*}\frac{\partial c_2^*}{\partial t}-\frac{\partial n_i^*}{\partial T}\frac{\partial T}{\partial t}=0 \tag{4.13}$$

and eq. 4.13 is the differential of the equilibria.

In this study it is assumed that the time scale for pressurization is small compared to the overall cycle allowing this effect to be neglected. The solution was implemented using a set of routines written in Visual C++ with calls to the integration algorithm ODESSA, which employs LSODE, a Gear's type method for first order ODE's. Multiple bed systems could be integrated simultaneously by augmenting the model matrices to discretize additional columns.

In addition to the model equations eq. 3.1-3.7 the integrated mass balance was calculated for the three streams: feed, product and purge. For the cases of complete desorption of a single bed simulation or cyclic steady state of a multiple bed system, the difference between the integrated feed, and sum of product plus purge is zero. The

material balance for the model was calculated by integrating the concentration of each stream: feed, product and purge. The equation for the integrated mass of the stream is

$$\frac{dM_i}{dt} = \mathrm{v}Ac_i \tag{4.14}$$

4.3 Laboratory-Scale Experimental TSA System

4.3.1 Description

In order to investigate the behavior of a thermal cycling adsorber system a laboratory-scale apparatus was constructed. The features of this system needed to be consistent with the behavior of a scaled-up air purification apparatus. The system also would require sufficient instrumentation in order to quantify the appropriate conditions that would yield an optimized design. Among the appropriate factors that must be considered is adsorber design, the method for heat input, chemical concentration and humidity measurement, flow switching, and rapid temperature measurement. The selection of components and construction materials will allow for rapid thermal cycling while maintaining the high level of purification. The size of the system was chosen in order to be able to obtain adiabatic behavior in the adsorber column and evaluate conditions for rapid cycling. An apparatus to conduct single step and cyclic thermal adsorption studies was constructed. An experimental TSA air purification apparatus will be used to measure single bed and cyclic behavior.

4.3.2 Apparatus

Several earlier studies had used single bed results as a basis for multi-bed design. The single bed approach may not be able to capture all of the dynamics associated with

multicomponent separations. For instance the water adsorption wave will progress ahead of the contaminant wave and that water concentration would be important for the purge behavior of a regenerating bed. The laboratory system therefore was designed to operate in either a single bed or 2-bed mode.

The 2-bed thermal regeneration adsorption system is shown schematically in Figure 4.1. A mass flow controller meters the feed flow. Either low or high volatility vapor feed streams can be generated with variable humidity levels. Humidification was performed by injecting liquid water into a chamber containing a cartridge heater maintained at 388 K. Temperature control to the adsorber was achieved by passing the feed flow through a heat exchanger immersed in the thermostatic bath. The feed chemical contaminant can be introduced as either a vapor or a liquid. In the case of a vapor, a thermostatic box (318 K for chloroethane) contained a cylinder of the pure component feed chemical. A valve was used to meter the vaporized chemical and the flow rate was recorded using an electronic flow meter. When the contaminant chemical is a liquid the metering pump is used to deliver the flow to a heated valve. The liquid feed chemical could either be injected or recycled to the liquid chemical reservoir. The chemical feed line is heat traced and operated at 333 K.

Three modes of operation are employed for the system: bypass, breakthrough and cyclic. In the system bypass mode the feed flow is allowed to bypass the 2-bed adsorber system, which is useful in performing calibration. In a breakthrough mode the feed is directed to one bed and purge flow to the opposite bed blocked by a shutoff valve. Feed enters the column by up-flow in order to minimize the effect of condensation in the purge

step. Flow is directed to either of the adsorption beds using three-way slide valves (Versa Inc.). Product flow is withdrawn by a vacuum pump metered through a mass flow

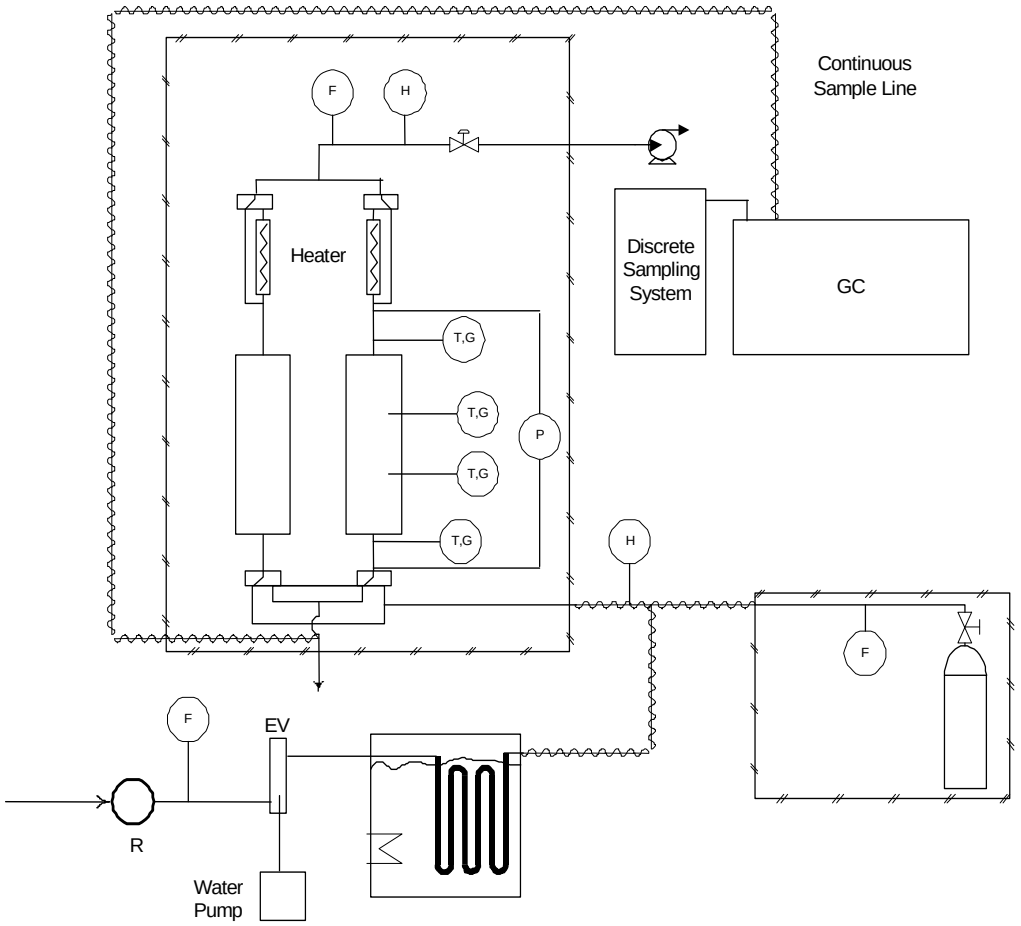

Figure 4.1 Schematic of experimental TSA system. R, pressure regulator; F, flow meter; P, pressure transducer; T, thermocouple; G, gas sampling port; GC, gas chromatograph; H, humidity analyzer; EV, water evaporator. Dashed lines indicate continuous gas sample.

controller. The purge flow temperature is controlled using an inline resistance heater where power input is monitored using a current shunt. Process variable measurement and cycle control is achieved using microcomputer control algorithm programmed in Labview (National Instruments Inc.).

The heaters located above each column are 1/2 inch diameter tubes with internal ceramic coated wires (Hotwatt Inc.) rated for 400 W at 120 V. A 4 inch length of tubing separates the heater from the column inlet. The product endcap has a Teflon connection to the tubing in order to reduce heat capacity. Both the tubing and the heater are wrapped with glass wool insulation. Temperature control of the feed flow to the adsorber was achieved by passing the feed flow through a heat exchanger immersed in the thermostatted bath. Upstream of the heat exchanger, humidification is performed by injecting liquid water. A cartridge heater placed in the air stream evaporated the water. The voltage to the heater is regulated through a variable transformer in order to deliver a fixed temperature purge to the purge bed. The pressure drop across the bed was monitored using a differential pressure cell. In order to minimize the pressure drop through the bed, fittings and connections are ½ inch.

Voltage to the heater was manually adjusted using a variable transformer, while the power is monitored. A latching high temperature cutout switch was installed to prevent ignition of the adsorbent. A bypass valve was added to the product flow in order to deliver cool purge gas at the end of the heating step. This was accomplished by 3-way slide valves identical to those on the feed end.

The column was fabricated using thin walled carbon steel, which was treated with a chromate finish and having dimensions listed in Table 4.1. The adsorption beds are made

Table 4.1 Dimensions and probe positions in adsorbent column

	Short Column	Long Column
Column length (cm)	11.5	17.5
Column diameter (cm)	7.6	7.6
Feed endcap height (cm)	3.7	3.7
Position 1 distance from feed endcap (cm)	2.0	2.0
Position 2 distance from feed endcap (cm)	4.5	4.5
Position 3 distance from feed endcap (cm)		7.0
Position 4 distance from feed endcap (cm)		9.5
Product endcap height (cm)	1.5	1.5
Total adsorbent length (cm)	6.0	12.0

of 7.6 cm inner diameter, thin wall, 0.2 mm, copper tube fitted with PEAK endcaps. The outside of the bed is wrapped in glass wool batting and Mylar. Columns of various lengths were constructed both with and without in-bed thermocouple and concentration probes. The adsorption column was constructed from an open cylinder which was fitted with endcaps where the endcaps were retained using an external brace. The cylindrical sleeve was fabricated from either copper or carbon steel. A length of pipe with a nominal 3 inch OD was machined to provide a thin walled cylinder. The wall thickness of this bed was 16/1000 inch with an inner diameter of 2.97 inch. The metal surface was treated to prevent corrosion. One column was fitted with a combination of gas sampling and temperature ports. The temperature probe, Type T thermocouple, has a 1/16 inch diameter sheath. The gas sampling was accomplished using 1/16 inch stainless steel tubing. Both the thermocouple and sampling tube were passed through a hole in the cylinder wall and butt fitted into a sintered metal cylinder 1 cm in length. The butt end connections and the probe-to-wall contacts were fixed with epoxy. Two cylinder sets were constructed with 17 and 11 cm overall lengths which allowed a packed adsorbent length of 12 and 6 cm respectively. The mass of each cylinder was 76 g and 53 g. Endcaps were fabricated for the column using PEAK, an inert high-temperature thermoplastic. At the feed end a screen-plate, which was retained by springs, is connected to the feed endcap. At the product end the screen was built into the endcap with an open diameter of 2.8 inches. An O-ring around the endcaps is used to make a seal with the cylinder. Each endcap is press-fit into the column. The probes are located at 2 cm distances starting from the feed end. The adsorption beds are made of 7.6 cm inner

diameter, thin wall, 0.2 mm, copper tube fitted with PEAK endcaps. The outside of the bed is wrapped in glass wool and Mylar.

The heat transfer coefficient of the bed and lumped heat capacity can be calculated using equilibrium theory solutions to the energy balance equation. A constant temperature input at a fixed velocity results in a temperature profile. The difference in temperature from inlet to outlet is related the heat transfer coefficient while the speed of the wave is a function of the heat capacity. The overall heat transfer is 2 J/m^2s suggesting near adiabatic behavior, and the heat capacity is 960 J/kgK.

4.3.3 Analytical

The system was leak tested by applying an over pressure. Chemical concentrations were measured using a gas chromatograph equipped with a flame ionization detector. Sampling was conducted using two methods. Discrete samples were collected at up to six locations simultaneously. A series of gas sampling loops controlled by electric actuators were connected through switching valves to allow sequential injection from each loop. Solenoid valves between the sample loop and the process flow allow the flow from the process to be depressurized to atmospheric pressure after filling yielding a common reference state for concentration determination. The FID detector exhibits a linear calibration over the concentration range considered. When the feed, product and purge concentration ports are selected then up to three in-bed ports can also be sampled. Each filled loop is injected in the chromatograph column flow after the chromatogram of the previous sample has been recorded. In addition to discrete sampling a second FID detector is used to record a continuous chemical concentration. The flowrate to the detector is fixed using a metering valve and the sample passes to the detector through a

heated transfer line at 333 K. This air flow is combined with the combustion gases to maintain a stable flame. The continuous concentration measurement is used to monitor the purge stream. The flowrate through the continuous FID detector is measured before and after each run. When a single bed breakthrough experiment is performed the purge sample port is capable of monitoring the breakthrough and the purge profiles. A background contaminant in the ambient air was detected using the FID. This concentration corresponds to approximately 20 ppm. The retention time of the feed chemical was adjusted to avoid overlap between these peaks.

The humidity was measured using chilled mirror hygrometers (EGG 911) on the feed and product streams. A sample flow of 1 slpm is required for the sensor. The time constant for the hygrometers is approximately 1 minute. A flow balance is verified by measuring the flowrates with a dry test meter. The chemical feed rate is determined from the chemical supply mass flow meter and dry air feed rate.

4.4 Results

4.4.1 Overview

A series of experimental runs were performed using the laboratory scale thermal regeneration apparatus. The effect of various operating and system parameters was investigated in an attempt to identify conditions for rapid regeneration and retention of contaminant vapors. The runs were of two types: single bed feed followed by purge or cyclic two-bed operation. Breakthrough experiments are used to identify the bed capacity and the regeneration time. A series of experiments were performed for both dry and humid feed, followed by thermal purge. The feed components considered were water vapor, and a moderate volatility vapor and a low volatility vapor. Adsorbents were sought

for minimal water coadsorption of high volatility vapors and rapid regeneration of low volatility vapors. The effects of fluid velocity, purge temperature, and cycle time on the purification process were examined for this system to determine design rules that could be used to analyze more complex cycles.

4.5 Dry and Humid Runs Without Chemical Contaminant

To identify conditions required for rapid thermal regeneration of an adsorption column the progress of a thermal wave was first analyzed without introducing the chemical contaminant. Starting with a clean bed at ambient temperature a constant temperature input step change was introduced at the product end of the bed where the purge halfcycle could be no longer than the adsorption halfcycle for a two-step cyclic process. Increased adsorption capacity during the feed step can be achieved by including a cooling step in the purge halfcycle. Chasing the heated purge wave with ambient temperature purge reduces the temperature at the product end. In these experiments the feed end temperature probe was monitored until the temperature furthest into the bed recorded a temperature equivalent to the average of feed and heated purge inlet temperatures. At the time when this temperature reached the furthest probe the heat input was terminated and a cooling step was initiated. The cooling step was terminated when the furthest temperature probe at the feed end was less than 5 K greater than the feed temperature.

The feed superficial velocity was considered in a range of 30-40 cm/s, which is in the range of the fluidization velocity. The purge to feed mass flow ratio was considered over a range from 0.1 to 0.5. The bed dynamics of the thermal front of a heated air purge were recorded for many experiments with the conditions for several of these are listed in Table 4.2.

Figure 4.2 illustrates the in-bed temperature profiles for a constant purge temperature experiment, Run 1 Table 4.2, of a 12.7 cm column packed with BPL carbon. The product end temperature front is sharp upon powering the heater, indicating good heat transfer between the heating element and air. The temperature profile demonstrates a 14 K temperature difference at steady state between the purge inlet temperature and the feed end temperature at the end of the heating portion of the purge step. This is a result of heat losses primarily through the endcaps. The time for the midpoint temperature during the purge step to reach the 2 cm probe is taken as the minimum half cycle time if the feed step would then be initiated to a warm bed. In this case it occurred at 9 minutes. The slope of the temperature profile is not as steep for positions further into the bed as the heater has already been turned off by the time the temperature front reaches those probes. During the cooling step the temperature exhibits a gradual decrease at the product end associated with the thermal heat capacity of the heating element. The purge air continues to be warmed as it passes through the heater.

Figure 4.3 presents temperature profiles recorded for Run 2 conducted with the heater bypass installed. In this case more rapid cooling is noted. A shorter bed depth is also employed in this experiment 6.1 cm versus 12.7 cm for the run without heater bypass. The time from the end of the heating step to the end of the cooling step is reduced from 20 to 4 minutes while the purge velocity increases from 10 to 14 cm/s going from Run 1 conditions to Run 2 conditions. This illustrates the need to limit the heat capacity associated with the column.

Table 4.2 TSA Run Conditions

	Run 1	Run 2	Run 3	Run 4	Run 5
Adsorbent	BPL	PICA 1322	BPL	Ambersorb 563	Ambersorb 563
Chemical Contaminant	---	---	---	chloroethane	chloroethane
y_{feed}	---	---	---	$8.9x10^{-4}$	$9.2x10^{-4}$
Feed Dewpoint (K)	<258	<258	289.1	<258	<258
Bed diameter (cm)	7.5	7.5	7.5	7.5	7.5
Bed depth (cm)	12.7	6.1	12.7	6.1	6.1
Feed Velocity (cm/s)	32.7	37.2	32.5	37.5	34.9
Purge Velocity (cm/s)	10.1	16.1	15.4	20.5	15.3
Feed Temperature (K)	298	298	298	298	298
Feed Pressure (kPa)	136	120	135	130	140
Feed Pressure Drop (kPa)	18	7	18	8	18
Particle Diameter (mm)	1.0	1.0	1.0	0.5	0.5
Bed Density (kg/m^3)	480	480	480	530	530
Purge Temperature (K)	333	353	358	373	353
Feed Time (m)	32	7.4	44	---	9.5
Heat Time (m)	9.0	2.2	22	---	2.5
Cool Time (m)	23.0	5.2	22	---	7.0
τ_{ads}	4943	2707	6756	---	3261
τ_{heat}	1390	805	3378	---	858
τ_{cool}	3553	1902	3378	---	2403
τ_{heat}/τ_{ads}	0.28	.297	0.5	---	0.26
Purity (mg/m^3)	---	---	---		< 4
Energy/Product (J/mol)	108	330	934	2101	300

Table 4.2 TSA Run Conditions (cont.)

	Run 6	Run 7	Run 8	Run 9	Run 10
Adsorbent	Ambersorb	PICA 1322	PICA 1322	PICA 1322	PICA 1322
Chemical Contaminant	chloroethane	chloroethane	chloroethane	chloroethane	chloroethane
y_{feed}	$8.5x10^{-4}$	$9.2x10^{-4}$	$9.2x10^{-4}$	$9.6x10^{-4}$	$9.2x10^{-4}$
Feed Dewpoint (K)	291.5	291.7	283	<258	<258
Bed diameter (cm)	7.5	7.5	7.5	7.5	7.5
Bed depth (cm)	6.1	6.1	6.1	6.1	6.1
Feed Velocity (cm/s)	37.2	37.4	37.4	37.4	37.4
Purge Velocity (cm/s)	15.3	16.1	16.1	16.3	15.5
Feed Temperature (K)	298	298	298	289	289
Feed Pressure (kPa)	130	130	130	130	130
Feed Pressure Drop (kPa)	8	7	7	7	7
Particle Diameter (mm)	0.5	1.0	1.0	1.0	1.0
Bed Density (kg/m^3)	530	480	480	480	480
Purge Temperature (K)_	353	353	353	353	353
Feed Time (m)	14.6	21	23	20	9
Heat Time (m)	6.3	8.4	8.4	2.0	3.1
Cool Time (m)	8.3	12.6	14.6	18	5.9
τ_{ads}	5346	7725	4760	7357	3311
τ_{heat}	2305	3090	3075	735	1140
τ_{cool}	3037	4614	4614	6622	2170
τ_{heat}/τ_{ads}	0.56	0.4	0.4	0.10	0.34
Purity (mg/m^3)	17	43	43	32	<4
Energy/Product (J/mol)	508	437	549	135	346

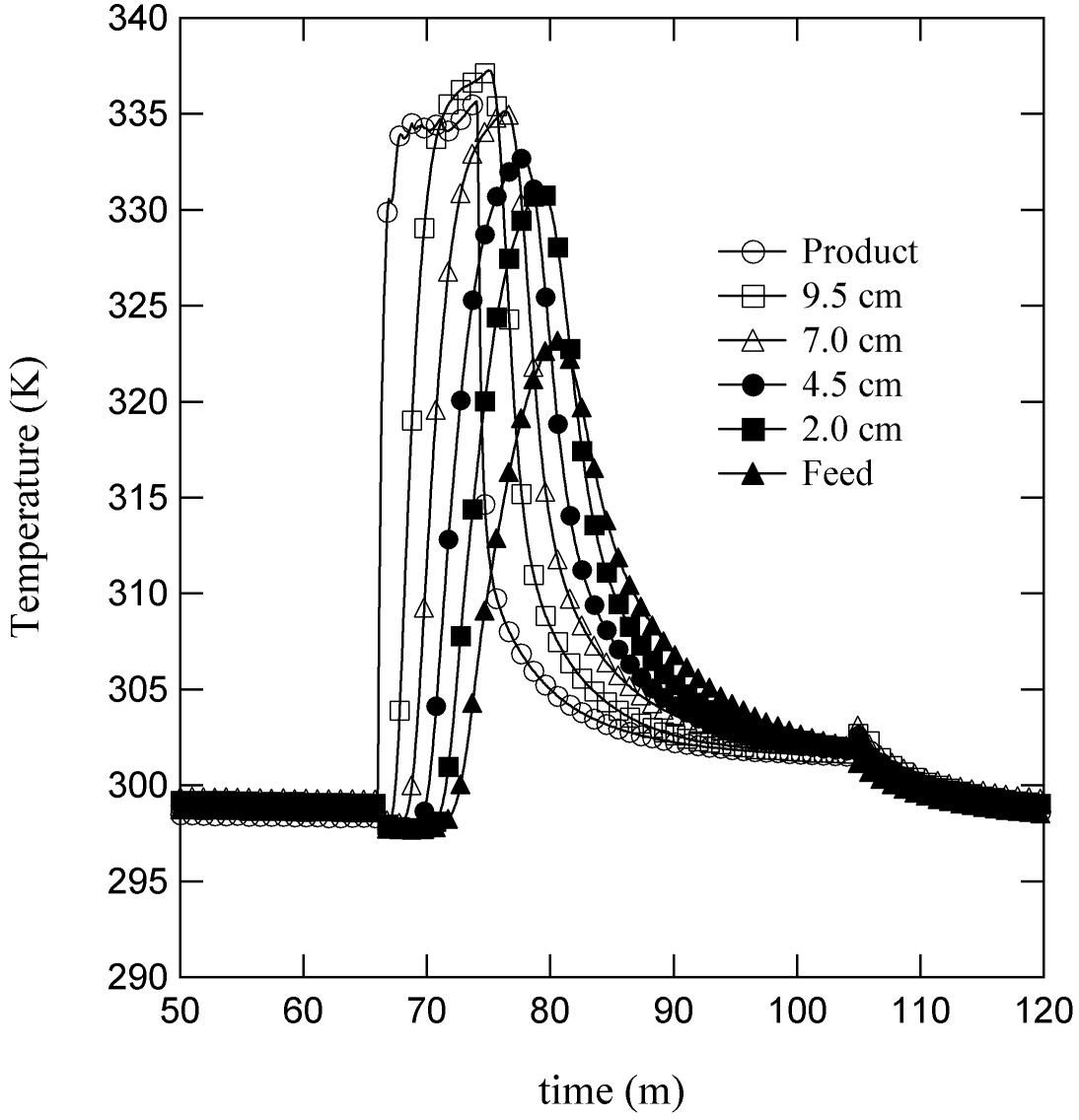

Figure 4.2 Temperature profiles for thermal purge followed by cooling using the conditions listed in Table 4.2 Run 1.

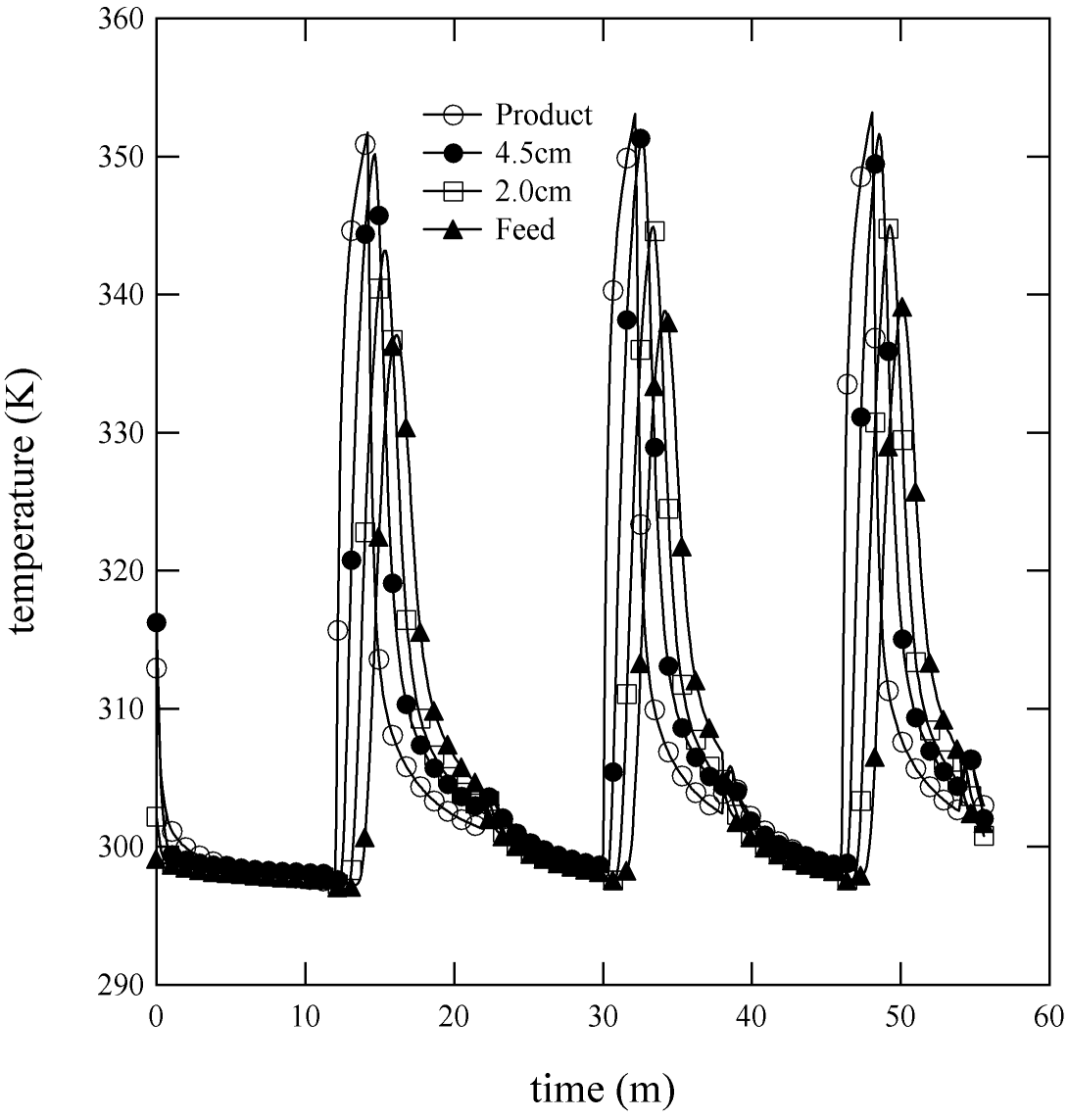

Figure 4.3 Temperature profiles for thermal purge followed by cooling using the conditions listed in Table 4.2 Run 2.

Figure 4.4 provides a summary of the effect of temperature on the purge time for both BPL carbon and Ambersorb 563. The time is reported in terms of the dimensionless parameter τ_{heat}. It is seen that there is no significant effect of temperature on τ_{heat}. This results from the adiabatic behavior of the column. For both adsorbents the average value of τ_{heat} is 450. Similar results are presented in Figure 4.5 for the effect of velocity on heating time. This indicates that thermal dispersion effects are not significant.

Results for a heated purge experiment using humid air are also considered. Here the feed water concentration is maintained constant during the experiment; however, the humidity of the purge inlet stream is reduced due to the elevated purge temperature. In the present study the water wave is allowed to pass through the feed bed to the purge bed. This is only important during the cooling step, as the water vapor has minimal adsorption capacity at the elevated temperatures of the heating portion of the purge step.

The feed and product water concentration measurements for the breakthrough and thermal purge of a humid air feed to a bed packed with BPL carbon are presented in Figure 4.6 together with the simulation results for nine cycles. Model parameters are listed in Table 4.3. The conditions of this experiment are listed as Run 3 in Table 4.2. Excellent agreement is observed in the simulation profile for the product water concentration. During this experiment the purge water concentration was not measured but the simulation result is presented. The loading profiles from the simulation indicate that the bed water

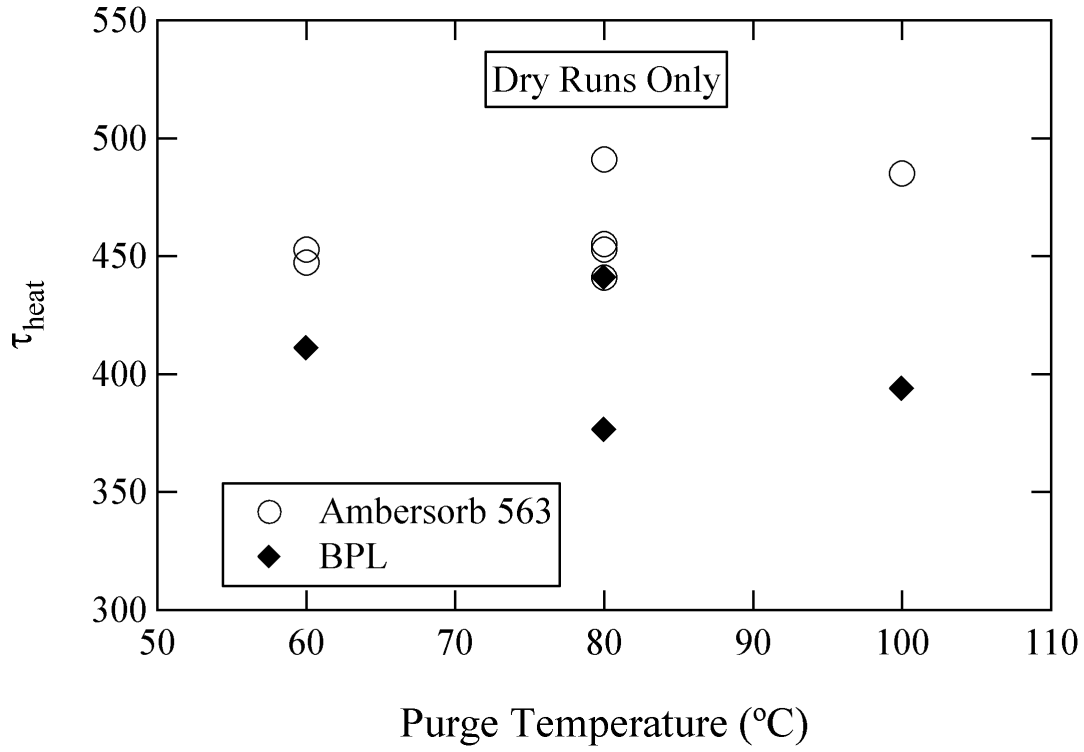

Figure 4.4 Dimensionless heating time versus purge temperature for dry runs.

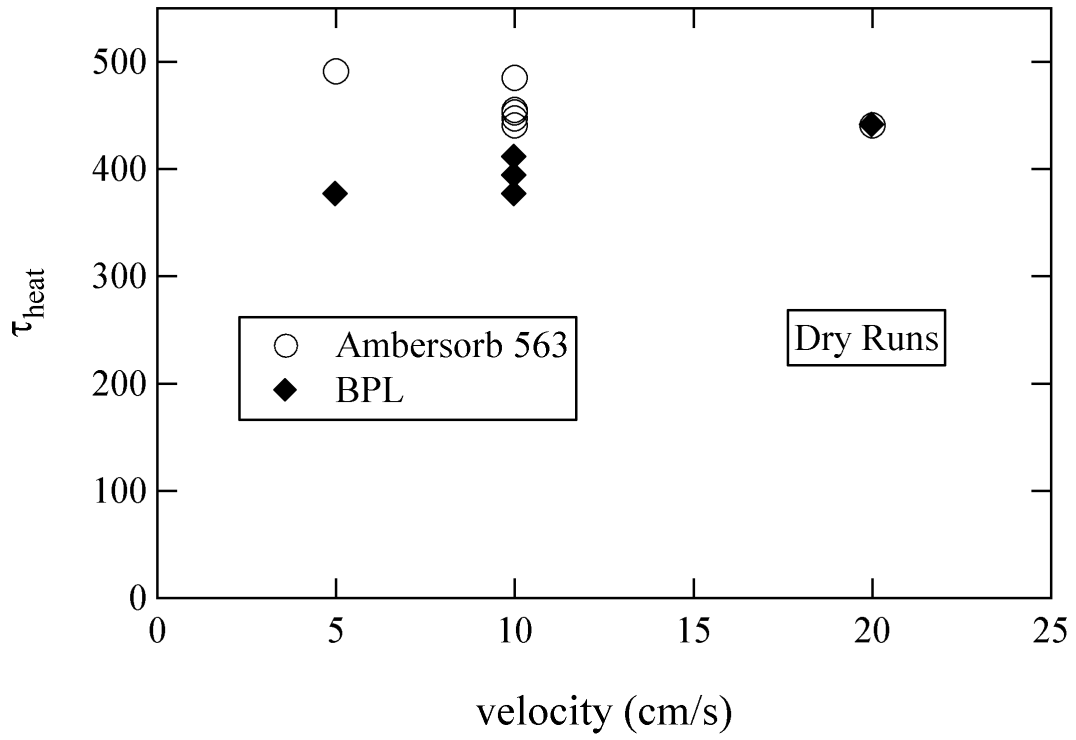

Figure 4.5 Dimensionless heating time versus purge velocity for clean bed.

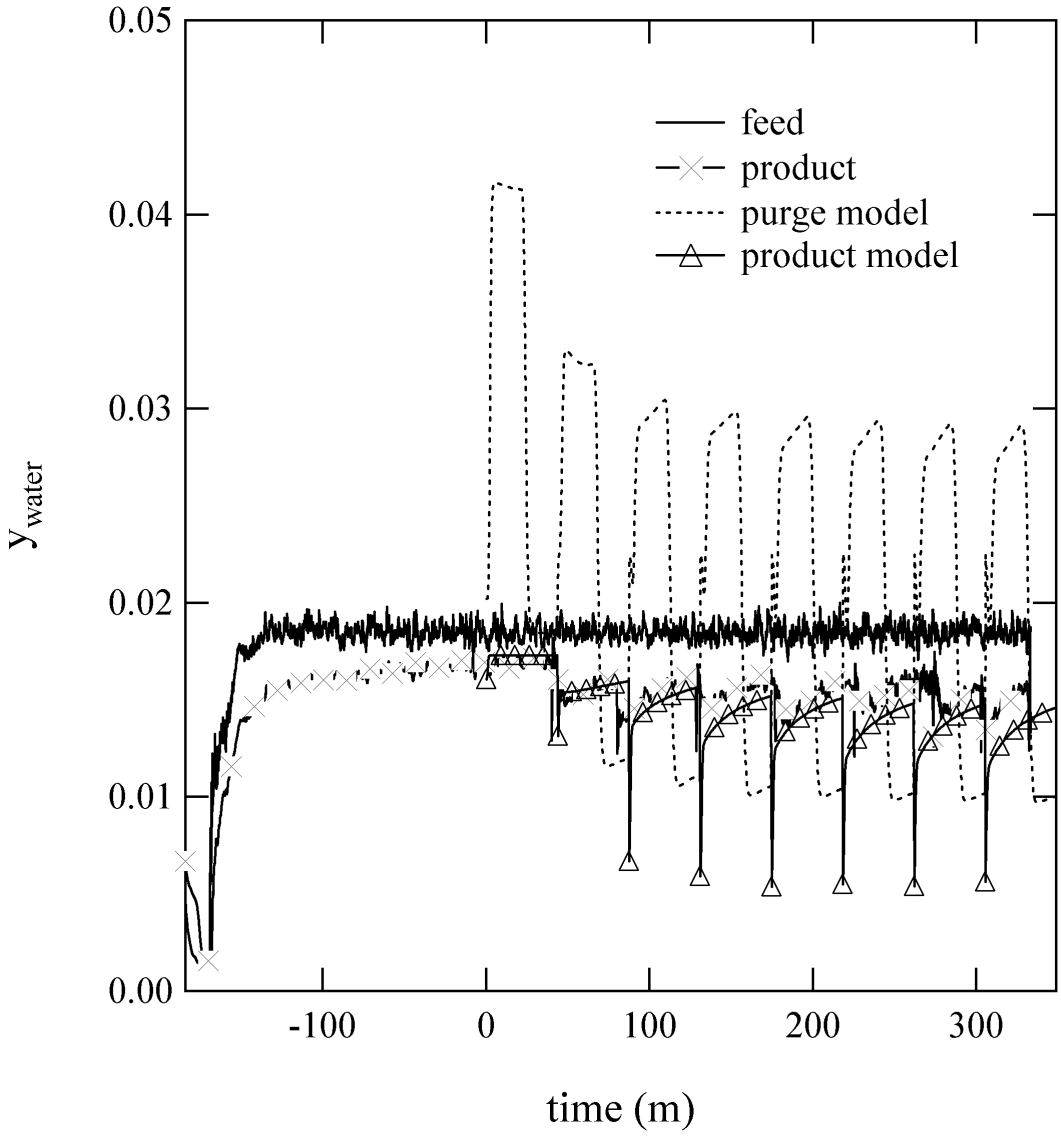

Figure 4.6 Water concentration profiles for constant humidity feed with cyclic thermal purge followed by cooling using the conditions listed in Table 4.2 Run 3.

Table 4.3.Model parameters for TSA simulation

No. Stages	20	
Cp air (J/mol/K)	29.1	
Cp CE (J/mol/K)	93.6	
Cp water (J/mol/K)	76.0	
	BPL/PICA	Ambersorb 563
d_p (cm)	0.1 (12/30 mesh)	0.05 (20x50 mesh)
kva (1/s)	10	42
kpa CE (1/s)	0.01	0.03
kpa Water (1/s)	$1x10^{-3}$	$1x10^{-3}$
ha (J/m3/K)	$6.8x10^{6}$	$2.6x10^{7}$
C_s (J/kg/K)	1250	1250
Pe	100	100
Pe_T	0.1	0.1
K_L (W/m/K)	0.03	0.03
ε bed voidage	0.43	0.47
ε_p particle porosity	0.60	0.52

loading is removed from the product end of the bed. The product water concentration is reduced by 25% versus the feed concentration. This represents a large loading difference because the steepest portion of the water isotherm occurs in this range.

A series of experiments were conducted to calculate the heating and cooling time for beds equilibrated over a range of relative humidity. The adsorption column was fed with humid air until the product dewpoint measurement matched the inlet dewpoint. The same procedures to determine the heating and cooling time for a dry bed were used with the humidified bed. The purge profile, for a bed initially saturated at humidity, is delayed versus a dry bed for the same purge flowrate and temperature conditions. Figure 4.7 presents the experimental results obtained for τ as a function of the relative humidity for both BPL and Ambersorb 563. A 500% and 300% increase in heating time is observed at 80% relative humidity with BPL and Ambersorb 563 respectively compared to the value recorded under dry conditions.

4.5.1 Dry and Humid Runs With Chemical Contaminant

The first part of this study provided insight into (1) the conditions required to process heated purges and (2) the propagation of the resulting temperature profiles. In order to understand the operation of a regenerative filtration system for chemical contaminant removal the effect of adsorbate loading on regeneration and the filtration capability are considered. To approach an optimum operating point relative to adsorbent utilization the component to be separated should

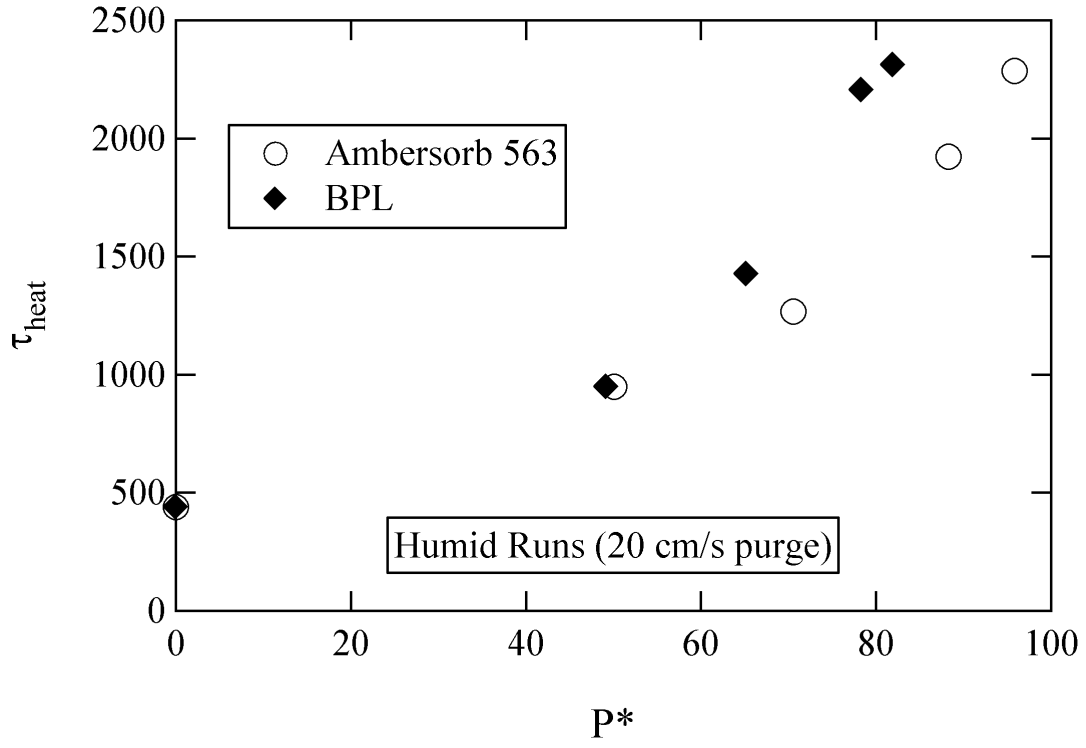

Figure 4.7 Dimensionless heating time versus relative humidity for BPL and Ambersorb 563 thermal cycling experiments.

progress far into the adsorption bed otherwise energy would be wasted during regeneration with the heating of clean adsorbent.

A series of experiments were performed in order to evaluate the adsorption and thermal purge of a high volatility vapor on activated carbon. A constant chemical feed concentration was delivered for a fixed period, which could have been either prior to breakthrough, to some intermediate concentration or to saturation at the product end of bed. In-bed concentration probes in addition to the feed, product and purge were sampled discretely. In addition a continuous concentration measurement of the purge was obtained for a number of experiments.

Breakthrough curves obtained on BPL carbon and Ambersorb 563 are shown in Figure 4.8 plotted as reduced product concentration versus stoichiometric time. The results were obtained at the same feed velocity and indicate that while the particle size of the Ambersorb is smaller the mass transfer is similar to that of BPL.

Several experiments were conducted with the feed step stopped well short of breakthrough. Later experiments were conducted to achieve breakthrough of the contaminant at the product end of the bed and to establish the adsorption time. Figure 4.9 presents chloroethane elution curves measured on the experimental system for a feed and purge run. The sequential and continuous measurements of feed concentration are in good agreement for the challenge. A constant concentration of 0.031 mol/m^3 results in breakthrough to the product under the conditions listed in Table 4.2 Run 4 using the adsorbent Ambersorb 563. The

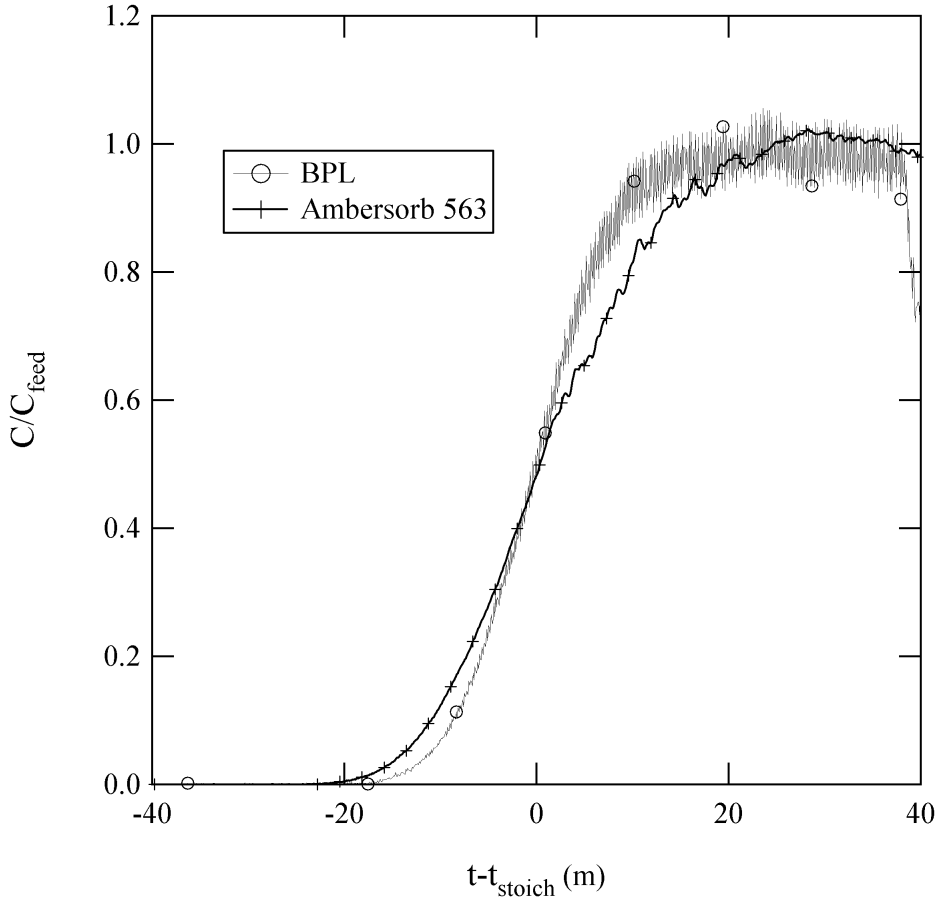

Figure 4.8 Breakthrough curves of chloroethane on two adsorbents.

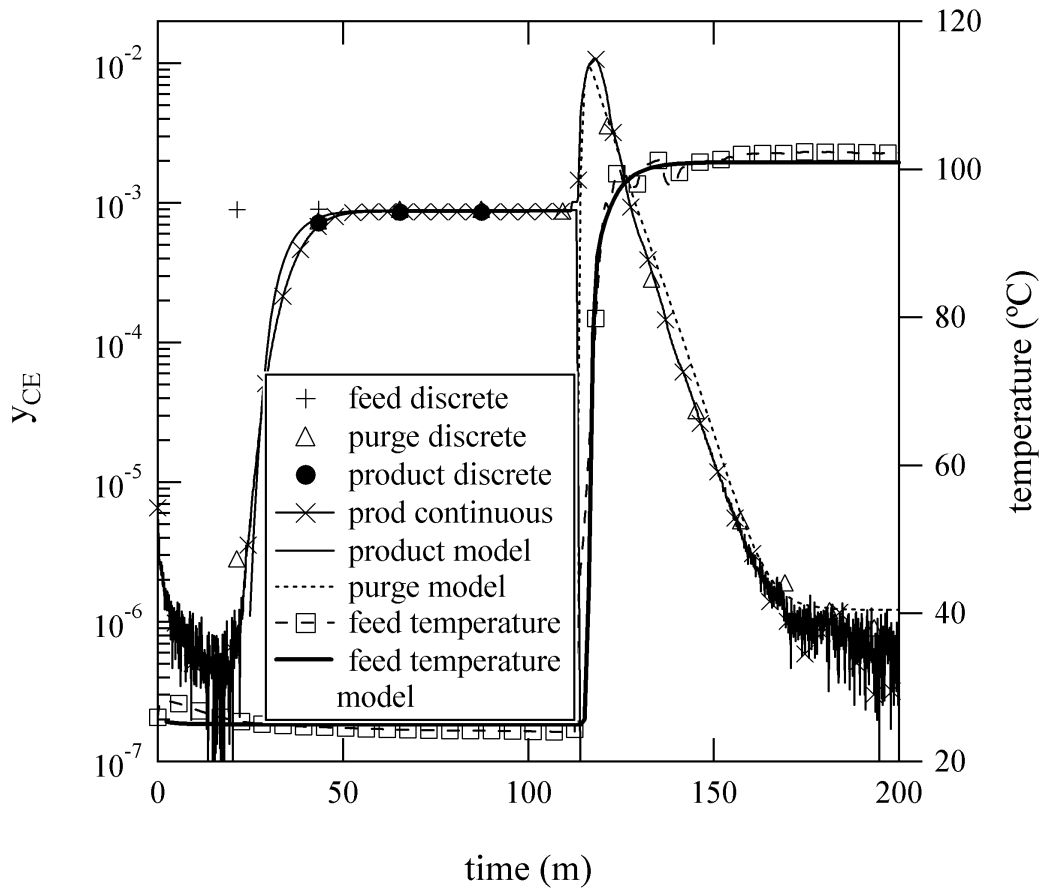

Figure 4.9 Feed and purge concentration profiles for chloroethane feed to dry bed of Ambersorb 563 Table 4.2 Run 4. Also shown are the simulation results.

concentration is displayed on a logarithm scale. Significant rollup above the feed concentration is observed in the purge profile. The temperature profile recorded at the 2 cm probe coincides with the appearance of the purge concentration. Also shown are the simulation results for the predicted breakthrough profiles. Excellent agreement can be seen in both the matching of the centers of the adsorption wave and shape of the curve at these dry conditions. A material balance can be calculated for these conditions based on the difference between the integrated feed and the sum of the product and purge. In this case the material balance is closed to within 2%.

Based on the results of the feed and purge experiments a series of cyclic thermal swing runs were conducted. Effective thermal cycling would require that the adsorption time be less than or equal to the purge time for two bed operation and that the concentration delivered to the bed be removed in the subsequent purge step.

A finite duration, 30 minute, chemical challenge was introduced using the conditions of Run 5. No change in concentration is recorded in the product, however a slight increase is noted for the 2 cm in-bed probe. The purge concentration is measured using both continuous and discrete samples, which agree well. The feed concentration is also monitored by discrete samples yet only one sample is taken during the injection period. The purge profile obtained from a chemical challenge experiment in shown in Figure 4.10. Simulation results are presented for the purge concentration. The initial purge concentration recorded by the detector exhibits noise. At higher concentrations the noise recorded from the

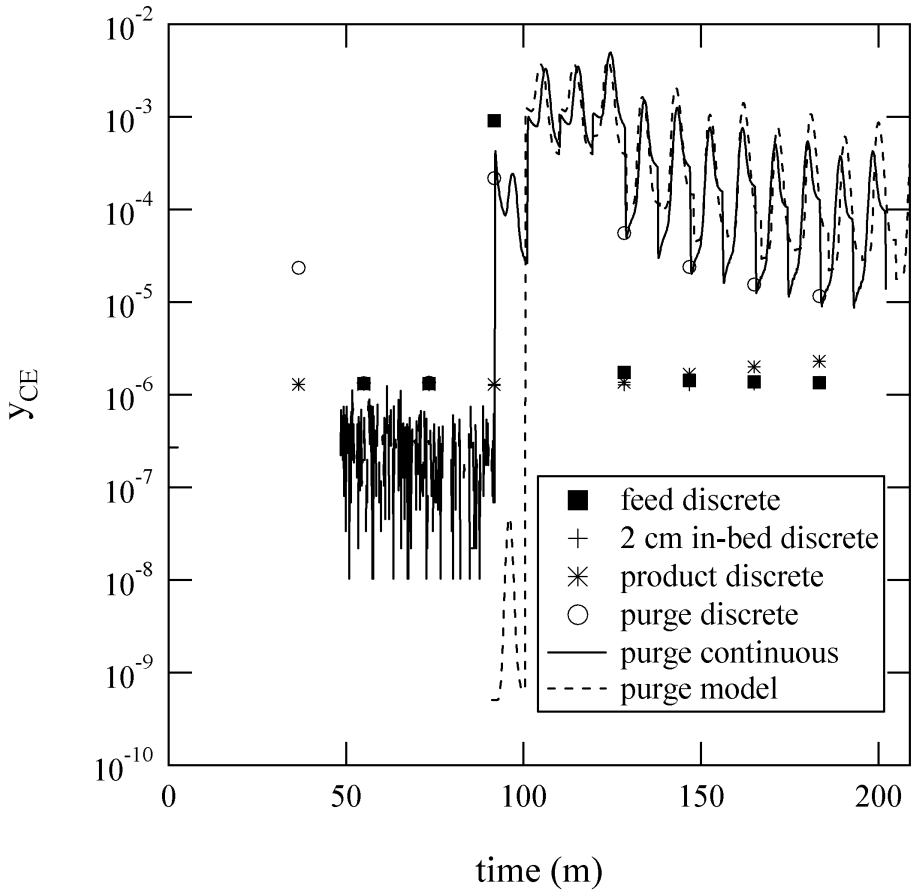

Figure 4.10 Concentration profile for pulse challenge with cyclic thermal purge for dry conditions listed in Table 4.2 Run 5, together with the simulation results purge. The product concentration exhibits carry-over.

FID detector is not apparent. Again excellent agreement is obtained between the simulation and the data for six cycles. This experiment was not continued until complete cleanup.

In the presence of humidity the energy required for regeneration would increase and the adsorption capacity would decrease relative to the dry case. This can be seen in the energy parameter listed in Table 4.2. Several experiments were conducted to assess this impact and the model accuracy. Figure 4.11 and Figure 4.12 present the purge and product profiles recorded using conditions of Run 6 in Table 4.2. The simulation for coadsorption of chloroethane and water consisted of non-interacting adsorption equilibria. The multicomponent equilibria for chloroethane and water were based on the relative differential heat method equation 3.12. The purge results obtained using the continuous FID detector show a larger swing than the simulation result. The simulation does seem to agree very well with discrete sampling results. The results of a simulation for the case of complete purge were shown to yield a closure of the material balance. The purge concentration decreases by almost an order of magnitude after the first three halfcycles, and then continues to decrease slowly for many cycles, never completely cleaning. The product concentration is predicted to be greater than that observed with the discrete sampling. However the product concentration in both cases is approximately 1% of the feed concentration. The number of CPU cycles required to perform the result. The simulation does seem to agree very well with discrete sampling results. The results of a simulation for the case of complete purge were shown to yield a closure of the material balance. The purge

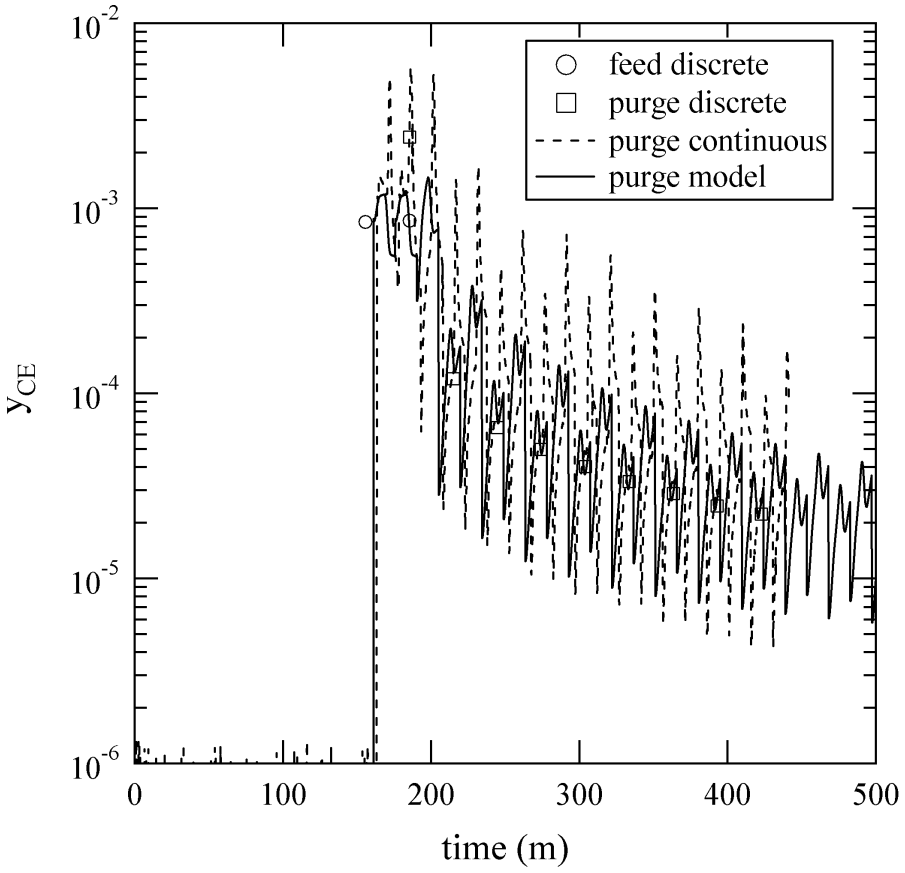

Figure 4.11 Purge profiles for chloroethane feed to Ambersorb 563 with humid cycling at conditions of Table 4.2 Run 6. Also shown in the purge simulation profile.

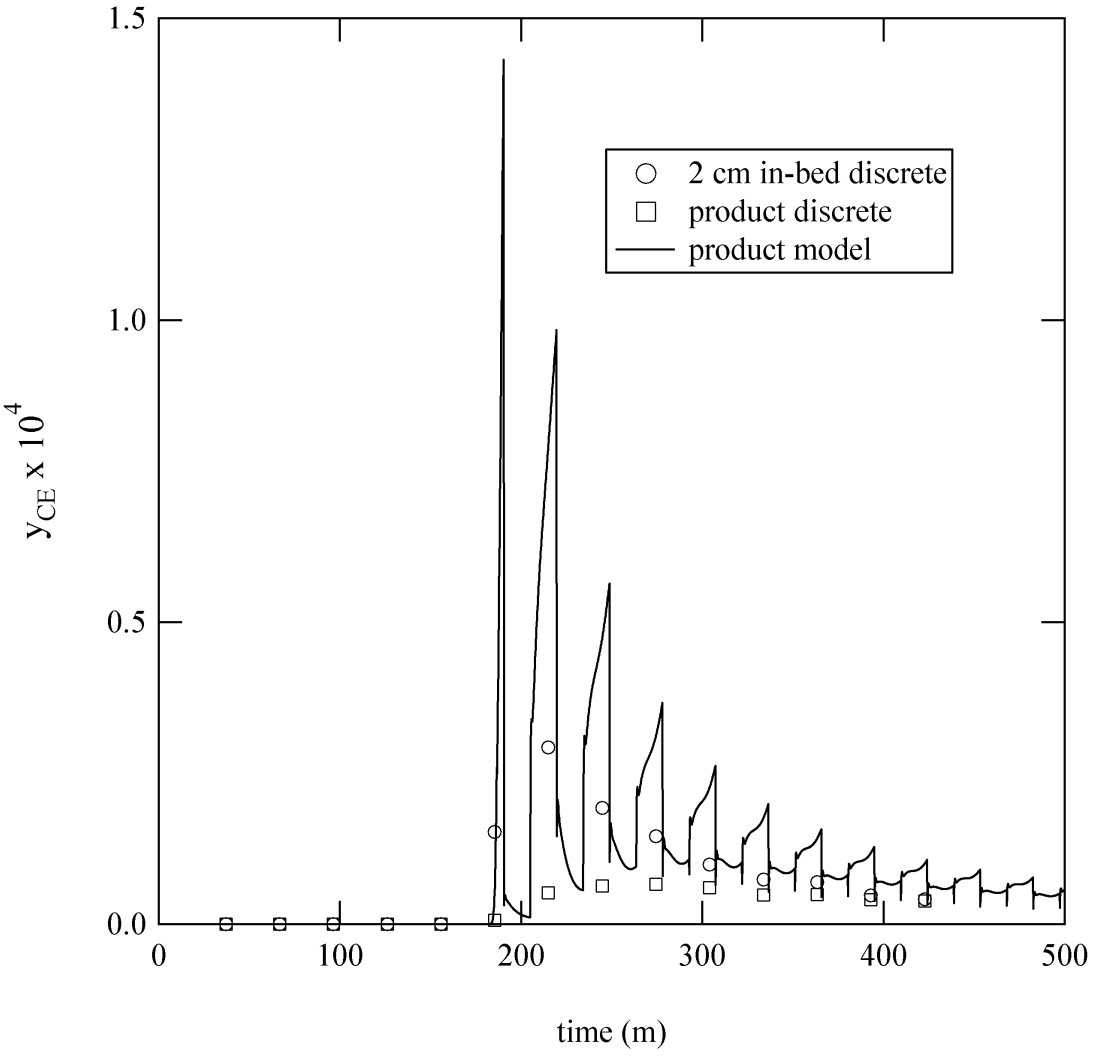

Figure 4.12 Product concentration profiles for chloroethane feed to Ambersorb 563 with humid cycling with conditions of Table 4.2 Run 6. Also shown is the product simulation profile.

concentration decreases by almost an order of magnitude after the first three halfcycles, and then continues to decrease slowly for many cycles, never completely cleaning. The product concentration is predicted to be greater than that observed with the discrete sampling. However the product concentration in both cases is approximately 1% of the feed concentration. The number of CPU cycles required to perform the multicomponent simulation with interacting beds increases greatly compared to the case of a feed and purge simulation.

A second experiment with a chloroethane challenge and humidity was conducted using the conditions listed as Run 7 in Table 4.2. In this case the adsorbent was PICA 1322 with properties similar to BPL carbon. The purge water profile is shown in Figure 4.13 where good agreement between the model and the data is obtained. The purge chloroethane profiles, Figure 4.14, also show excellent agreement. The product profile, Figure 4.15, under these conditions exhibits a high concentration breakthrough up to the feed concentration, while the model predicts breakthrough to a concentration slightly less than the feed concentration. The product concentration does not clean up to below 1% of the feed concentration until after 10 cycles. While the feed conditions for Runs 6 and 7 are nearly identical the breakthrough of feed to the product is nearly complete for PICA carbon because the halfcycle time is longer than for Ambersorb 563 due to greater water adsorption. For the 2-bed 3-step cycle (feed, heated purge, and purge without heating) experiments, breakthrough of feed contaminant to the product recorded as product purity is listed in Table 4.2. Even under dry conditions, Run 5, there is observed breakthrough

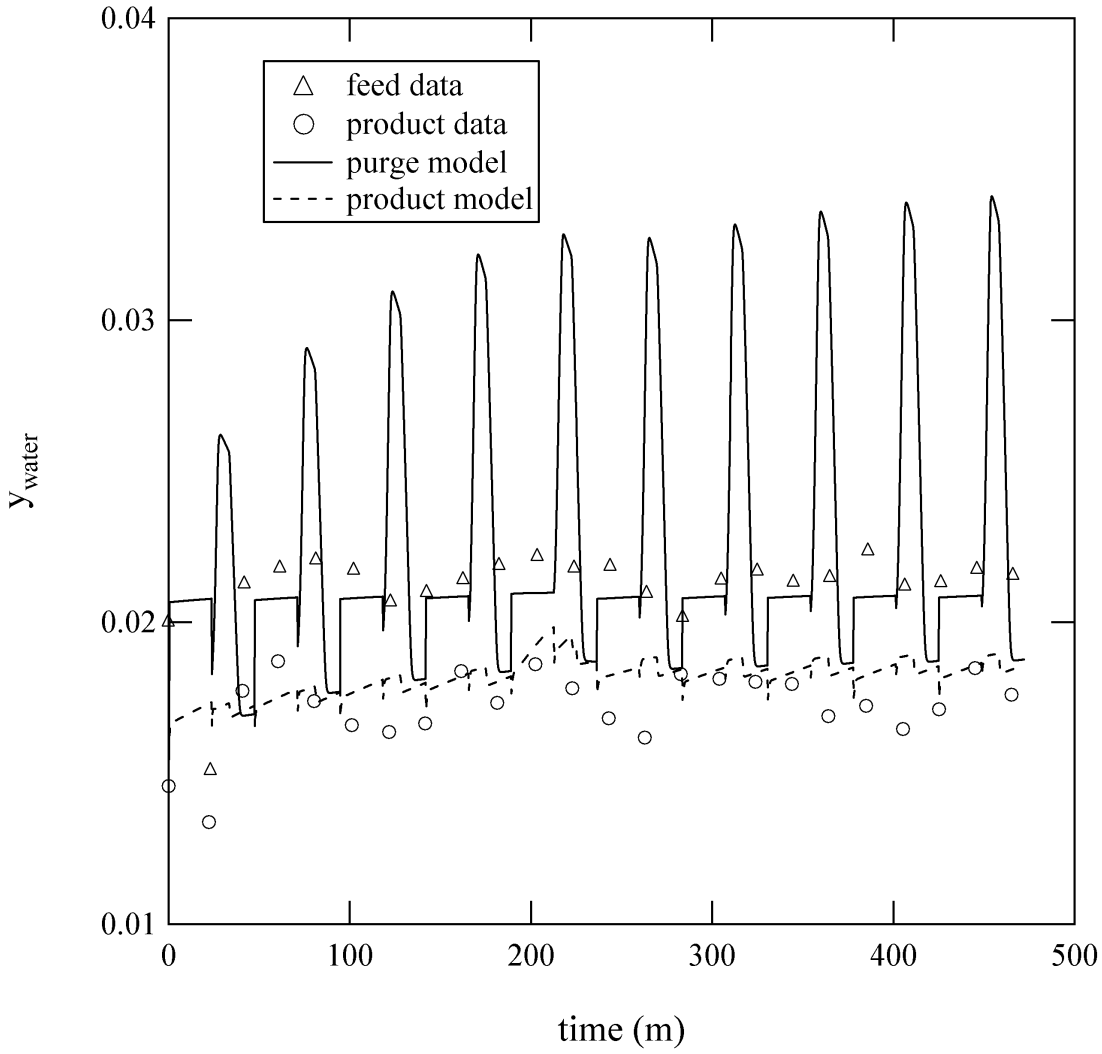

Figure 4.13 Product water concentration profiles for humid chloroethane challenge to TSA cycling with PICA carbon at conditions of Table 4.2 Run 7. Also shown are simulation product and purge profiles.

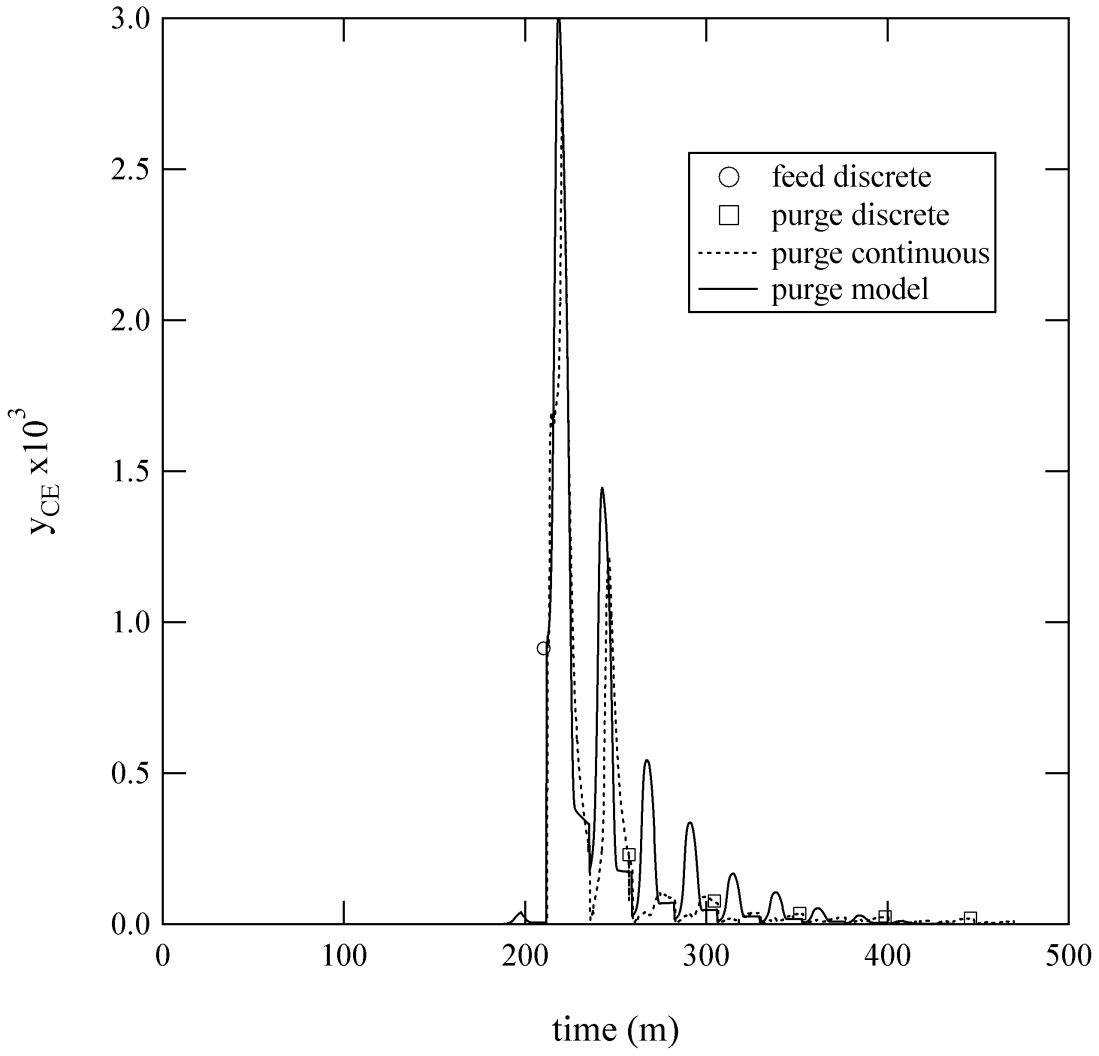

Figure 4.14 Purge chloroethane profiles for humid chloroethane challenge to TSA cycling with PICA carbon at conditions of Table 4.2 Run 7. Also shown is the simulation purge profile.

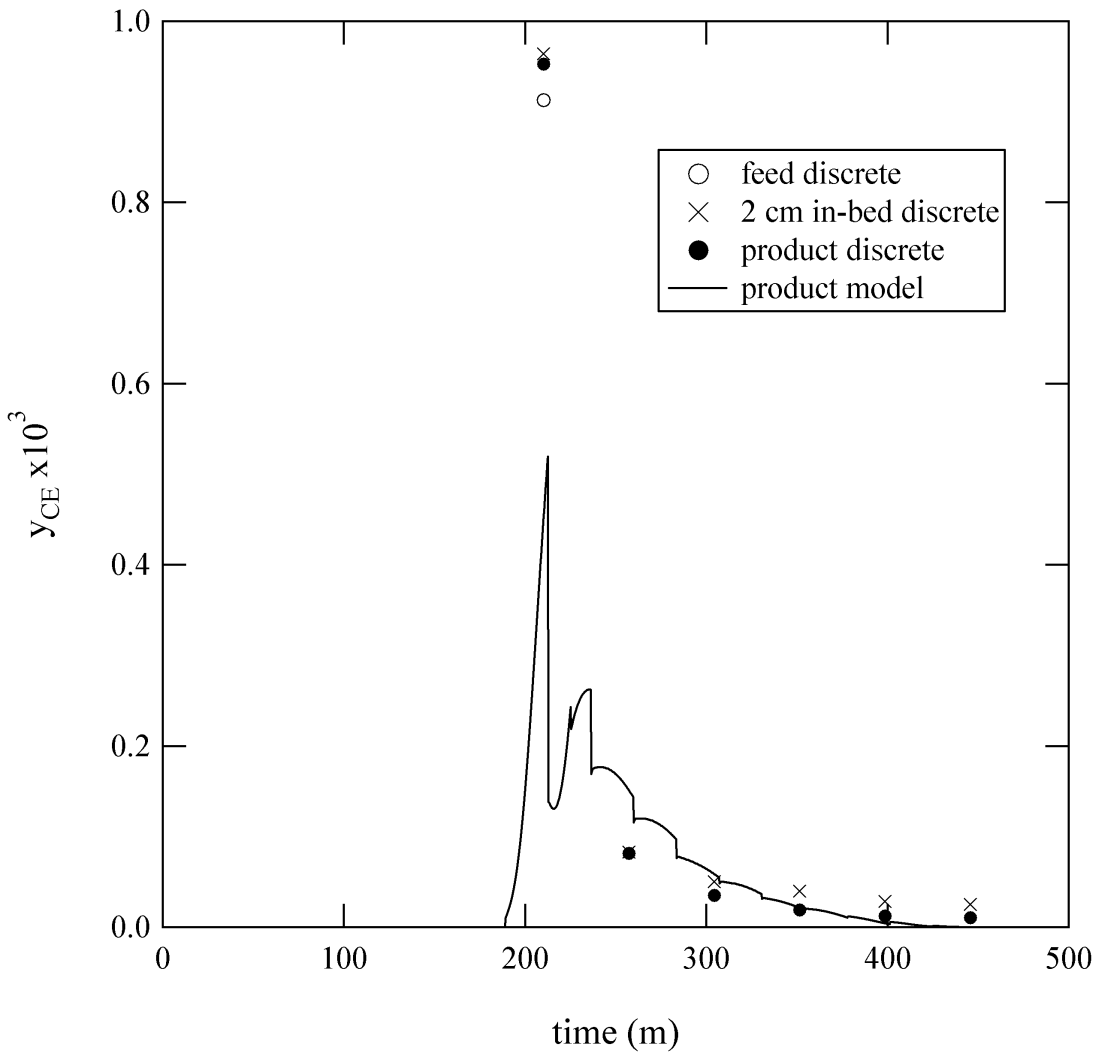

Figure 4.15 Product chloroethane profiles for humid chloroethane challenge to TSA cycling with PICA carbon at conditions of Table 4.2 Run 7. Also shown is the simulation product profile.

into the product however it takes 5 cycles to appear. A material balance indicated that 70% of the feed mass was desorbed after two cycles and 95% after 5 cycles for BPL in Run 7 and 70% of feed mass was desorbed by 5 cycles for Ambersorb 563 in Run 6. This is a result of a more favorable isotherm for chloroethane on Ambersorb 563 even though the capacity of BPL is greater than that of Ambersorb 563.

4.6 Cycle Concepts and Optimization

4.6.1 Approach

In purification processes the main objective is to maximize product mass delivery while limiting the maximum product contaminant concentration. Efficient adsorbent utilization requires that uptake occur over a significant fraction of the bed. The bed utilization is characterized by the mass productivity, taken as the ratio of product flow to adsorbent mass inventory. The system must also be optimized in terms of power consumed where a power productivity parameter can be defined as the ratio of supplied power to product flow. Recovery is the ratio of product flow to feed flow. Any regenerative filtration process can be analyzed with two descriptors: (1) the process flowsheet, (2) the steps that detail the flowsheet routing and duration. Design of an optimum flowsheet and steps, based on knowledge of these parameters requires both empirical and predictive analysis.

The simulation tool will be applied the analysis and optimization of the cycles discussed so far and other cycle concepts. Both a dry and humid case will be analyzed for the sensitivity to operating and system parameters. In addition the effect of heating schemes, process conditions, and adsorbent selection will be discussed.

4.6.2 2-Bed Cycle Analysis

The velocity of the adsorption wave must be slower than the purge wave of a cycle in order to prevent elution. In general an optimization approach would be to find conditions, which minimize the purge flow requirement while retaining the adsorption wave. This does not require complete regeneration of the bed. In order to minimize adsorbent inventory rapid cycling must be achieved. This requires that the bed depth be limited. For packed bed designs the effect of heat losses with increasing bed depth together with the heat capacity of the end fittings are important to consider in establishing on optimum bed depth. Shallow beds can perform better than a deeper beds because the cooling wave forces a fraction of the thermal wave out of the bed. For non-isothermal behavior the efficiency of the purge energy decreases with increasing bed depths for constant column volumes of feed and purge, i.e. the highest purge temperature does not reach the feed end. The heating time fraction has been shown to be approximately 50% simply because the cooling wave and heating wave travel as the same velocity. In general an optimization approach would be to find conditions, which minimize the purge flow requirement while retaining the adsorption wave. This does not require complete regeneration of the bed. In order to minimize adsorbent inventory rapid cycling must be achieved. This requires that the bed depth be limited. For packed bed designs the effect of heat losses with increasing bed depth together with the heat capacity of the end fittings are important to consider in establishing an optimum bed depth. Shallow beds can perform better than a deeper beds because the cooling wave forces a fraction of the thermal wave out of the bed. For non-isothermal behavior the efficiency of the purge energy decreases with increasing bed depths for constant column volumes of feed and purge, i.e. the highest purge temperature

does not reach the feed end. The heating time fraction has been shown to be approximately 50% simply because the cooling wave and heating wave travel as the same velocity.

A heating scheme based on the progress of the thermal wave at a position 2 cm from the feed end has been employed in the experimental work of this study. The appropriateness of this approach can be considered through the use of a TSA simulation by examining the effect of cooling time on the filtration behavior for a dry chloroethane feed to a bed of BPL carbon with 373 K purge temperature. Four simulation runs were conducted with different fractions of the purge step used for heating. The run conditions are established by setting the feed step to contain the adsorption wave. Four cases were then simulated using different fractional heating time a) cycle with no heated purge b) cycle with heat during entire purge c) heat for half of purge cycle d) heat for 75% of purge cycle. The feed breakthrough time was found to be 17 minutes. The purge time was then set at 17 minutes and feed concentration duration to twice the halfcycle time so that both beds of the 2-bed system are challenged.

Figure 4.16 presents the simulation results for the four cases over five cycles using logarithmic coordinates of concentration. The no heating case, corresponding to a heating time of 0, leads to chloroethane breakthrough of

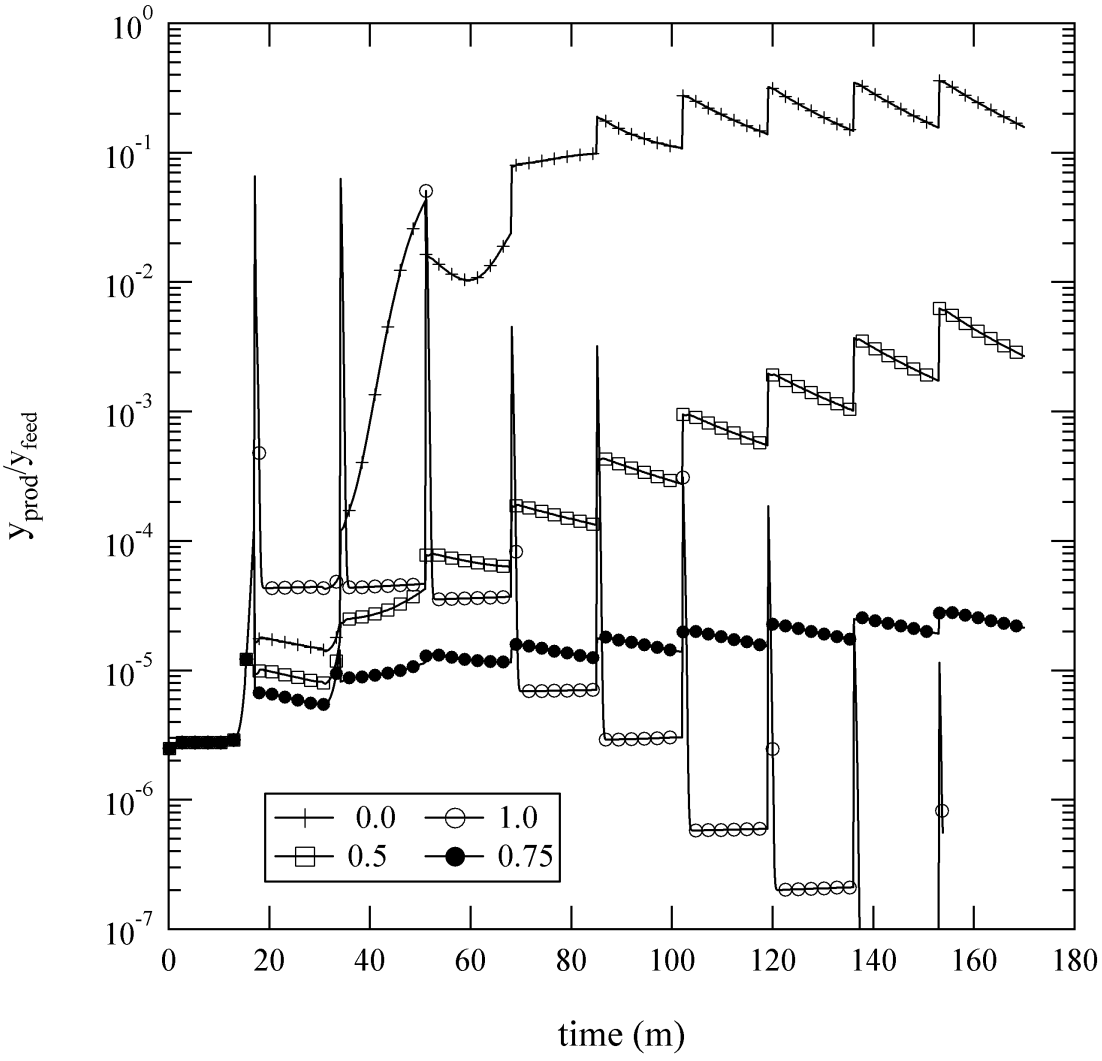

Figure 4.16 Cyclic product concentration profiles based on simulation with various fractions of time of the purge step when heat is input from 0 corresponds to no heating, 1 corresponds to heating the entire purge step.

increasing product concentration, which is reported as product mole fraction divided by feed mole fraction. Also apparent is some effect of bed cleanup associated with the slight pressurization of the feed and depressurization on the purge step. At a heating fraction of 0.5 a significant reduction in product concentration is observed versus the no heat case. At 0.75 fraction heating a low-level product concentration is maintained for each halfcycle during the feed step. The case of duration 0.75 heating results in a lower product concentration than for 0.5 over all cycles. The full duration heating case, duration 1.0, results in high product concentrations at the cycle changeover but extremely low concentrations in the latter part of the feed step. The case of heating during the entire purge cycle actually leads to a higher product concentration during the initial cycles when feed occurs but eventually results in low product concentrations, because the bed temperature is still high during a feed step all heating occurs. The fractional cooling time of approximately 0.5 used in this study seems to be reasonable based on this simulation. These results confirm that the cooling step is required for TSA operation such as considered here where high purification is required and the feed step alone cannot cool the bed to an adsorption temperature corresponding to a significant adsorption loading.

Next simulations were conducted in order to establish the effect of various heating schemes, illustrated in Figure 4.17. A simulation was conducted using heated purge and the efficiency of regeneration evaluated. Also in-bed heating was simulated by assuming that a heat source was placed at an in-bed location corresponding to various stages in the fixed bed model. The cycle consisted of co-

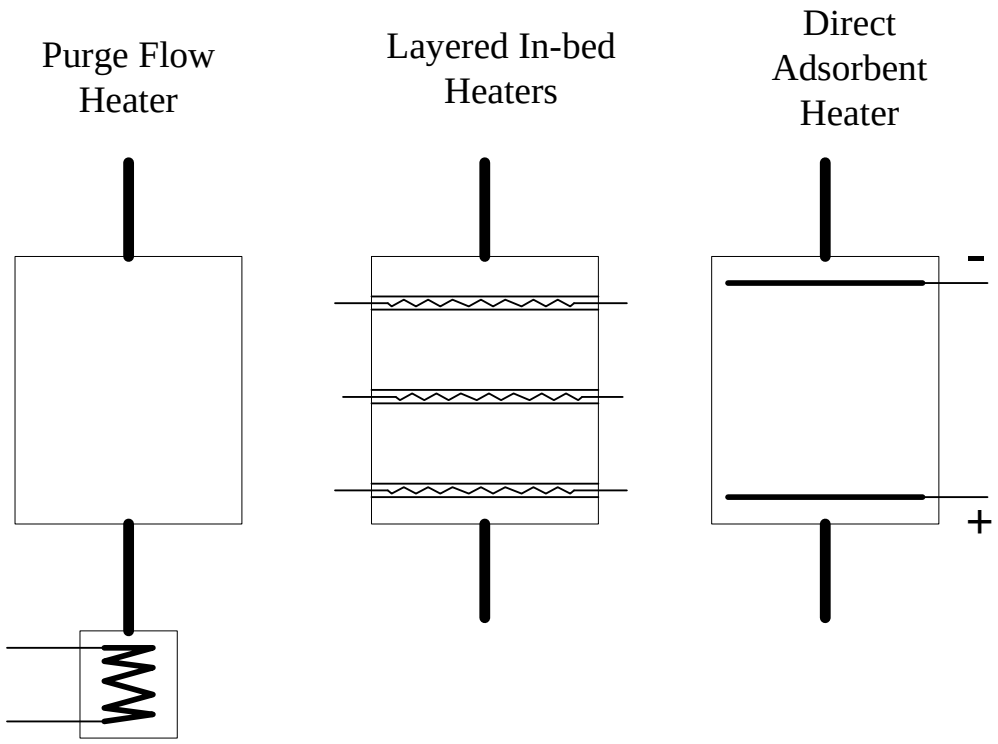

Figure 4.17 Bed concepts for purge end, in-bed layered and electrical resistance heating.

current feed, followed by countercurrent purge with heat input at the purge inlet and mid-point of the adsorbent bed. The simulation results presented in Figure 4.18 are obtained using equivalent power input for heating at different locations in the bed. The cycle time was chosen to contain the feed concentration wave. Heating included equal times for heating and cooling. For the case with heated purge only the product concentration remains free of contaminant while for the power input distributed equally over the length of the adsorbent contaminant is noted in the product starting at the end of the second cycle. This suggests that the equidistant heating is less efficient for purification applications on an equivalent energy basis compared to heated purge.

The effect of humidity on product purity, where the cycle time is set to provide the one half temperature at the feed end, is summarized in Figure 4.19 -Figure 4.21 for BPL, Ambersorb 563 and PICA respectively. Not all of these experiments have the conditions listed in Table 4.2 but in each case the approach to establish the conditions was the same as outlined earlier with regard to the time for the purge temperature wave. These figures indicate that for all three adsorbents studied there is the expected increase in adsorption time and product purity with humidity. An interesting point to note is that there were two PICA experiments at dry conditions, where for a τ_{ads} equal 3300 (Run 10) no breakthrough to the product was observed while for τ_{ads} equal 7300 (Run 9) the product concentration increased to 30 mg/m^3 because of the finite bed capacity.

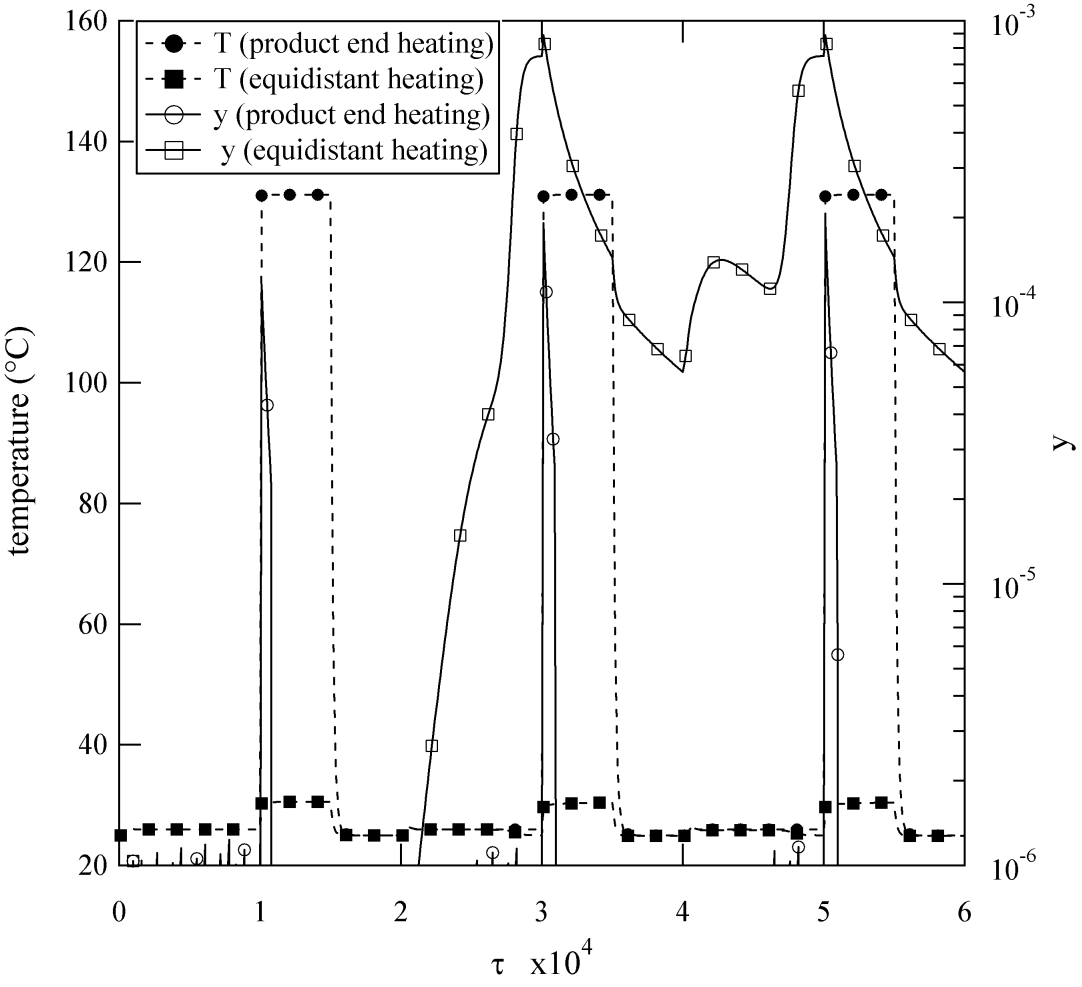

Figure 4.18 Simulation of cycle behavior for purge end heating and equidistant heating.

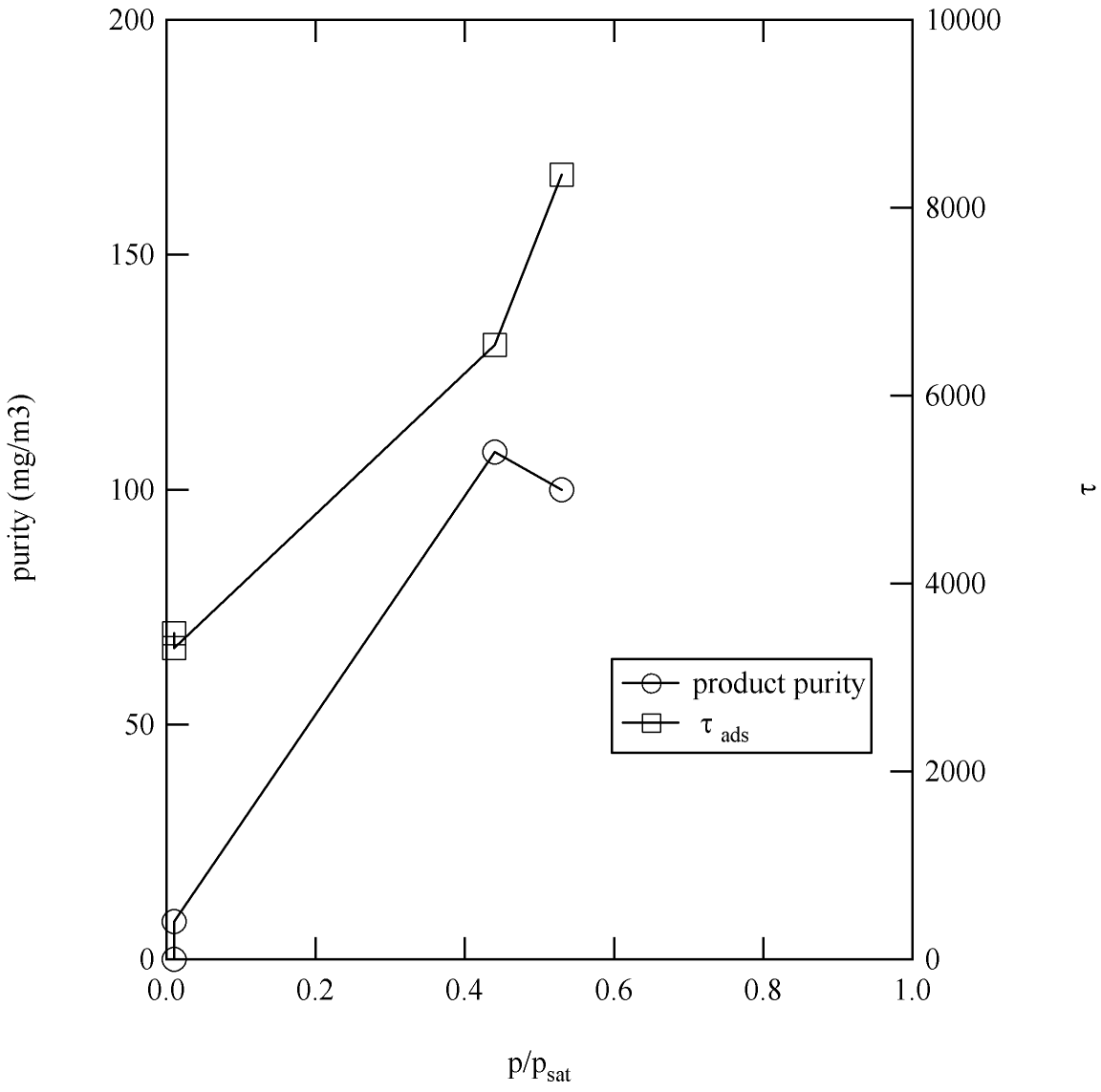

Figure 4.19. Product purity, adsorption time versus relative humidity for the TSA cycling experiments with BPL carbon.

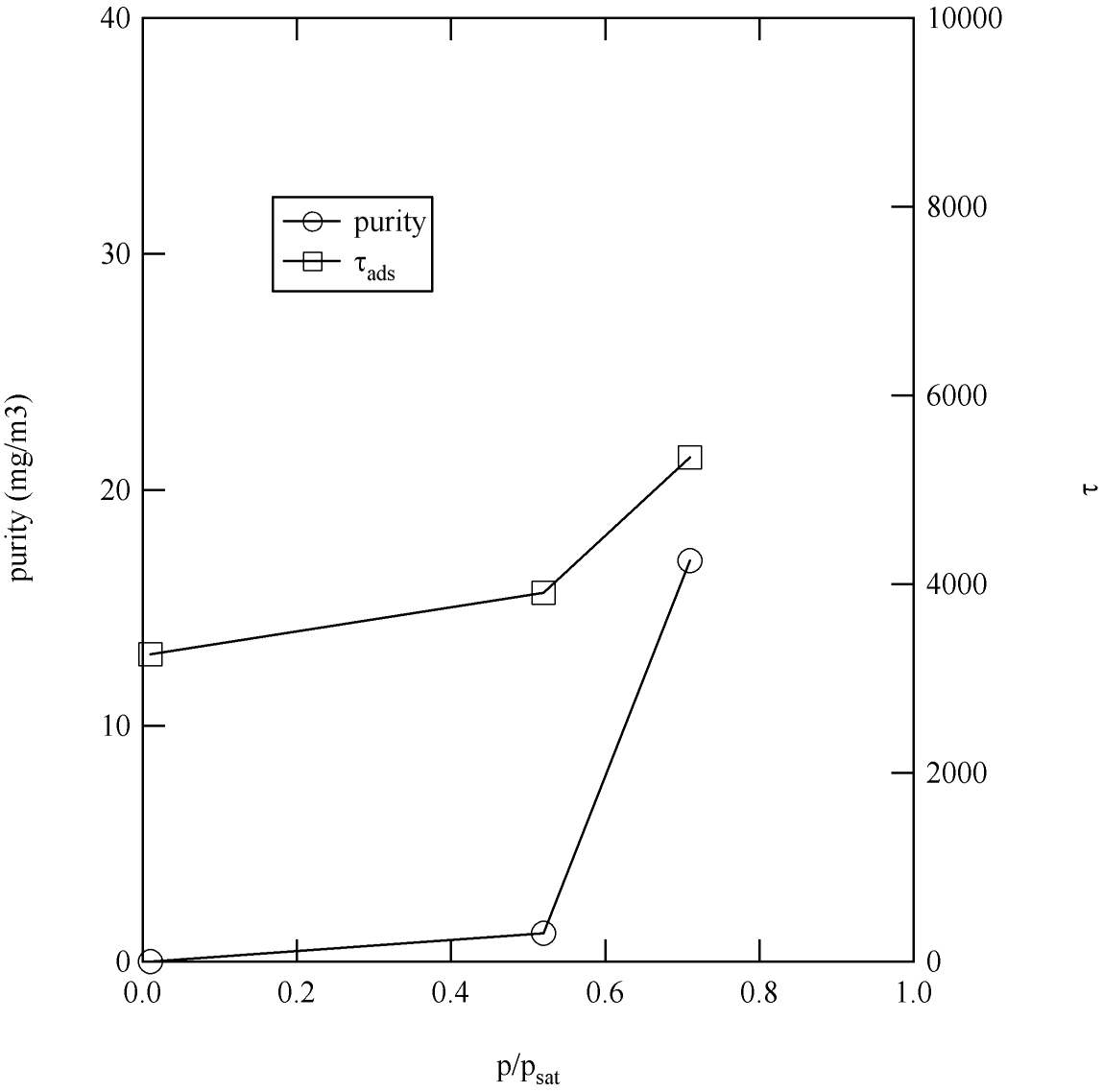

Figure 4.20. Product purity, adsorption time versus relative humidity for the TSA cycling experiments with Ambersorb 563 carbon.

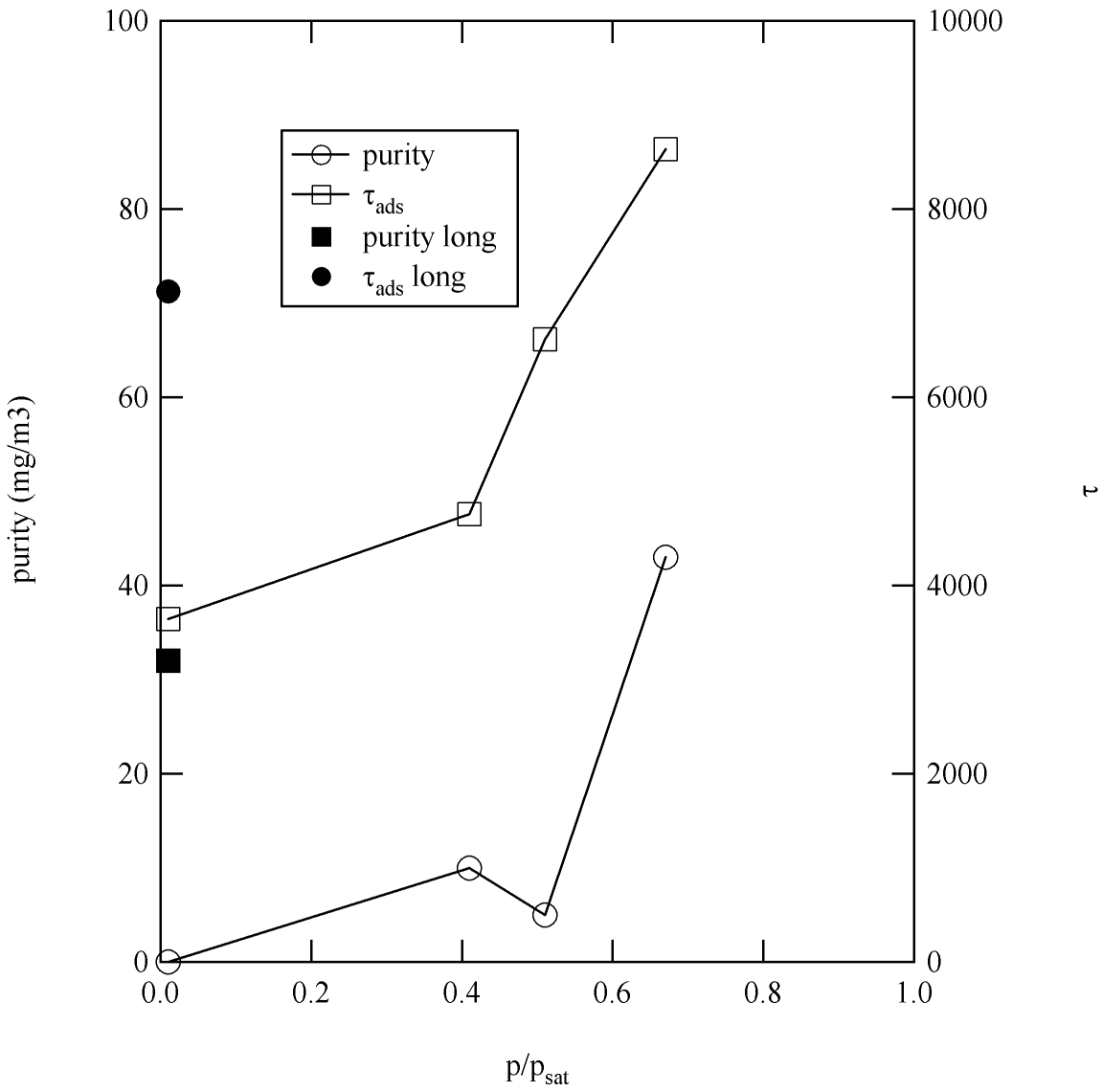

Figure 4.21. Product purity, adsorption time versus relative humidity for the TSA cycling experiments with PICA carbon.

The purge to product mass flowrate ratio, ϕ, is a metric of the process efficiency. Reducing ϕ is a process objective where the tradeoff is easily determined. Assuming a constant feed step velocity, the relative adsorbent inventory increases linearly with ϕ. The purge to feed velocity is an important term, which determines the rate of bed purging. Because the velocity is a function of the bed pressure and the mass flowrate and the product mass flow can be written as the sum of feed and purge, this ratio can be written in terms of the purge to product mass flowrate ratio according to $\phi(P_{feed}/P_{purge})/(1+\phi)$. The purge to feed velocity ratio increases less than linearly with ϕ. Figure 4.22 presents these relationships for the pressure ratio of 1.0 and 1.2, the latter recorded in the present experiments. This suggests that process efficiency can be best achieved by keeping ϕ below 0.5, in order to minimize the adsorbent mass and velocity ratio differentials. In these experiments where the bed pressure was significant, ϕ has been chosen between 0.3-0.5.

A summary of the effect of heating time for these experiments versus those reported earlier by Davis and LeVan (1989) is shown in Figure 4.23. The results are in good agreement under dry conditions and the larger increase in cycle time associated with humid operation is also apparent. However it is not possible to determine the optimum of τ_{heat}/τ_{ads} from the limited number of experiments presented here.

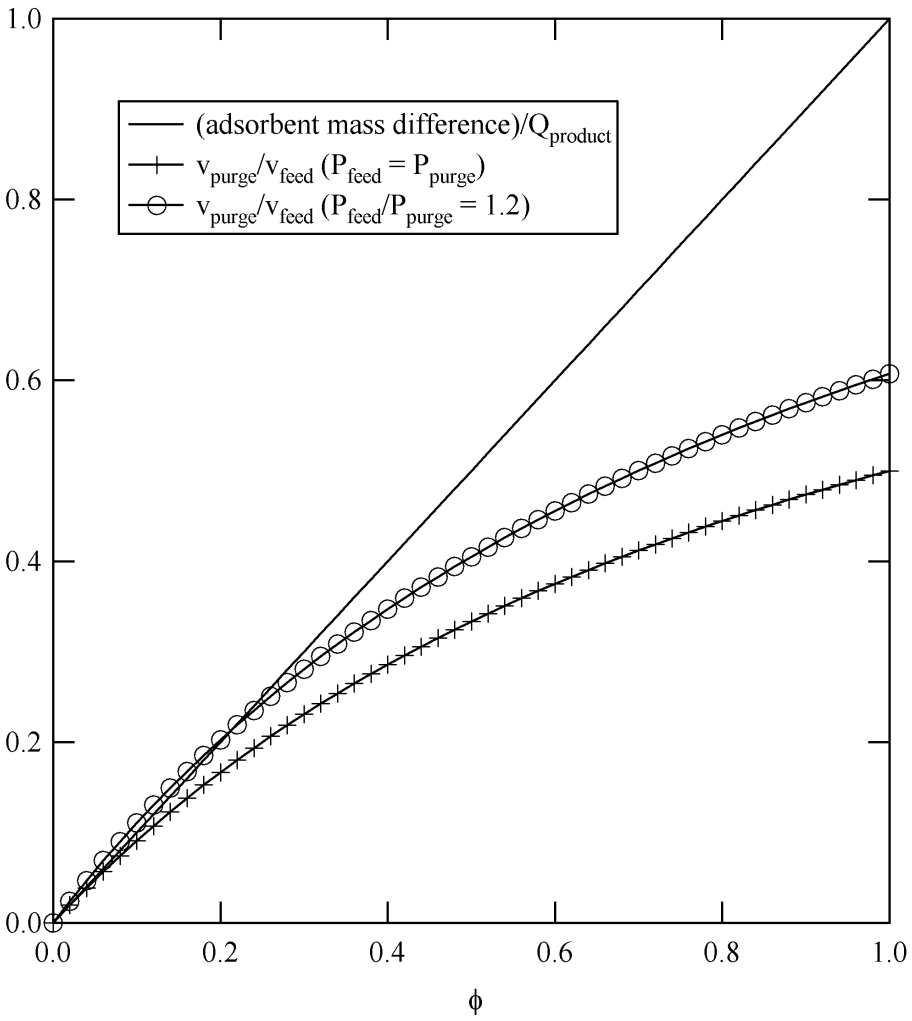

Figure 4.22 The purge/feed velocity ratio with a pressure ratio of 1.0 and 1.2 and the adsorbent inventory-to-product mass flow ratio versus the purge-to-product mass flow parameter, ϕ.

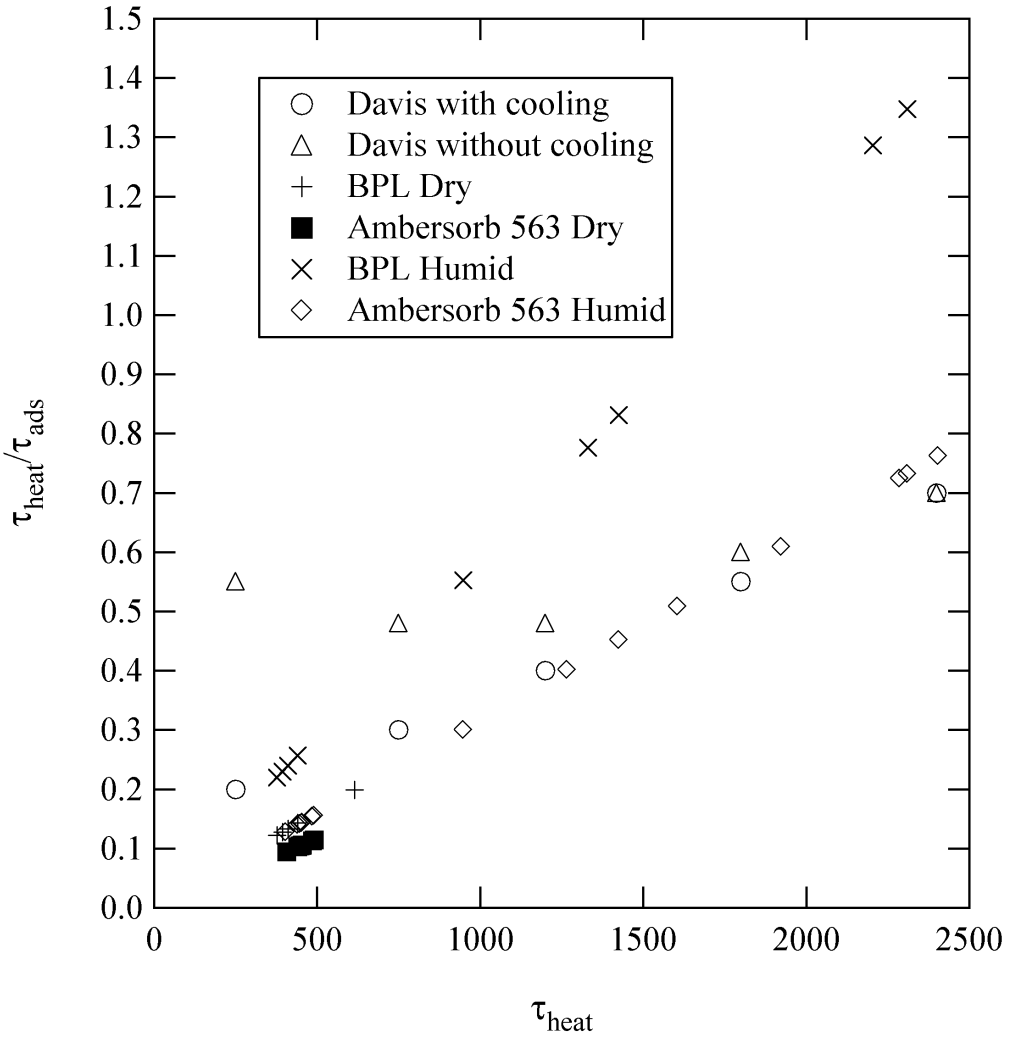

Figure 4.23 τ_{heat} / τ_{ads} for laboratory system and work of Davis and LeVan (1989).

4.6.3 Simulation Optimized Cycle

In the experiments discussed so far τ_{heat}/τ_{ads} was established based on the velocity of the heating and cooling waves. This assumed that feed to a cool bed would yield the minimum product purity. This assumption can be examined. Figure 4.24 shows that the product purity versus τ_{heat}/τ_{ads} for the conditions of Run 8, humid feed, has a minimum at 0.7, which indicates that the bed should not be cooled completely. However the actual behavior of the experimental system does not exhibit this same optimum also shown in Figure 4.24. The finite heat capacity at the purge end does not allow for rapid low temperature purge. Another possible comparison between the simulation and data would be to obtain a set of optimum conditions at the same productivity as observed for Run 5, which had the highest purity (lowest product concentration) of the recorded runs but was near the detection limit, so an optimum might not be detectable.

The TSA process can be optimized by increasing adsorption time (reducing humidity, decreasing feed temperature) or decreasing purge time (heating and cooling without purge). The effect of feed temperature was examined. Several runs were conducted at a reduced feed temperature by passing the feed through a condenser. A slight reheating occurred to ambient temperature. Low feed temp experiments (Run 9 a 14 minute halfcycle with breakthrough, Run 10 with a 9 minute half cycle resulted in no breakthrough). The effect of humidity on performance is illustrated where the conditions used to simulate Run 7 in Figure 4.25 at a feed temperature of 298 K were in addition simulated at 308 and

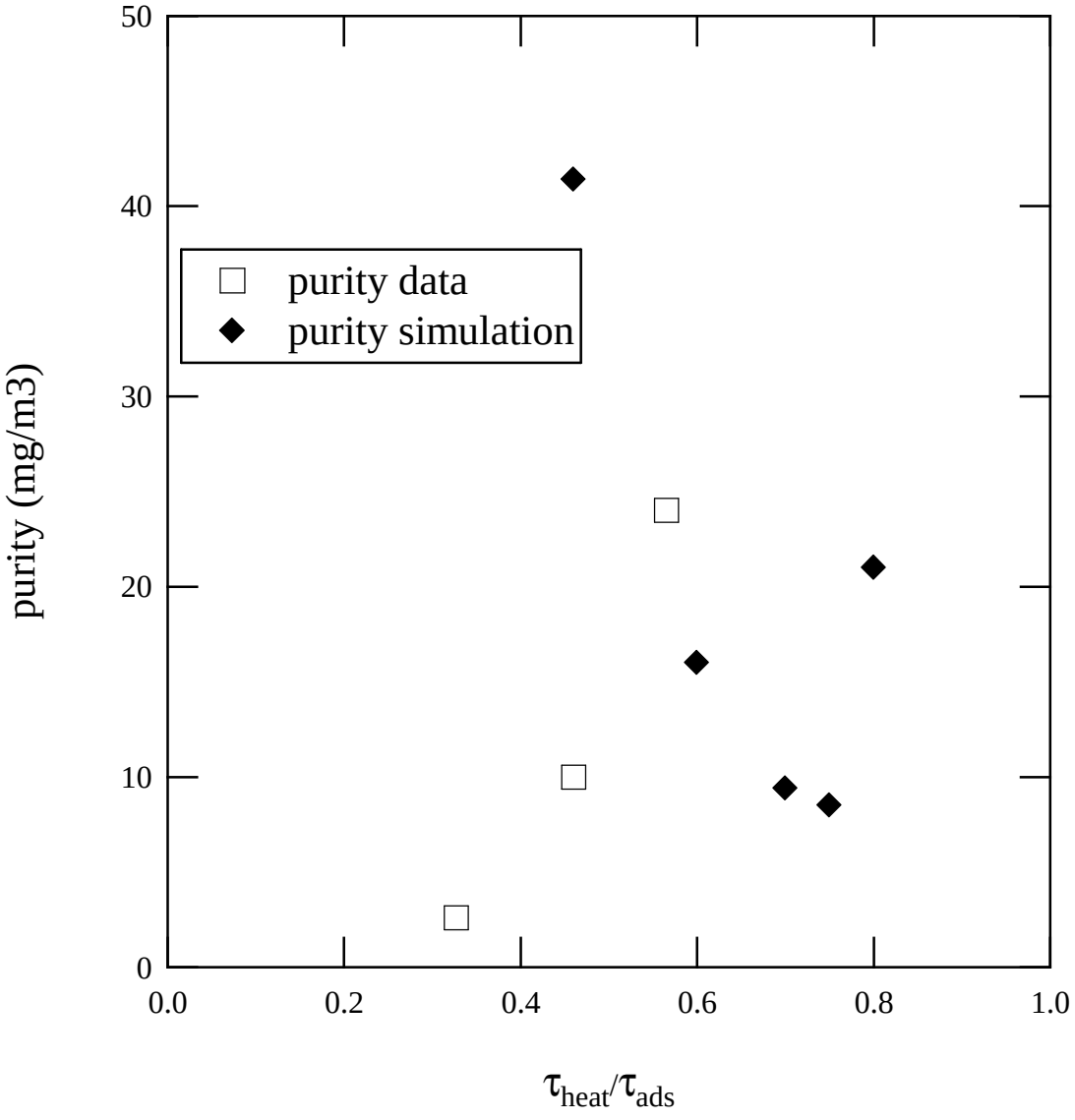

Figure 4.24 Effect of τ_{heat} / τ_{ads} on purity for chloroethane to PICA carbon TSA humid cycling conditions of Run 8 in Table 4.2.

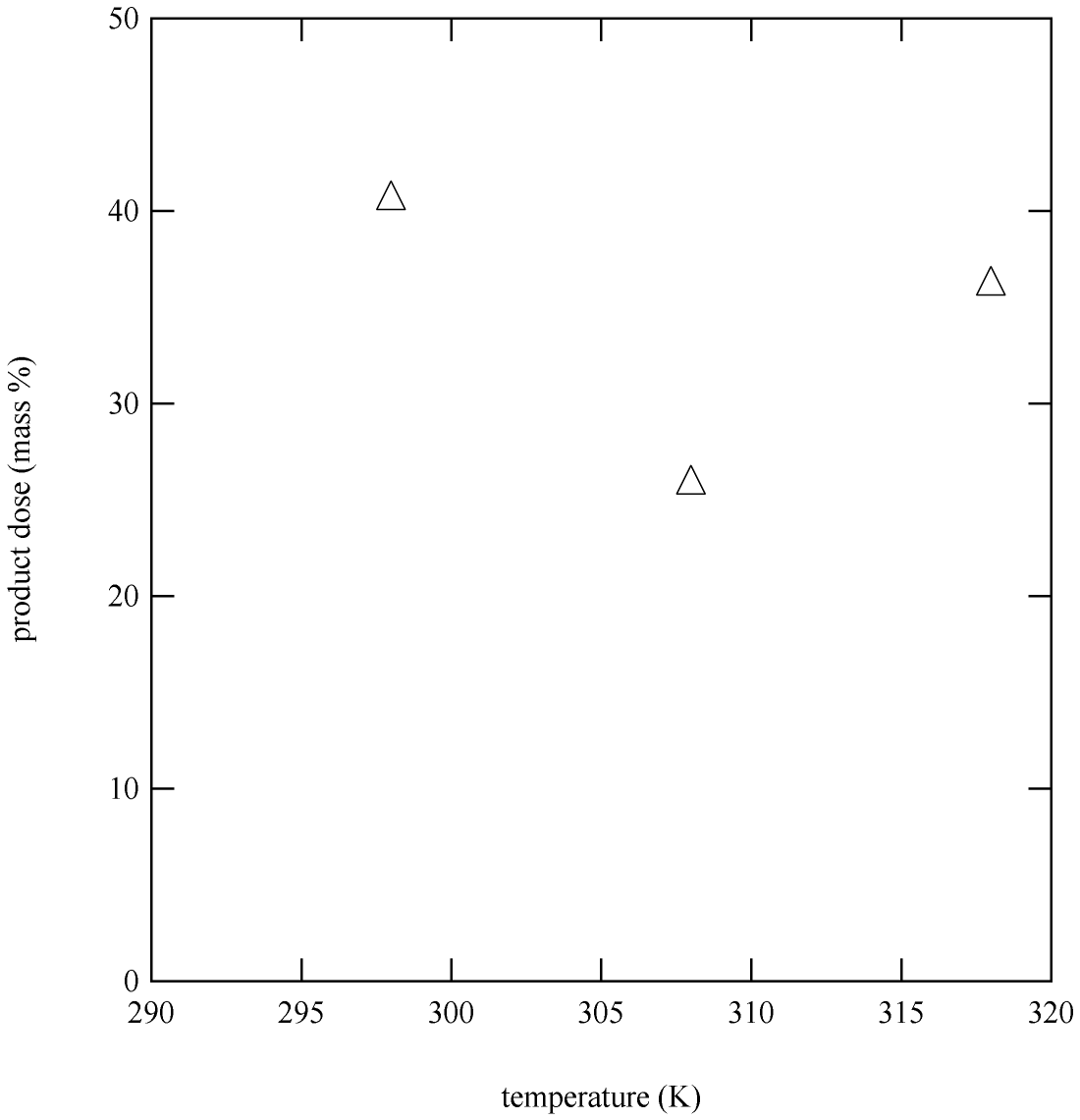

Figure 4.25. Simulation results for Run 8 at several feed temperatures.

318 K corresponding to 88, 51 and 29% relative humidity respectively. The optimum corresponds the tradeoff between the adsorption capacity of water at different relative humidity versus reduced chloroethane adsorption capacity at increased temperature.

The reproducibility of the thermal swing adsorption system could be evaluated using three sets of experiments conducted under nearly identical conditions. Figures x present the purge and product concentration recorded for one of the sets of repeat experiments. As stated earlier the cycle switching was conducted manually so there is not exact time agreement between experiments. An instructive approach to evaluate reproducibility of the purge concentration, as recorded by the continuous detector, would be to compare the cumulative purge dose between experiments. Here the integrated purge concentration, eqn 4.15

$$C_{t,purge} = \int c_{purge} dt \tag{4.15}$$

is used to calculate the purge difference eqn.4.16

$$\Delta_{purge} = \frac{\sum abs\left[\frac{(C_{t,purge,1} - C_{t,pureg,2})}{\frac{(C_{t,purge,1} + C_{t,purge,2})}{2}}\right]}{N} \tag{4.16}$$

In addition the product concentration difference can be examined, where this was only measured once per cycle so discrete values for each cycle are compared eqn 4.17.

$$\Delta_{product} = \frac{\sum abs\left[\frac{(c_1 - c_2)}{\frac{(c_1 + c_2)}{2}}\right]}{N} \tag{4.17}$$

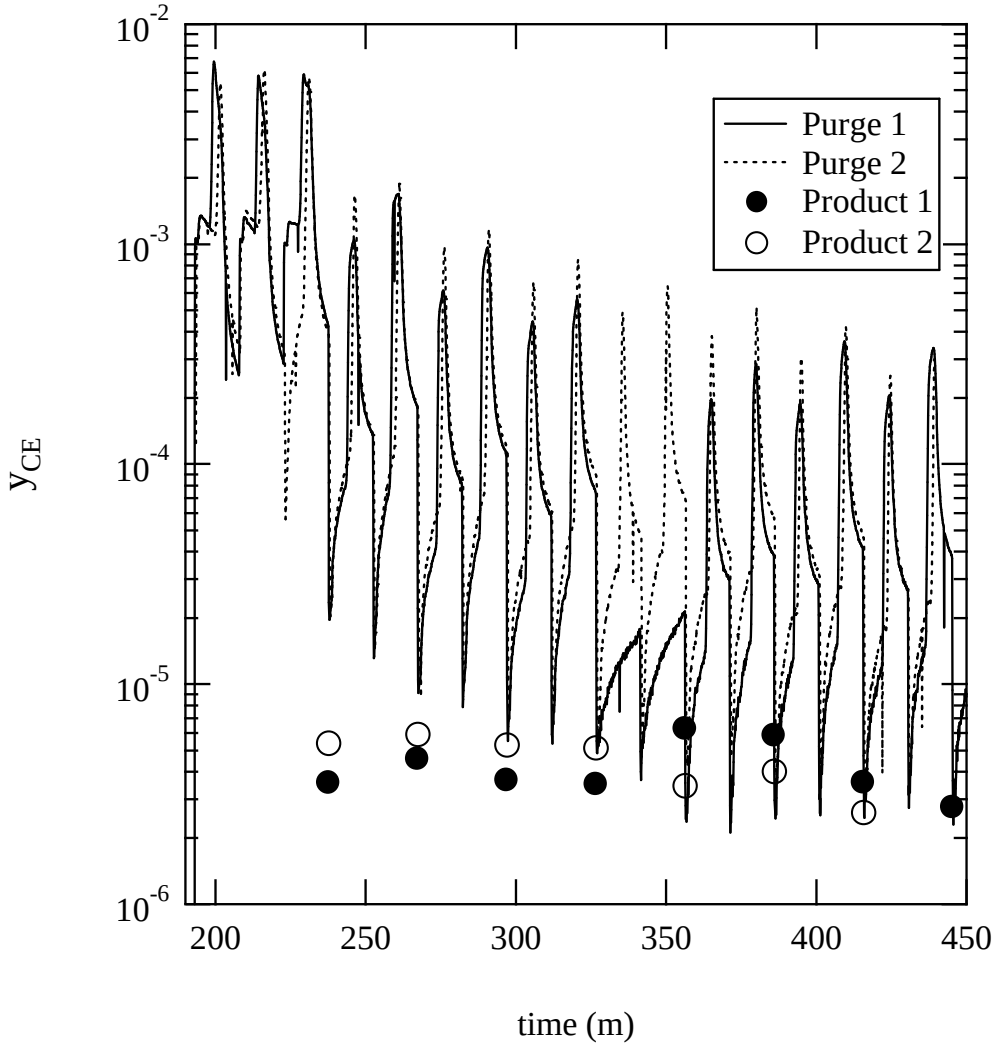

Figure 4.26 Repeated TSA runs, purge and product concentration profiles

Table 4.4 summarizes the reproducibility results in terms of relative difference in purge dose, Δ_{purge} , and relative product concentration difference, $\Delta_{product}$. It can be seen that the agreement for purge dose is approximately 15%, which is related to the ability to deliver the feed dose consistently. The product concentration relative difference is 51%.

The sensitivity of the thermal swing adsorption model was also investigated. Base case conditions were chosen for the simulation corresponding to Run 7. The integrated product dose, defined in eqn. 4-18,

$$C_{t,\,product} = \int c_{product} dt \tag{4.18}$$

obtained from the simulation was evaluated at the base case and with an adjusted parameter value these were then used to determine parameter sensitivity by eqn. 4-19

$$\delta_{product} = abs\left(\frac{\partial C_{t,\,product}}{\partial P}\right)\frac{P_{base}}{C_{t,\,product,base}} \tag{4.19}$$

The simulation parameter sensitivities are listed in Table 4.5. From this analysis none of the parameters considered is most significant but the particle internal diffusion rate and Peclet number have the greatest sensitivity of 6%. This would be expected for low level concentration breakthrough.

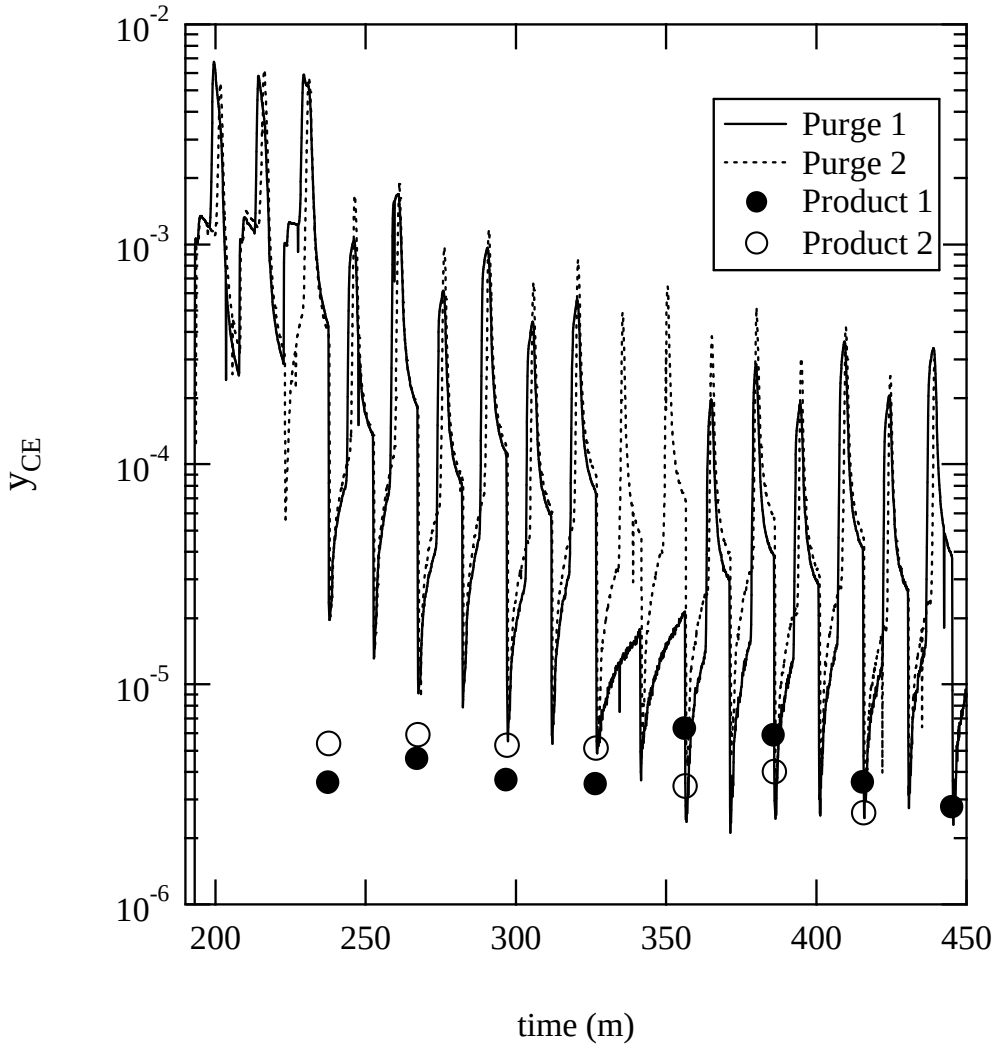

Figure 4.26 Repeated TSA runs, purge and product concentration profiles

Table 4.4 TSA experiment concentration reproducibility for three sets of repeated experiments.

	Δ_{purge}	$\Delta_{product}$
Set 1	0.13	0.38
Set 2	0.31	0.30
Set 3	0.014	0.85
Avg	0.15	0.51

Table 4.5 TSA simulation parameter sensitivity using Run 7 as base case conditions.

	$\delta_{product}$
kva	0.0045
kpa CE	0.063
kpa water	0.010
Pe	0.0001
Pe_T	0.055
ha	0.028

4.7 Conclusions

A series of experiments were performed using the two-bed thermal swing system. The approach focused on collecting data appropriate for the design of vapor filtration in the presence of humidity. Data obtained from this study included results for packed beds of activated carbon. The results presented here for breakthrough and thermal cycling agree well with the simulation using the novel multicomponent equilibria model developed earlier. Design rules for a 3-step 2-bed thermal cycle have been presented and applied cyclic adsorption data. The implication of coadsorption effects was compared using high (BPL and PICA activated carbon) and low (Ambersorb 563) water capacity adsorbents. Optimization of the 2-step thermal adsorption cycle for a moderate volatility vapor, chloroethane, was not able to identify a feasible set of conditions to achieve high purity levels under high humidity conditions.

Chapter 5: Particle Scale Transport

5.1 Introduction

There are many approaches to describe transport properties of microporous adsorbents. An understanding of this behavior is important for low concentration separations and off-gassing behavior from surfaces. In amorphous, or heterogeneous adsorbents such as activated carbon, silica and alumina particle scale the transport resistance is governed by several mechanisms in both the gas and adsorbed phase. In addition chemical reactions and surface interaction can occur in the adsorbed phase, which would be subject to transport resistances. Particle scale transport for adsorbed species is important for adsorber process design. Several authors have examined hexane diffusion; however the reported rates of diffusion vary by four orders of magnitude. Here an experimental vapor phase uptake system is examined. A series of experiments are used to determine the controlling transport rates for the adsorbed systems. The adequacy of available models will be assessed.

5.2 Particle Scale Transport

Methods to describe mass transfer rates from the vapor phase to adsorbent particles typically invoke the concept of combined resistances. The phase transition is considered to be fast and the adsorbed phase equilibria relationship offers a means to equate the concentration between vapor and adsorbed phases. Many models to describe intraparticle adsorption rate behavior have been proposed. A potential difficulty in interpreting the modeling results would be that parameter values for rate terms or intraparticle diffusivities are model dependent, and the mechanisms require a particle geometry, which

is often poorly characterized. Depending on the operating regime various resistances may be regarded as fast or negligible, which leads to implications for model development.

Experimental methods to investigate adsorption rate behavior can be categorized as either steady state or transient. Among the latter each can affect either differential or integral changes in adsorbed phase concentration. Convection and dispersion effects for heat and mass transfer influence experimental methods based on packed beds of adsorbent particles. Therefore it is revealing to consider particle scale transport at the particle scale rather than as a lumped effect of many particles. Gravimetric methods have been used successfully for these measurements.

In the case of gravimetric rate measurements an overall fluid phase component balance on a basket in a flowing stream can be written as

$$V\frac{dC_B}{dt} = Q_B\left(C_F - C_B\right) - \frac{m}{\rho_p}N_A a_v \tag{5.1}$$

where, N_A, is the molar flux in terms of a fixed coordinate frame. This allows for the concentration gradient between a basket and the flowing stream.

The film resistance associated with the boundary layer penetration results from combined diffusion and convection. The flux associated with film mass transport rate is written in terms of a film coefficient

$$N_A = k_f\left(c_{A,B} - c_{A,i}\right) \tag{5.2}$$

where $c_{A,B}$ represents the concentration in the basket and c_{Ai} the concentration at the outer radius of the particle. The film coefficient has been well correlated for single particles. The corresponding flux for film resistance heat transfer is

$$q\big|_{r=r_0} = h_f a_v (T_B - T_i) \tag{5.3}$$

The film mass transfer resistance becomes negligible for adsorption of pure components. Available correlations for sphere film coefficients, k_g and h_f, expressed in terms of Sherwood and Nusselt numbers are available (Geankopolis, 1984).

$$N_{Sh} = 2 + 0.552 N_{\mathrm{Re}}^{0.53} N_{Sc}^{1/3} \tag{5.4}$$

$$N_{Nu} = 2 + 0.6 N_{\mathrm{Re}}^{0.5} N_{\mathrm{Pr}}^{1/3} \tag{5.5}$$

Adsorbent particles for efficient separations are designed to incorporate a bidisperse pore structure. The largest fraction of pores is in the micropore region, < 2 nm, while a still significant number of larger pores are present. Transport in larger pores is governed by pore diffusion, which can have contributions of three resistances, molecular and Knudsen diffusion and Poiseuille or viscous flow. Transport in micropores can depend on micropore diffusion or hindered access. Micropore diffusion occurs due to flux in the adsorbed phase while hindered access to pore cavities results from steric effects. For adsorbents with a microparticle structure the characteristic dimensions of micropore diffusion is the microparticle. There are conflicting uses of the term surface diffusion in the literature. In some cases it is synonymous with micropore diffusion (Ruthven, 1984) in others it is used to describe skin resistance or pore blockage at the particle surface (Ruthven, Farooq and Knaebel, 1994) but always written in terms of adsorbed phase loading. Surface diffusion is referenced to the concentration gradient over the whole pellet not the microparticle because of an absence of knowledge of the surface. Surface diffusion has also been given the definition of adsorbed phase transport on the surface of micropores and macropores throughout the particle in parallel with gas phase transport (Yang, 1987). For large or macro- pore transport at high vapor concentrations molecular diffusion is dominant, at low vapor concentrations Knudsen diffusion dominates and under an applied pressure gradient Poiseuille flow can be important.

Typically a distributed parameter model is used to describe particle scale transport. The particle material balance is written as

$$\varepsilon_p \frac{\partial \bar{c}_A}{\partial t} + \rho_p \frac{\partial \bar{n}_A}{\partial t} + \nabla \cdot \left(\varepsilon_p N_p + \varepsilon_p N_v + \rho_p N_S \right) + a_{v,mp} \mathbf{N}_{D,mp} \Big|_{r_{mp}=r_{mp,0}} = 0 \qquad (5.6)$$

with fluxes due to pore, viscous, and surface diffusion and microparticle diffusion.

The flux in the macropores can be written as

$$N_P = y_A \left(N_A + N_B \right) - D_{MP} \nabla c_A \qquad (5.7)$$

where, for diffusion through a porous particle, the tortuosity of the particle must be considered

$$D_{MP} = \frac{D_P}{\tau} \qquad (5.8)$$

The pore diffusion is vapor phase transport and considered to occur in the macropores and mesopores. Knudsen diffusion results from the gas phase transport through pores with diameters less than mean free path length. If the macropores are small enough that Knudsen diffusion would be important and in the case of equimolar counter diffusion then the transition from molecular to Knudsen diffusion could be described using the Bosanquet equation (Froment and Bischoff, 1979).

$$\frac{1}{D_p} = \tau \left(\frac{1}{D_m} + \frac{1}{D_K} \right) \qquad (5.9)$$

The Knudsen diffusivity is calculated by (Geankopolis, 1984).

$$D_K = 9700 R_p \left(\frac{T}{MW} \right)^{1/2} \qquad (5.10)$$

In highly microporous adsorbents surface and microparticle diffusion will be dominate versus Knudsen diffusion. In macropores molecular diffusivities are smaller than

Knudsen diffusivities, $D_m << D_k$. The pore diffusion flux, for trace vapor concentrations of adsorbing species can then be written as

$$N_P = -\frac{D_m}{\tau}\frac{P}{R_g T}\nabla y_A \tag{5.11}$$

For the case where the gas phase mole fraction of the adsorbing species is low, it was shown by Taqvi et al. (1997) that macropore convection could be neglected.

The viscous flow term associated with a pressure gradient across the adsorbent, referred to as Poiseuille flow, can be written as

$$N_v = -(\nabla \rho v) \tag{5.12}$$

but from Darcy's law

$$v_o = -\frac{\kappa}{\mu}\nabla p \tag{5.13}$$

if only one component of the concentration varies in the particle, i.e. a non-adsorbing carrier with a dilute contaminant then the viscous flux can be written as

$$N_v = \left(\frac{\kappa}{\mu} c_A \nabla p\right) = \frac{\kappa}{\mu}\frac{p^2}{R_g T} y_A \nabla y_A \tag{5.14}$$

The permeability, κ, can be determined from the geometry of the problem using the Hagan-Poiseuille law

$$\kappa = \frac{R^2}{8}\frac{1}{\tau_v} \tag{5.15}$$

Two processes describe intraparticle transport associated with pores on the order of molecular dimensions: micropore and intracrystalline diffusion. The relative importance of transport in small pores to the overall transport could be lessened due to the presence of numerous interconnecting large pores through which molecular diffusion is still possible. In the case of physical adsorption with a large adsorbed phase

concentration, movement in a two-dimensional sense can occur leading to surface diffusion. Surface diffusion cannot be measured independent of the other resistances. It is a transport effect, which occurs in parallel with pore diffusion. Intracrystalline diffusion is associated with hindered transport through finite dimension openings such as found in zeolite crystals and carbon molecular sieves. This is also called configurational diffusion. In the case of micropore diffusion steady state molecular movement can be observed using tracer methods. The same mathematical development described here is applied to both surface diffusion and micropore diffusion.

Both surface and micropore diffusion can be expressed with a Fickian type model based on the gradient in adsorbed phase concentration. It is convenient to define an effective or transport molar flux in terms of the Fickian model

$$J_{s,c} = -D^{s}_{trans}(n_A)\nabla n_A \tag{5.16}$$

based on the gradient of concentration. The activation energy for diffusivity is assumed to take the usual Eyring form

$$E = \exp\left(\frac{-E}{RT}\right) \tag{5.17}$$

This transport diffusivity has been found to be concentration dependent for both surface and micropore diffusion. The true driving force for diffusion, either surface or micropore diffusion, is governed by the gradient in chemical potential not concentration, where the molar flux for a single component is expressed as

$$J_{s,c} = -\frac{n_A D^{s}_{o}}{kT}\nabla \mu_A \tag{5.18}$$

Here D_o is the mobility and n_A is the adsorbed phase concentration. The mobility for physical adsorption corresponds to a two-dimensional movement on a surface associated

with small surface barriers and is concentration dependent. The transport diffusivity and mobility are related. By definition the chemical potential is written as

$$\mu = \mu_o + kT\ln(a) \tag{5.19}$$

For an ideal gas the activity can be represented by the partial pressure so, if one assumes that the chemical potential in the vapor phase is the same as the chemical potential in the adsorbed phase

$$\mu = \mu_o + kT\ln(p) \tag{5.20}$$

The Fickian transport diffusivity is related to the mobility through eq. 5.4-5.7 such that

$$D_{trans} = D_o\left(\frac{\partial \ln(p)}{\partial \ln(n)}\right) = D_o\Gamma \tag{5.21}$$

This is the Darken equation, which applies concentration dependence to diffusion as opposed to the Fickian approach, which is a constant diffusivity. The term Γ is close to unity for gases but is significant for liquids and adsorption. Since the chemical potential driving force is related to the rate of entropy production, the self diffusion is described by both the straight and cross coefficients of irreversible thermodynamics. The transport diffusivity consistent with the Fickian model is different from the self-diffusivity determined by tracer exchange under equilibrium conditions. The Darken relationship has also been used to predict effective transport rates from tracer studies based on

$$D_{AB} = \left(D_A^* x_A + D_B^* x_B\right)\Gamma \tag{5.22}$$

where D* is the self-diffusivity.

Multicomponent diffusion can be modeled using the Maxwell-Stefan equations (Krishna and Wesselingh, 1997). For multicomponent diffusion of gases at low density the Maxwell-Stefan equations are appropriate, where the flux of any component depends

on the concentration gradient of all species. Van den Broeke and Krishna (1995) extended the Maxwell-Stefan multicomponent model to surface diffusion in the form

$$\mathbf{N}^s = \mathbf{D}^s \nabla \mathbf{n} = \left(\mathbf{B}^s\right)^{-1} \boldsymbol{\Gamma} \nabla \mathbf{n} \tag{5.23}$$

where $\mathbf{B}^s$ is the inverted matrix of surface mobilities. If there were a more complicated interaction between the surface adsorbed species then the form of Γ, the thermodynamic factor, would have to capture it.

The concentration dependence of a pure component, Γ, would be a function of the adsorption equilibria. Eq. 5.10 has been used to derive various loading dependent expressions for diffusivity. When the Langmuir equation is considered

$$\Gamma = \frac{1}{(1-\theta)} \tag{5.24}$$

with the Dubinin-Astakov equation it yields

$$\Gamma = \frac{\beta E}{RT} \frac{1}{m} \left(-\ln(\theta)\right)^{\frac{1}{m}-1} \tag{5.25}$$

The shape of the Γ calculated by eq. 5.12, versus θ using the correlation parameters for hexane on BPL is plotted for these two models in for these two models in Figure 5-1. The value of Γ varies from approximately 2 to 30 or approximately one order of magnitude for the DR case, and it varies from approximately unity to 50 for Langmuir over a loading range, θ, of 0 to 0.98. This behavior indicates that the Fickian surface

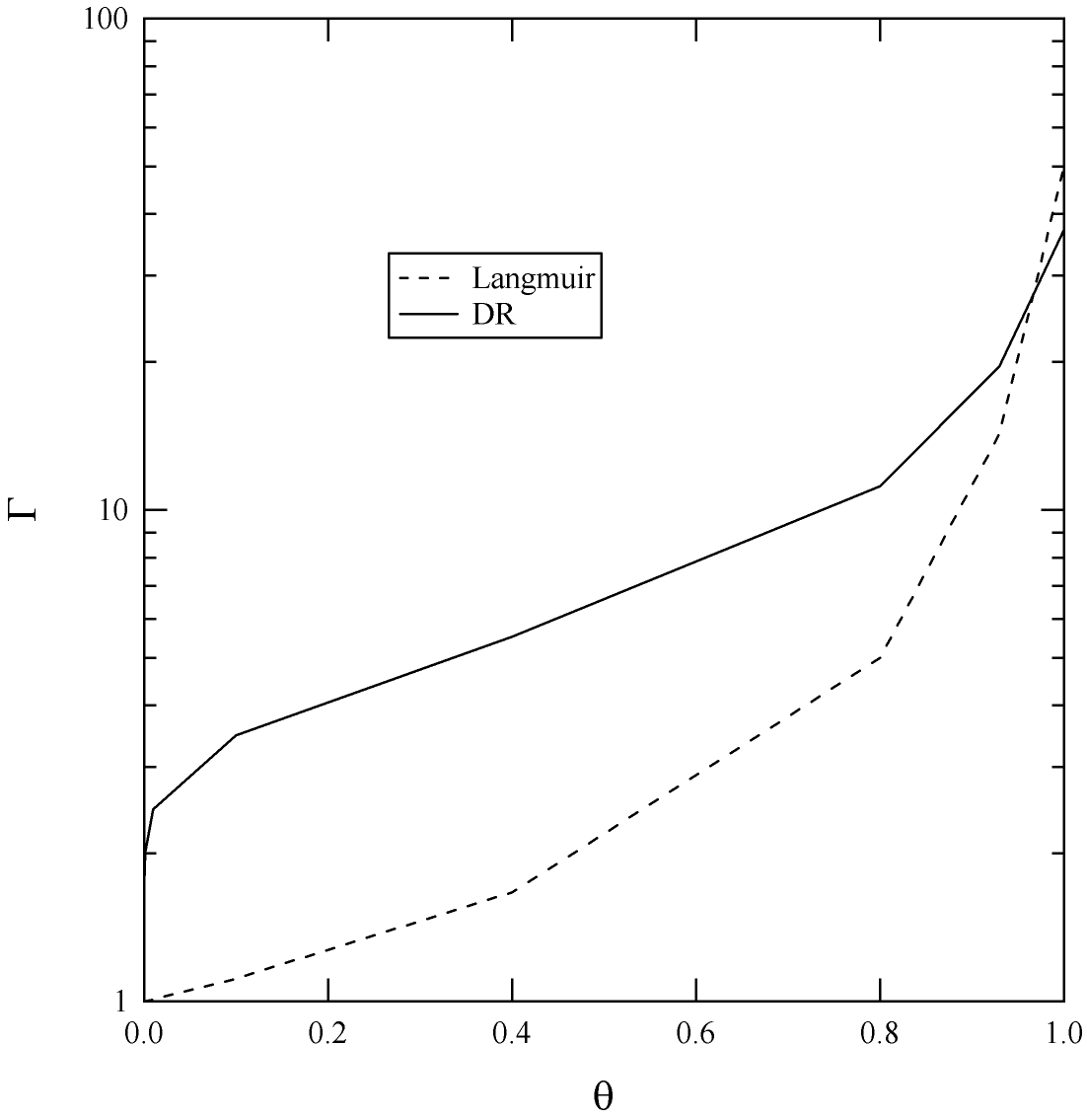

Figure 5-1The thermodynamic correction factor, eq. 5.21, calculated for the Langmuir and Dubinin-Raduschevich equations as a function fractional filling.

diffusivity should increase with loading which is expected when the adsorbed molecules are less strongly adsorbed at higher loadings.

It has been shown that the concentration dependence of diffusivities measured on zeolites and carbon molecular sieves is well correlated by the Darken relationship, such that the mobility is nearly constant with loading. The activation energy has been shown to be dependent on the molecular volume consistent with passage through a hindered opening. The concentration dependence of surface diffusivities has also been reported. A summary of surface diffusion data (Gilliland et al., 1974, Sladek et al., 1974) verifies that the activation energy for surface diffusion can be well correlated to the heat of adsorption, where it is assumed that the binding energy is the heat of adsorption. Recently Do, Do and Praseyto (2001) proposed a model for the surface diffusion on activated carbon based on a review of experimental results. The surface mobility was observed to increase with concentration more than predicted by the Darken relationship. They proposed a concentration activation term of the following form

$$D = D^{00}(T)\exp\left(\frac{E_0}{RT}\frac{\beta n_A}{1-\beta n_A}\right)\frac{\partial \ln p}{\partial \ln n_A} \tag{5.26}$$

Their explanation relates the loading activation energy to the heterogeneity of the surface. The temperature dependence of adsorption and chemisorption surface diffusivity was found to agree with the heat of adsorption correlations of Sladek et al. (1974). Their results were calculated by first subtracting Knudsen diffusion from the observed permeability.

The complete equation of continuity for the particle with surface diffusion is

$$\varepsilon_p \frac{\partial \bar{c}_A}{\partial t} + \rho_p \frac{\partial \bar{n}_A}{\partial t} = \nabla \cdot \left(\varepsilon_p D_p \nabla \bar{c}_A + \varepsilon_p \frac{R^2}{8\tau_v \mu} \bar{c}_A R_G T \nabla \bar{c}_A + \rho_p D \nabla \bar{n}_A \right) \tag{5.27}$$

where D represents either Fickian or Maxwell-Stefan diffusivity. The complete equation of continuity for the particle with microparticle diffusion is

$$\varepsilon_p \frac{\partial \bar{c}_A}{\partial t} + \rho_p \frac{\partial \bar{n}_A}{\partial t} = \nabla \cdot \left(\varepsilon_p D_p \nabla \bar{c}_A + \varepsilon_p \frac{R^2}{8\tau_v \mu} \bar{c}_A R_G T \nabla \bar{c}_A \right) + \nabla_\mu \cdot \rho_p D_\mu \nabla_\mu \tilde{n}_A \tag{5.28}$$

and the boundary condition is defined by the adsorption equilibria

$$n_\mu \Big|_{r=R_\mu} = f(\bar{c}_A) \tag{5.29}$$

and

$$\frac{\partial \bar{n}_A}{\partial t} = \frac{3}{R_\mu^3} \int_0^{R_\mu} \frac{\partial \tilde{n}}{\partial t} r^2 dr \tag{5.30}$$

An energy balance written for the particle takes the following form based on distributed parameter approach

$$\frac{\partial}{\partial t}\left[U_s + U_f - \lambda n\right] = k\nabla^2 c \tag{5.31}$$

the boundary condition

$$k\frac{\partial T}{\partial r} = h_a(T - T^*) \tag{5.32}$$

similarly a lumped parameter model for the energy balance can be written as

$$\frac{\partial T}{\partial t} = \frac{\lambda \frac{\partial n}{\partial t}}{c_{ps} m + n c_{ps}} \tag{5.33}$$

A distributed parameter model for particle scale effects is difficult to justify if the adsorbent particle is granular. Pore diffusion occurs in macropores, which are of the length of the particle. Surface diffusion occurs in the micropores where the characteristic dimension for surface diffusion should be the microparticle radius and not the pellet radius. In heterogeneous adsorbents it may be difficult to characterize the microparticle diameter leaving the group D_s / R_{mp}^2 as the parameter that characterizes the system. These two rates are considered to act in parallel with no accumulation in the pores of the

adsorbent. In the absence of external film resistance and where micropore diffusion is controlling this approach does not result in any particle size dependence. For the case where pore diffusion does contribute to the overall resistance there is something other than a R_P^2 rate dependence.

There is a conceptual difficulty with application of a surface diffusion model where vapor and adsorbed phases coexist in the same pore domain. The assumption must be made that the vapor and solid are everywhere in equilibrium or the chain rule must be invoked to relate the phases. Using a combined film resistance, pore and surface diffusion model, eq. 5.1-5.11 and 5.32-5.33, the boundary condition must be written in the vapor phase concentration yet the equilibria relationship must be applied to describe a loading dependence. One way to introduce the adsorption equilibria would be to implement and isotherm derivative as follows

$$\frac{\partial n}{\partial t} = D_g \nabla^2 c \tag{5.34}$$

$$k_v\left(c - c^*\right) = D_g \frac{\partial}{\partial r} c \qquad at \quad r = 1 \tag{5.35}$$

$$\frac{\partial n}{\partial t} = D_g \frac{\partial c}{\partial n} \nabla^2 n \tag{5.36}$$

$$D_s = D_g \frac{\partial c}{\partial n} \tag{5.37}$$

Eq. 5.38 suggests that a simple relationship exists between the vapor phase diffusivity and surface diffusivity. However the slope of the isotherm must be evaluated and its value can vary by 5 orders of magnitude as seen in Figure 5-2, which presents the isotherm slope for hexane using the Langmuir and DR equation. This can lead to numerical solution difficulties as well a not being accurate description of the observed

uptake data which shows rapid uptake even at low loadings. Solution to the above approach does not correctly relate the vapor and adsorbed phase concentrations. The only model that correctly captures the difference between adsorption and desorption profiles expresses vapor and adsorbed phase equilibrium directly through a boundary condition, not as in eq. 5.35.

A bidisperse, distributed parameter macropore, micropore diffusion equation can be solved using orthogonal collocation (Finlayson, 1980). Jacobi polynomials are evaluated and the boundary conditions were solved numerically with the resulting boundary concentration and temperature substituted in the collocation matrix where the collocation matrices are written in the form

$$\frac{dy}{dx} = \overline{\overline{\mathbf{A}}}y \qquad\qquad \nabla^2 y = \overline{\overline{B}}y \tag{5.38}$$

The collocation solution to an imbedded derivative, such as occurs with a loading dependent diffusivity in the pore diffusion equation, can be obtained as follows

$$\nabla^2\left[f(y)y\right] = f(y)\overline{\overline{B}}y + \left(\overline{\overline{A}}y\right)^2 \frac{d\left[f(y)\right]}{dy} \tag{5.39}$$

One difficulty in the application of this method is that the function f in the above equation corresponds to the slope of the isotherm in the diffusion equation. The second derivative of the slope of the isotherm does not have any obvious physical significance. In addition the solution for the second derivative becomes undefined for a highly favorable adsorption equilibria model such as the DR equation, which leads to the choice of implementing a constant micropore diffusivity parameter.

Recently Choi (2001) presented a review of many of the surface transport models. Several theories have been proposed for surface diffusion relying on the concept of

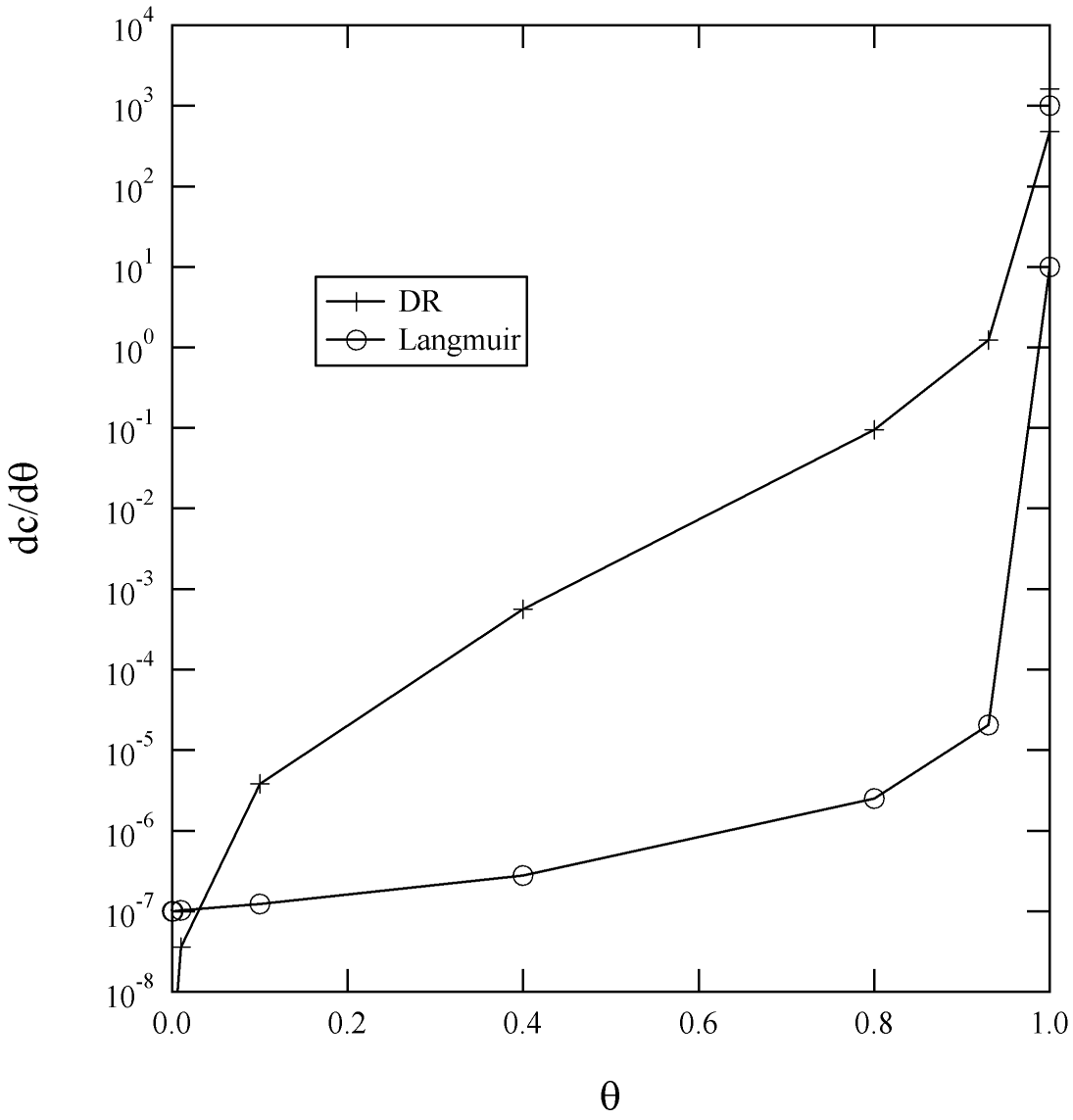

Figure 5-2 Derivative of the adsorption isotherm with respect to fractional loading versus fractional loading.

adsorbed molecules moving from site to site with the rate related to the heat of adsorption. Malek and Farooq (1997) studied adsorption rates of several light hydrocarbons on activated carbon and silica gel. They employed a single linear driving force model based on the adsorbed phase to study the dynamics of breakthrough behavior. An overall rate coefficient was determined from which surface diffusion coefficients were obtained. However the model that they postulated may not have employed the appropriate driving force expression for more strongly adsorbed species. The gas phase transport should be governed by a gas phase driving force while they assumed that the solid phase driving force was adequate for all resistances. Their assumption would be valid for the case of near linear adsorption equilibria. However for highly favorable equilibria the vapor phase equilibrium concentration can be nearly zero. This would lead to a linear uptake rate. Therefore in simulating the shape of the uptake profile the two different uptake mechanisms would predict different shapes to the uptake curve. Their reported diffusivities are consistent with those found in the uptake results. They found that the effective diffusivity on activated carbon is less than the Knudsen diffusivity while for silica gel the diffusivity is governed by Knudsen diffusivity. An apparent diffusivity for porous pellets can be measured using a Wilke-Kallenbach method. However the observed rate will result from the fastest of the several combined rates acting in parallel. Data, obtained using this method (Guo et al., 1998), for several light hydrocarbons on 13X molecular sieve pellets indicated that macropore transport was dominant as would be expected for a highly porous adsorbent. However it is known that micropore diffusion does occur into the crystals, but that rate is masked at steady state. Large interconnecting macropores allow rapid transport throughout the particle.

Kapoor and Yang (1991) studied the uptake rates of hexane on BPL carbon from a helium carrier. The model included both gas phase and adsorbed phase fluxes. They concluded that surface diffusion provided a significant contribution in addition to Knudsen diffusion. The pore diffusion model of Kapoor and Yang was discussed in comparison for adsorption of hexane on BPL carbon. They presented a simulation of desorption data using the model but did not present modeling results for desorption. The time scale for adsorption data to reach equilibrium was approximately 1000 s in their results. Their analysis only considered uptake at later times ignoring the initial part of the profile. They did not consider non-isothermal effects but did consider the temperature effect on diffusivity. Using a constant surface diffusivity and assuming the vapor diffusion is governed by Knudsen diffusion they found a zero loading surface diffusion coefficient of 2.2×10^{-4} cm^2/s at 298 K. The magnitude of this diffusion coefficient is greater than the corresponding liquid phase diffusivity of hexane, even though the enthalpy of adsorption is greater than the enthalpy of vaporization.

Hu et al. (1994) reported experimental diffusivity results based on a differential bed approach. Their model was derived using a thermodynamic factor based on the adsorption equilibria expression. The zero loading diffusivities obtained for an Ajax activated carbon 4×10^{-5} cm^2/s for propane at 303 K. Rutherford and Do (2000) described a permeation time lag method for transport measurements. They examined carbon dioxide on Carbolac activated carbon. Earlier uptake experiments were analyzed by Kodama (1992) and analyzed using either pore diffusion and surface diffusion model with constant diffusivities. They showed that similar fit could be obtained using either model. A combined model was not discussed. They also included a mass transfer term for

the film resistance. A constant surface diffusivity reported for refrigerant R-113 was approximately $4x10^{-6}$ cm^2/s on an activated carbon. They evaluated two parameter fits to determine the diffusivity and Sherwood number for data obtained using a well mixed stirred tank. The equilibria were described by the Langmuir isotherm. The Sherwood number was determined to be 0.86, which was less than 2.0 due to the use of more than one particle in the basket. Zhu et al. used the uptake approach (2004) to determine surface diffusivities for butane and isobutene on activated carbon from desorption data. They found good agreement using a structure dependent diffusivity, which is the inverse of the isotherm slope as opposed to the Darken equation which the inverse slope in logarithmic coordinates. No mention was made in that work of measurement of vapor phase concentration profiles, also the particle radius considered was small 0.17 mm. Ding and Bhatia (2003) employed a micropore Maxwell-Stefan formulation to describe the multicomponent uptake kinetics of ethane and propane on two activated carbons,

Sward (2003) determined that surface diffusion was rate controlling for microporous carbon by frequency response. He measured a diffusivity of $4.7x10^{-3}$ cm^2/s for CO_2 on 6x16 mesh BPL carbon and noted that the diffusivity did not vary with the radius to the second power. This concept would be consistent with internal geometry being more important than particle diameter.

Do et al. (2001) determined the hexane transport properties on activated carbon by a permeation technique. They applied the Darken relationship which resulted in a loading dependent surface diffusivity which varied from zero coverage to a loading corresponding the hexane partial pressure of this experiment, 6000 Pa, from 4×10^{-8} to 2×10^{-6} cm^2/s.

In order to consider the application of the transport models for vapor phase adsorption to a microporous adsorbent a series of experiments were conducted using gravimetric uptake of a strongly and moderately adsorbed vapor on activated carbon and molecular sieve. The results are analyzed using the particle transport models. Analysis of the measured intraparticle rate data in terms of particle and microparticle length scale, should provide some indication of basis for the variations of literature values of diffusivity. It should be apparent with this analysis how for future investigations a more consistent approach to reporting diffusivity values can be established.

5.3 Experimental Methods

A gravimetric apparatus has been constructed to measure adsorption uptake rates. The system is designed to introduce a metered flow of carrier to an adsorbent sample with controlled concentration and temperature conditions. A system schematic is presented in Figure 5-3. The sample basket containing the adsorbent sample is suspended with a hang-down wire from a Cahn model D-200 vacuum microbalance. The flowrate of the carrier gas, either air or helium, is controlled using two mass flow controllers. One of these flow streams serves as a source of clean carrier. The other metered flow stream is directed to a glass U-tube type, liquid filled sparger cell. A series of two 4-way switching valves is used to select the bed exposure state. The bypass 4-way valve allows flow to pass over the sample or to place the sample in an isolated state. The purge 4-way valve selects whether clean purge or sparger flow is directed to the basket. The sample basket is contained in a thermostatted vessel constructed of Pyrex, which allows temperature-conditioning of the flow.

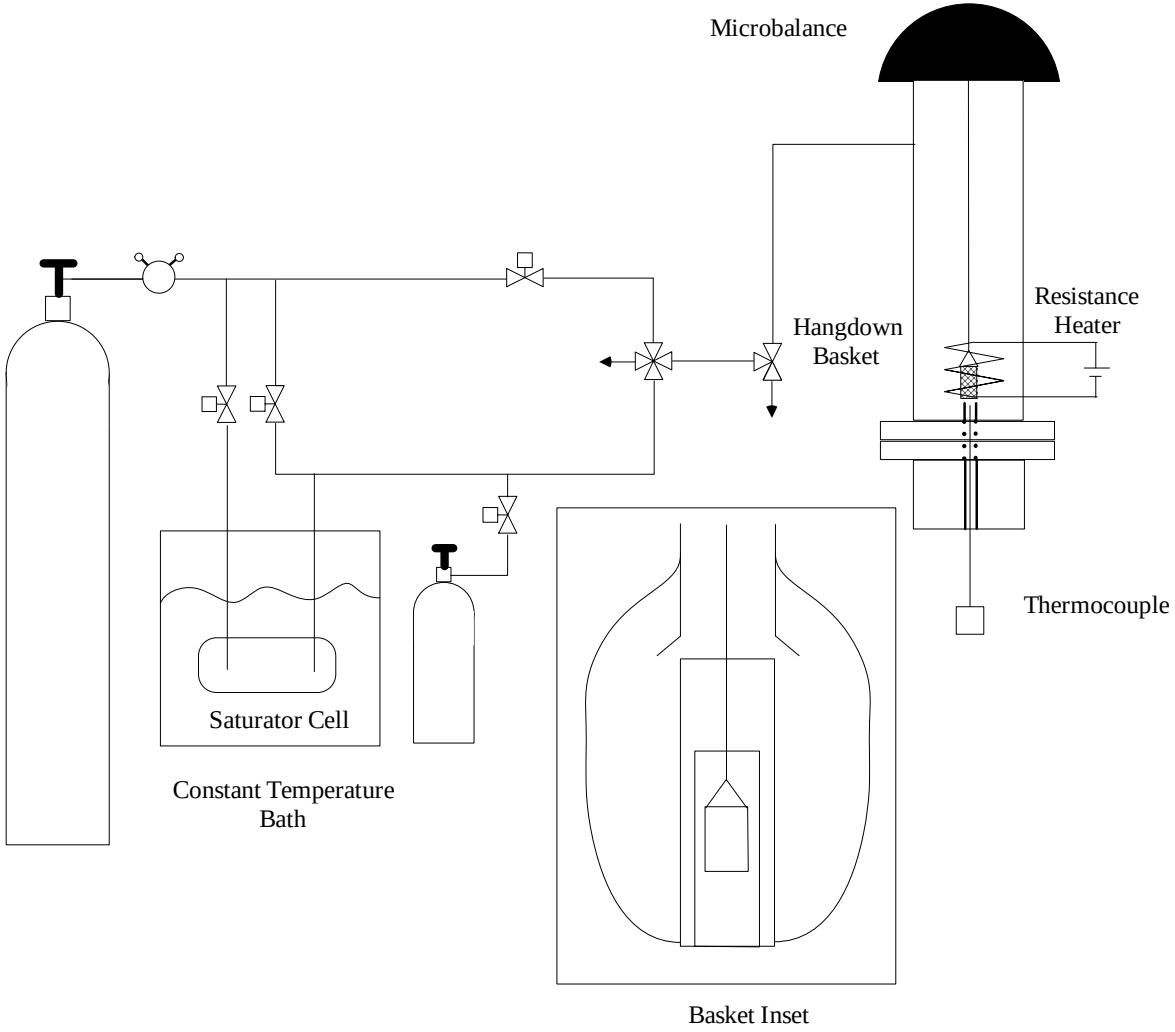

Figure 5-3. Schematic of gravimetric adsorption apparatus.

The sample basket is suspended in a funnel and tube arrangement Figure 5-4. The incoming carrier stream is vented over the basket in a small exposure chamber. The exposure area contains a length of Ni/Cr wire wrapped around a quartz tube, a resistance heater for high temperature purging of the adsorbent sample prior to the chemical challenge experiment. Flow exits the chamber below the basket through a discharge tube with an outer diameter equivalent to the basket diameter of 0.8 cm and an inner diameter of 0.4 cm. A thermocouple is run through the discharge tube such that the tip of the thermocouple is located at the base of the basket.

The experiment started by establishing carrier flow over the basket with adsorbent particles followed by heating to 423 K for 20 minutes, then cooling to the equilibrium temperature. The weight or the clean sample was established by placing the sample in bypass mode. The bypass valve was then switched to allow clean carrier flow to the sample causing a drag on the sample. The second stream was then introduced to the chemical equilibration cell, while the temperature is allowed to return to the setpoint for the test. By then switching the purge valve the sparger flow at the same drag condition was introduced to the sample and the uptake response recorded. System operation was automated to perform both challenge and desorption steps and data logging. On desorption the clean carrier was re-directed to the sample through the purge line. The sampling rate could be selected as 1 or 5 s. Sample carryover was minimized by the use of PEEK transfer tubing. Typically sample size is restricted to 5-30 mg in order to obtain single particle or monolayer coverage in the exposure basket.

Two feed chemicals were considered in these experiments, hexane and chloroethane. The hexane concentration was obtained by passing the carrier through an

evaporator cell maintained in a constant temperature bath. Chloroethane was metered into the carrier flow as a gas. The chemical concentration was measured by pulling a stream of 30 sccm continuously to a flame ionization detector. Tubing, 1/16 inch OD, was used to connect a diaphragm pump between the gravimetric system and the GC with FID.

5.4 Results

5.4.1 Uptake Behavior

In order to clarify the transport mechanisms that influence vapor phase adsorption, measured uptake data has been obtained from a series of experiments using the gravimetric adsorption apparatus. This technique provides a convenient method to observe particle scale transport. The method is similar to that employed by Kapoor and Yang (1991). At the start of the experiment the adsorbent sample is conditioned at an elevated temperature of approximately 423 K, with carrier flow. The temperature is then reduced to the temperature of the run, typically 298 K, and the sample weight allowed to stabilize. The chemical challenge is then introduced. Uptake is observed corresponding to adsorption from the vapor phase until equilibration is achieved. After the temperature and loading have stabilized at this new condition the desorption step is begun by switching to clean carrier flow. The desorption profile typically requires a much longer time, asymptotically approaching complete cleanup.

The response from the microbalance and the temperature measurement from the base of the basket were recorded. A typical transient response for the measured weight is plotted versus time as shown in Figure 5-4. In the figure the time scale is adjusted so that the start of the challenge step corresponds to time zero. The adsorbent is allowed to reach

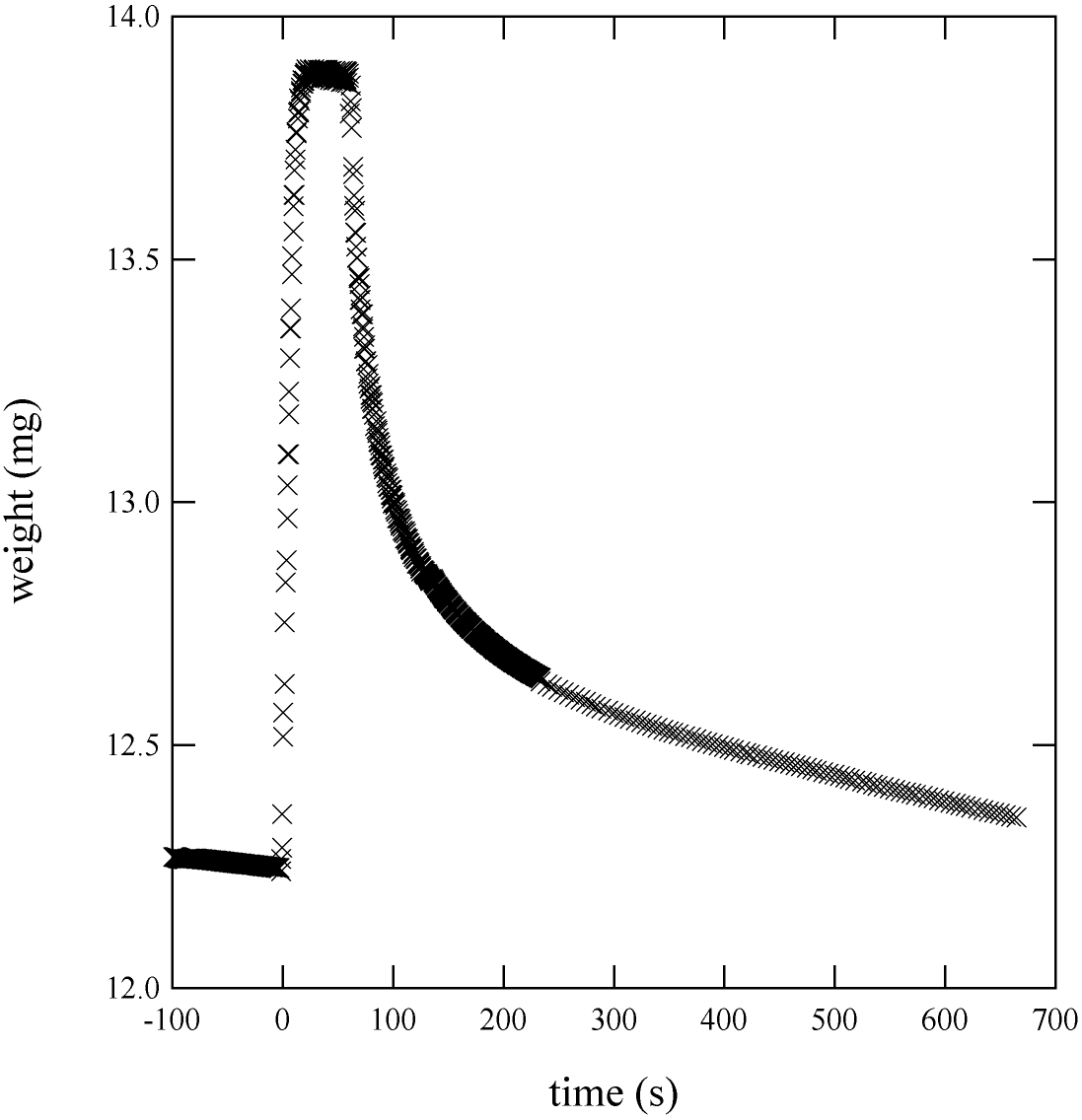

Figure 5-4. Gravimetric response profile for adsorption followed by desorption experiment of hexane on BPL carbon with helium carrier (Run 1 conditions).

adsorption equilibrium at the feed conditions, prior to the desorption step, where clean carrier is directed to the sample at the feed temperature and weight loss is observed. It is instructive to consider both the uptake and desorption profiles on a common plot. One approach to achieve this is to represent both steps on normalized coordinates such that at the start of each step the ordinate is unity and over the course of the step the ordinate value tends to zero. If a reduced loading is defined in terms of n/n_{feed} then the ordinate for the adsorption step must utilize the following transformation $1-n/n_{feed}$.

Several aspects of the operation of the gravimetric system affect the observed uptake response. The rate of chemical feed delivery during the adsorption step must be fast enough to maintain uniform concentration over the adsorbent. Calculations for a typical set of conditions indicate that the feed chemical delivery rate of hexane and chloroethane during the uptake experiment is 0.2 g/m, which is approximately 20 times greater than the observed uptake rate as recorded by the microbalance. The dead volume of the tubing and balance upstream of the adsorbent basket was approximately 100 cm^3, which for a flowrate of 2 slpm corresponds to approximately 3-second residence time. The sampling rate during the experiment is conducted at 3 Hz by the data acquisition system. However the microbalance performs an internal 1 s integration, which then becomes the limit of time resolution. The apparatus then can easily characterize rate processes which occur over 2 seconds and longer. The weight measurements by the microbalance have a resolution of 0.01 mg with a range of 100 mg.

The selection of the total flowrate and velocity at the sample basket must be optimized. As mentioned above the chemical delivery rate must be large relative to the particle uptake rate. Similarly the velocity of the carrier should be large to reduce film

mass transfer resistance. However the maximum flowrate is limited by the momentum of the flowing gas on the stability of the weighing basket. It is observed that the recorded weight changes from stable to unstable with increasing carrier flowrate, i.e. a harmonic in the recorded weight. Also the flowrate should be minimized in order to limit the consumption of chemical and carrier gas in the case of helium, where both air and helium were evaluated as carrier gases. In order to minimize chemical consumption the low mass flow rate with small void volume approach was utilized.

A pressure drop is generated at two places, which can provide a force to disturb the basket. In order to obtain an increased velocity at the basket, the discharge tube, 0.4 cm ID is located below the basket. Also as the feed gas flows through the heat exchange system it empties through tubing with 0.4 cm ID into the 2.0 cm ID tubing through which the hand-down wire is run. There is a pressure drop associated with these velocity changes. The force associated with this expansion can be calculated using the equation of continuity

$$\Delta p = \frac{\rho v_2^{\,2}}{2}\left(1-\left(\frac{D_2}{D_1}\right)^2\right) \tag{5.40}$$

The sum of the interior and exterior area of the basket 1.7 cm long and 0.75 cm OD corresponds to an area of 8.9 cm^2. The calculated pressure force multiplied by basket area divided by the basket weight is well correlated to the balance stability under flowing conditions. Calculated values for this ratio for a series of flow and carrier gas conditions are presented in Table 5.1. The measured weight becomes unstable as the force exerted by the flow expansion on the hang down wire and basket approaches the weight of the basket. Some physical properties of the gases are listed in Table 5.2. The results indicate

Table 5.1. Flow Behavior of Gravimetric Adsorption System

carrier	Flowrate (slpm)	stability	(ΔPxA) (dyn)* (eqn 5.10)	(ΔPxA)/(basket wt)** (%)
air	1	stable	177	3
air	2	unstable	710	12
helium	2.84	stable	204	3
helium	4.26	transition	460	8
helium	5.68	unstable	820	14

* heat exchange tube and discharge tube ID 0.6 cm, hang down column ID 2 cm
** basket weight 0.75 g, area 8.9 cm^2

Table 5.2. Properties of selected gases and adsorbents.

ρ (g/cm^3)	1.6×10^{-4}	Helium
ρ (g/cm^3)	1.1×10^{-3}	air
k (W/cm/K)	1.5×10^{-3}	helium
k (W/cm/K)	2.6×10^{-4}	air
D_m (cm^2/s)	0.08	hexane-air
D_m (cm^2/s)	0.316	hexane-helium
C_s (kJ/kg/K)	1.25	heat capacity of carbon

that the use of helium as a carrier gas maintains basket stability a higher volumetric flowrate and corresponding velocity than air. Measurements of adsorption and desorption were conducted using helium at up to 2.84 slpm in order to obtain stable readings. For the case of a pressure change resulting from a small flow change there is a corresponding change in the recorded weight at the next measured data point suggesting that there is no apparent averaging in the balance response.

A summary of the experimental runs is provided in Table 5.3. The carrier gas flowrate, adsorbent, feed chemical, and measured loading are listed. Most of the data was obtained using activated carbon. In order to minimize the effect of chemical delivery the adsorbent samples were generally kept small. In some cases single particle experiments were conducted. Two adsorbents were considered, BPL activated carbon (Calgon Corp.) and zeolite molecular sieves (UOP 13X grade PSA/O2 minibeads). The use of helium as the carrier resulted in no co-adsorption effects.

Adsorption and desorption trials conducted with hexane as the adsorbing chemical have been plotted for several cases of adsorption on BPL carbon. The results for uptake behavior with two vapor phase concentrations of hexane are presented in Figure 5-5. The feed stream was equilibrated with hexane at the partial pressure corresponding to the saturation vapor pressure at 275 and 293 K. The significant enhancement in uptake associated with the higher concentration indicates a strong influence of film mass transfer resistance. Similarly the effect of velocity, particle size and temperature on uptake rate can be seen in Figure 5-6. In the apparatus it is difficult to assign a velocity because the different diameters of the hang-down tube and the discharge tube, therefore a average velocity is calculated based on the geometric mean of these two diameters. A velocity

Table 5.3 Summary of Gravimetric Experimental Conditions at 298 K.

Run No.	Adsorbent	Chemical	Particle diameter (mm)	Shape factor	Carrier gas	Temp. (K)	Velocity* (cm/s)	P_i (Pa)
1	BPL	hexane	1.0	0.43	helium	298	40	6700
2	BPL	hexane	1.5	0.43	helium	298	27	6700
3	BPL	hexane	1.5	0.43	helium	298	27	16161
4	BPL	hexane	1.5	0.43	helium	298	40	6700
5	BPL	hexane	1.5	0.43	helium	308	40	6700
6	BPL	hexane	1.5	0.43	air	298	19	6700
7	BPL	chloroethane	1.0	0.43	helium	298	54	1070
8	13X	hexane	1.0	1.0	helium	298	54	6700
9	13X	chloroethane	1.0	1.0	helium	298	54	1070
10	BPL	hexane	1.0	0.43	helium	298	54	6700

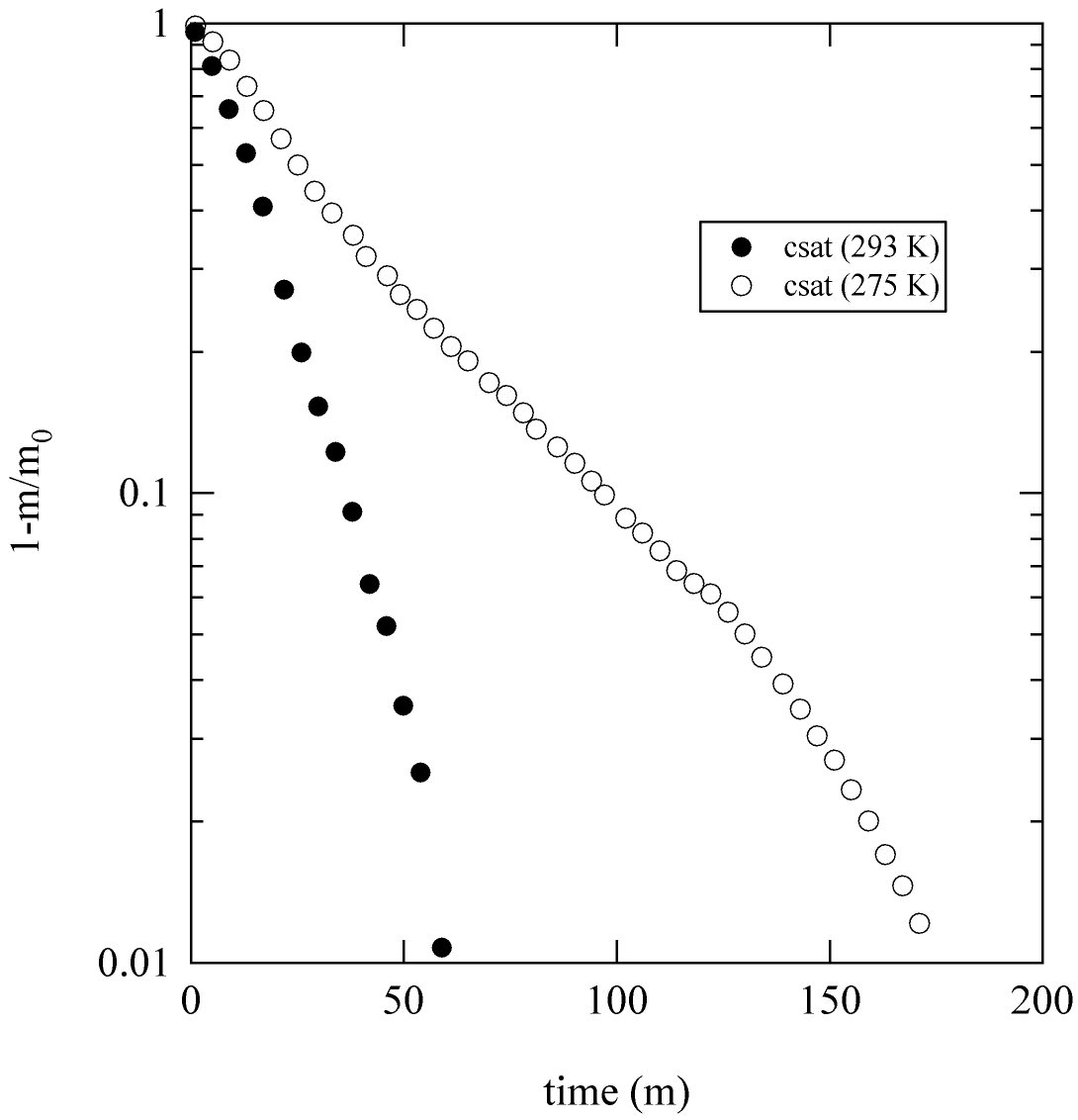

Figure 5-5 Uptake rate recorded for hexane on BPL carbon with helium carrier at two sparger temperatures, 275 and 293 K. Carrier flowrate 1 slpm, particle diameter 0.14 cm (Runs 2 and 3).

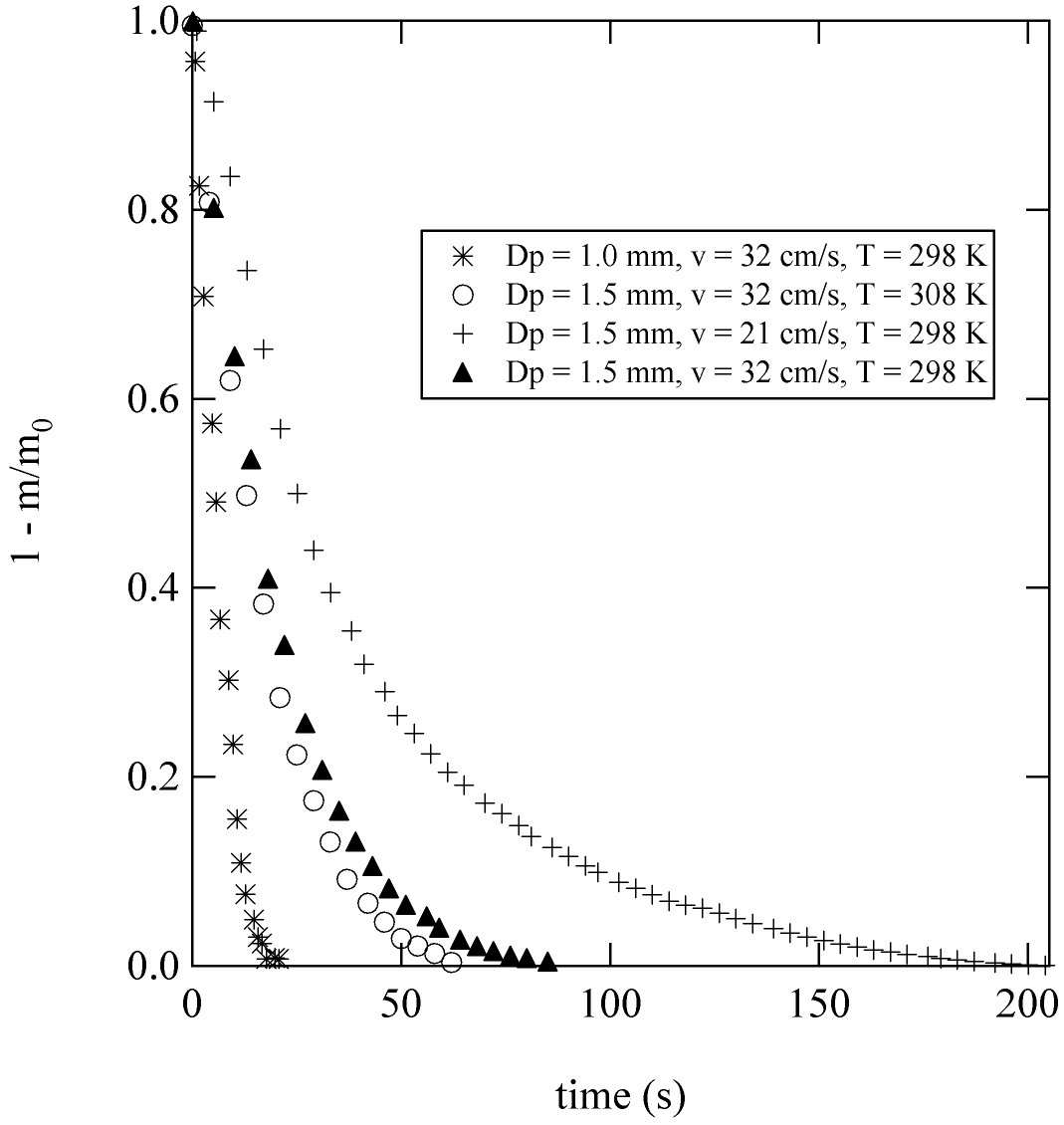

Figure 5-6 Adsorption profiles of hexane on single particles of BPL carbon measured with helium carrier for various particle sizes, velocities and temperatures (Run 2, 3-5).

dependence on the uptake is consistent with external film resistance. Results comparing the profiles for desorption are plotted in Figure 5-7. The rate for desorption is longer by an order of magnitude than the rate recorded for adsorption. Again this is consistent with the influence of external mass transfer, because the internal controlled rate is governed by loading thus adsorption and desorption rates should be nearly identical in the absence of film resistance. Also the effect of particle size is evident. The maximum response of the temperature probe for both adsorption and desorption were approximately 275 K. This temperature is measured in the flowing gas stream and no attempt was made to assure adiabatic behavior.

Most of the runs were conducted without measuring the feed concentration. Later in the testing a continuous concentration measurement was performed. Figure 5-8 shows the concentration response, measured weight, and the corresponding signal switching time for the valve where non-adsorbing glass beads are placed in the weighing basket. Three separate concentration-sampling locations were evaluated: after the four-way valve, after the 3-way valve and at the sample exit line. It can be seen that in each case a 23 second delay occurred in the concentration response. The concentration is sampled just below the weighing basket by running the sampling line up into the exit line of the apparatus. Upon switching the chemical flow to the bed the rise in concentration is sharp reaching the feed value in approximately 10 seconds. Therefore the adsorption step rate data is modeled using a step change profile. A similar response is noted during the desorption step as clean carrier gas is introduced to the system. For the desorption case

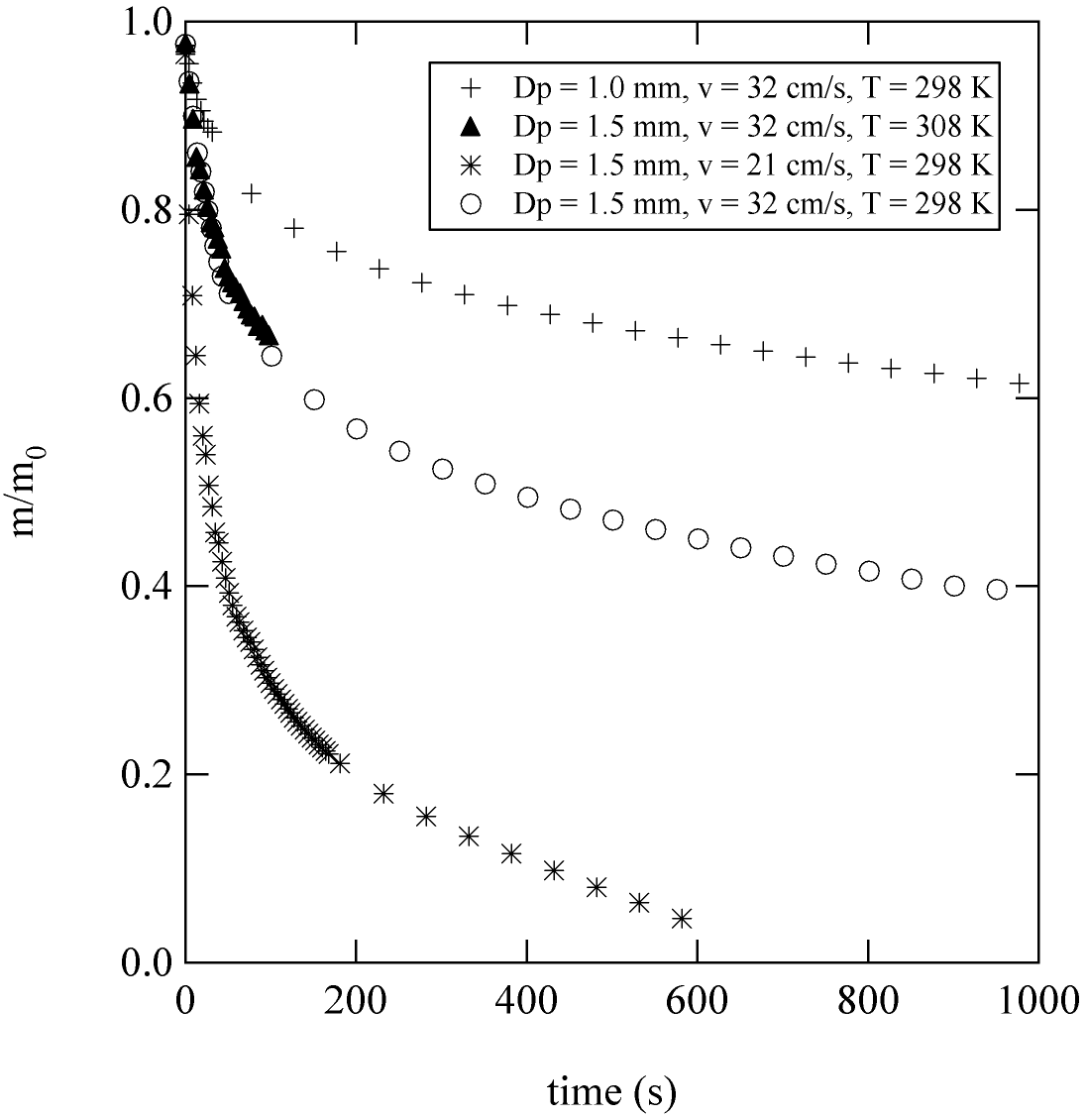

Figure 5-7 Desorption profiles of hexane on single particles of BPL carbon measured with helium carrier for various particle sizes, velocities and temperatures (Run 2,3-5).

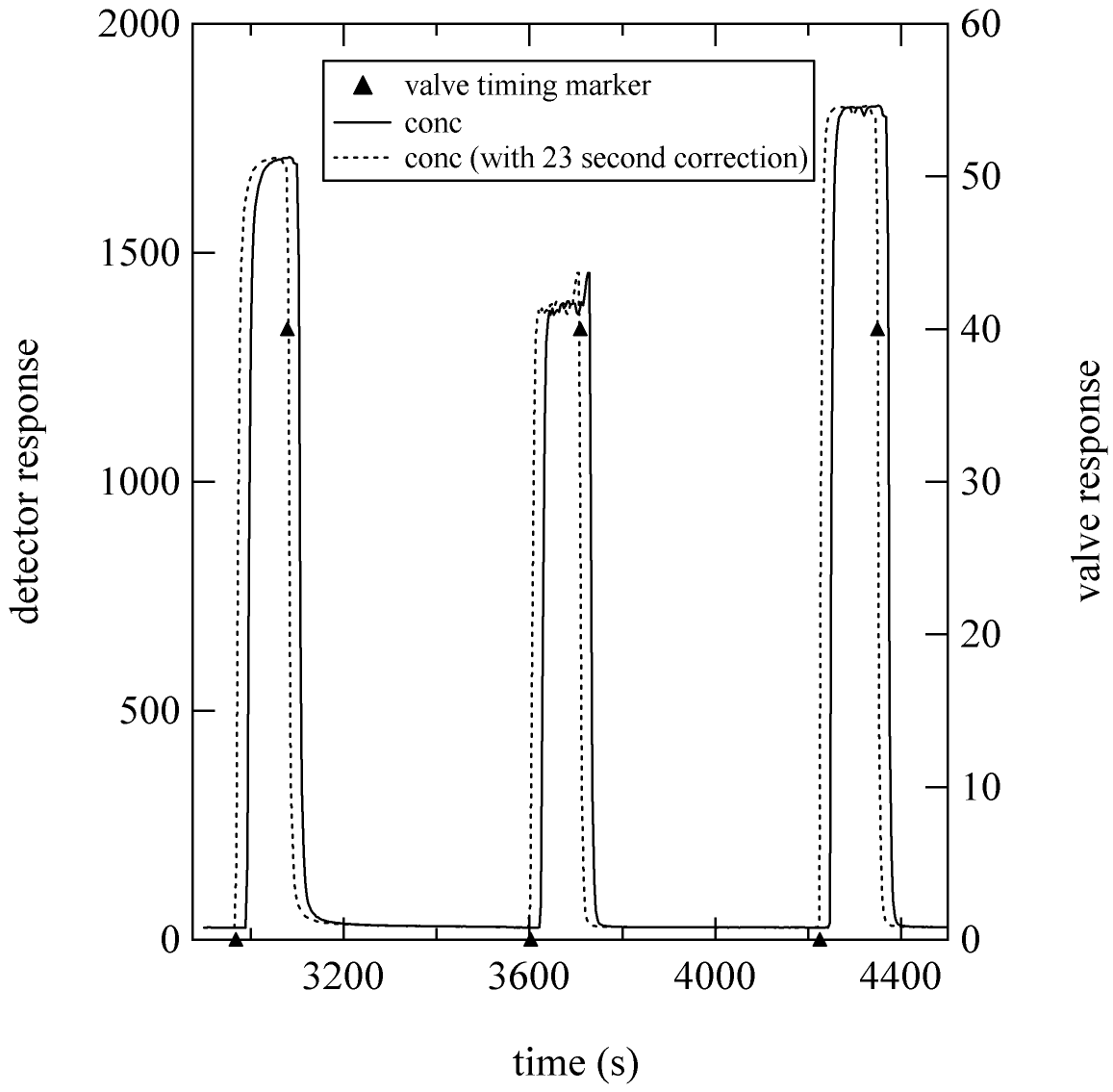

Figure 5-8 Measured uptake system outlet concentration profile and concentration profile with 23 s correction.

the concentration does not completely return to the initial concentration. For the case of the glass beads and the adsorbent a tail is observed due to a trace concentration contamination of the feed lines.

It can be shown that the effect of sample size on the uptake rate is not significant. Two experiments conducted with 4.5 and 13.6 mg tare samples using chloroethane on BPL carbon with identical feed concentrations are plotted in Figure 5-9. The loading range from 0.12 to 0.28 g/g is normalized from 0 to 1. The uptake curves are in close agreement in this case. Here it is assumed that the initial rate has been ignored because of the lag in delivering the highest feed concentration until a few seconds into the challenge step.

5.5 Modeling of Results

There is an uncertainty associated with the particle dimension of granular adsorbents. The characteristic dimension is determined as an average obtained by a passing the sample through a series of screens. The non-spherical character of granular material is best described through the use of a shape factor, ϕ, where the effective mean particle diameter is defined as

$$D_{p_m} = \phi D_p \tag{5.41}$$

A reported value of the shape factor of coal dust is 0.73, and sand is 0.75 (Geankoplis 1983, p. 133). The former value is used here for granular activated carbon.

The gravimetric method cannot be performed at a high Reynolds number and thus cannot yield a high film transfer rate, so that internal rates cannot be isolated. The model must include film mass transfer effects. The Sherwood number was calculated using single particle correlation, eq. 5.4. Similarly the Nusselt number was calculated using eq. 5.5.

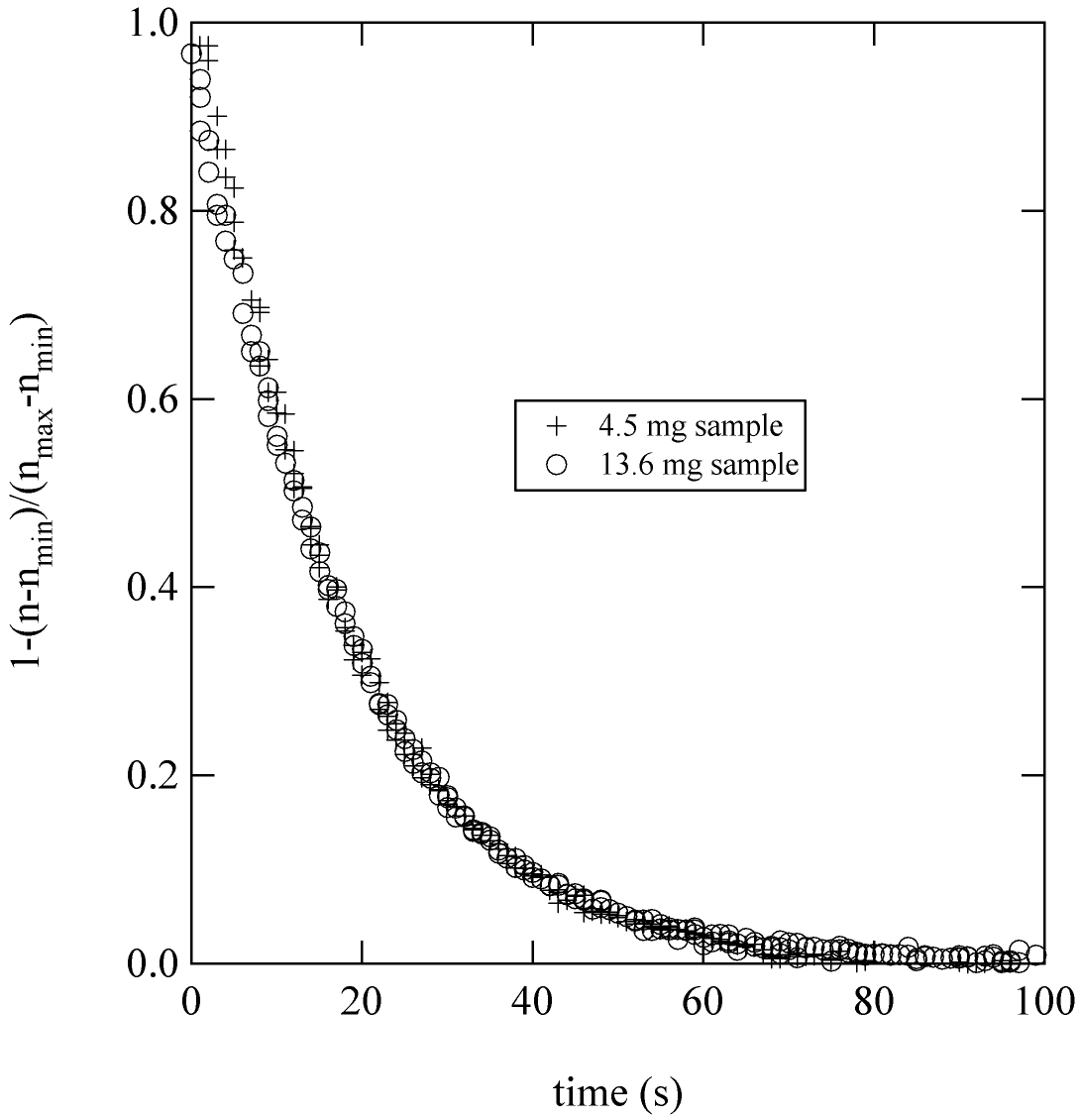

Figure 5-9. Normalized uptake of chloroethane on BPL carbon with two sample sizes.

For the conditions of experiment 1 in Table 5.3, using helium as the carrier the binary diffusivity of chloroethane is greater than with air, 0.32 versus 0.08 cm^2/s, the corresponding N_{Sh} and N_{Nu} numbers were 3.2 and 2.6. These were calculated using the average velocity discussed above. Most experiments were performed at flow conditions corresponding to an exit tube throat velocity of 32 cm/s.

The measured uptake response curves were used to determine the mass transfer rate parameters. The output of the simulation model was reported in terms of concentration and loading which was then cast in the dimensionless loading parameter used to display adsorption and desorption on a common plot. A regression algorithm was implemented to determine the values of various model parameters in a least squares sense. Typically only a single parameter, the microparticle diffusion coefficient, was regressed. An objective function was evaluated based on the sum over all the adsorption and desorption points of the difference in area under the transient profiles for the model and data. The simulation and regression were implemented in MATLAB.

The experimental observation of the carrier phase temperature transient justified a non-isothermal model. A distributed parameter particle heat balance was used with a distributed parameter particle diffusion model, with no temperature distribution implemented in the microparticle. When no particle heat transfer behavior is simulated, on adsorption a predicted temperature rise of up to 55 K results, while on desorption the temperature drop is only 15 K. The film resistance model alone whether isothermal or

non-isothermal cannot describe the measured data. It predicts too rapid an uptake and desorption.

A tortuosity factor of 4 is taken for all adsorbents considered here (Ruthven, 1984). For BPL carbon modeled as a bidisperse adsorbent with macropore radius of 1 μm, the Knudsen diffusivity is 3 cm^2/s versus D_m of 0.03 cm^2/s. The viscous term gives an equivalent diffusivity of 1.5 cm^2/s. A pore and microparticle diffusion model without film resistance predicts that both the uptake and desorption profiles when plotted as m/mo and 1-m/mo would be coincident, which is not observed experimentally. Both pore diffusion and viscous diffusion when solved with the film model result in simulations that are too fast to account for observed uptake. A solution based on combined film, pore and microparticle diffusion model, eq. 5.1-5.3, 5.11, 5.14 and 5.28-5.33, was obtained using the orthogonal collocation method with 12 collocation points for the pellet and 7 collocation points for the microparticle. The adsorption equilibrium correlation parameters for each adsorbent-adsorbate pair are listed in Table 5.4.

The minimization of the residual between the simulation and chloroethane adsorption and desorption data in helium carrier is shown in Figure 5-10. Also represented in Figure 5-10 are the predicted concentration profiles for the adsorption and desorption steps. There are only slight differences between the shape of the measured data and the simulation profiles. The constant dimensionless microparticle diffusion coefficient for chloroethane on BPL carbon is 6.0×10^{-3} s^{-1}. The results for hexane and 13X are presented in Figure 5-11. The adsorption on 13X is more favorable and therefore desorption is more difficult to model. Table 5.5 summarizes the micropore diffusivities obtained from several of the runs described in Table 5.3.

Table 5.4. Adsorption equilibria DR correlation parameters.

Adsorbate	Adsorbent	W_o (cm^3/kg)	$\beta E/R$ (K)	n
Chloroethane	BPL	477	1764	2
Chloroethane	13X	213	3692	2
Hexane	BPL	477	2860	2
Hexane	13X	213	6695	2

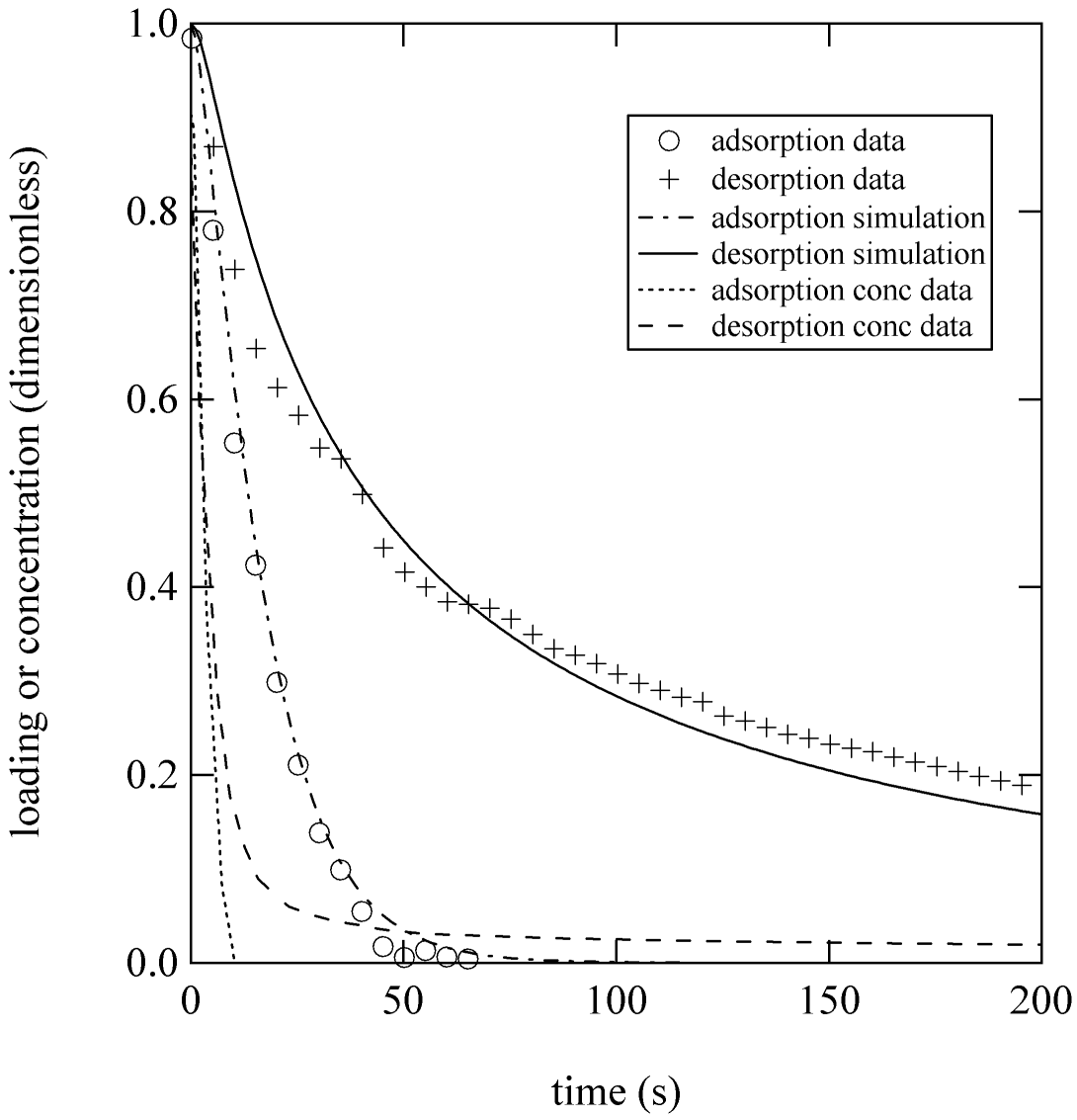

Figure 5-10 Chloroethane adsorption and desorption on BPL carbon granules at 298 K (Run 7), with non-isothermal microparticle scale model, eq. 5.1-5.3, 5.11, 5.14 and 5.28-5.33.

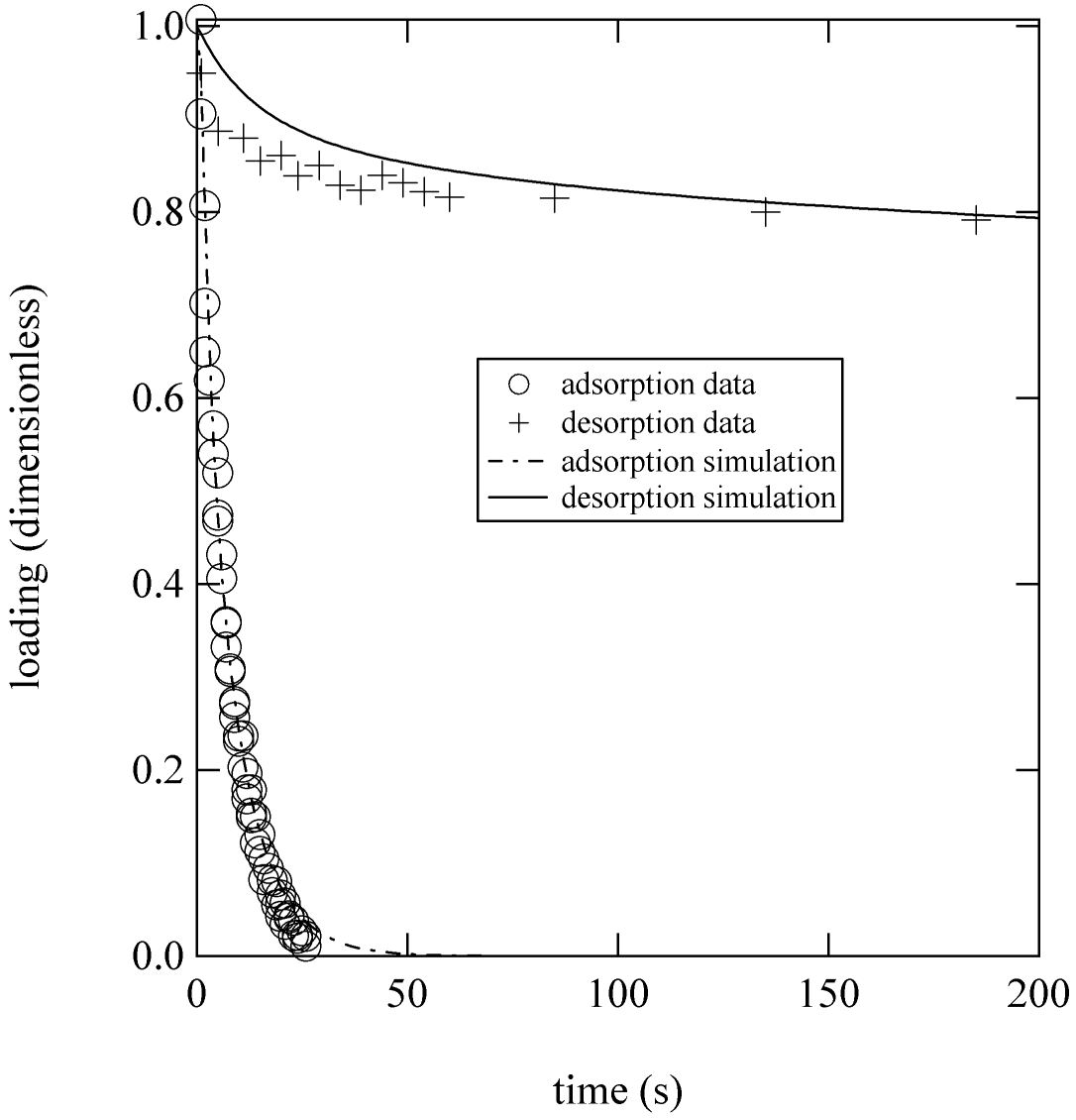

Figure 5-11 Hexane adsorption and desorption on 13X beads at 298 K (Run 10), with non-isothermal microparticle scale model, eq. 5.1-5.3, 5.11, 5.14 and 5.28-5.33.

Table 5.5 Micropore diffusivities from regression of uptake curves with non-isothermal microparticle scale model, eq. 5.1-5.3, 5.11, 5.14 and 5.28-5.33, and literature values.

D_μ/R^2	CE/carbon	6.0×10^{-3} s^{-1}
D_μ	CE/carbon	8.2×10^{-8} cm^2/s
D_μ/R^2	hexane/carbon	5.7×10^{-2} s^{-1}
D_μ	hexane/carbon	7.8×10^{-7} cm^2/s
D_μ/R^2	CE/13X	3.0×10^{-3} s^{-1}
D_μ	CE/13X	4.2×10^{-10} cm^2/s
D_μ/R^2	hexane/13X	9.9×10^{-3} s^{-1}
D_μ	hexane/13X	1.4×10^{-9} cm^2/s
Kapoor and Yang (1991)		
D_μ/R^2	hexane/carbon	8.9×10^{-2} s^{-1}
Do et al. (2001)		
$D_\mu 0$	hexane/carbon	4.23×10^{-8} cm^2/s
Malek and Farooq (1997)		
D_s/R^2	ethane/carbon	4.9×10^{-3} cm^2/s
D_s/R^2	propane/carbon	2.5×10^{-3} cm^2/s
Ruthven (1984)		
D_c	hexane/13X	2×10^{-6} cm^2/s
Sward and LeVan (2003)		
D/R^2	CO_2/carbon	3.4×10^{-1} s^{-1}
D/R^2	O_2/MSC	4.1×10^{-3} s^{-1}
D/R^2	N_2/MSC	1.5×10^{-4} s^{-1}

It is possible to discuss the implication of this rate term for assumed microparticle dimensions. Mantell (1968) describes that activated carbons are formed by the use of binders to re-agglomerate microparticles smaller than 200 mesh (74 μm) where macropores are of equal or greater diameter than the microparticle diameter. Derbyshire et al. (1995) states that microparticles of 5-10 μm diameter are used in activated carbons. Interestingly the crystal size of NaX used by Linde and UOP is less than 10 μm and Davison 3-5 μm as stated by Breck (1974). A microparticle size of 7.5 μm is assumed for both adsorbents considered here. The carbon microparticles are first activated, and then macropores are introduced into the binder by steam activation. The dimensional microparticle diffusivity is $7.3x10^{-10}$ cm^2/s for chloroethane on BPL carbon.

The results obtained here for hexane diffusion on activated carbon are somewhat faster that that reported by Do et al. (2001) on a different material and in good agreement with that report by Kapoor and Yang also on BPL carbon. The rate reported for the dimensional diffusivity of hexane on 13X (Ruthven, 1987) however is considerable faster that that reported here. This result is consistent with the observations of Kumar and Sircar (1986) that zeolite pellets had an additional resistance associated with the skin of binder on the processed pellet versus the crystal, that factor was found to be $3x10^{-3}$ cm^2/s in their case for nitrogen adsorption and $7x10^{-4}$ cm^2/s here. The observed hexane diffusivity is greater here than for chloroethane for both adsorbents, even though the final loading is similar. This could be a result of some steric effects, which would have to be further investigated by examining other adsorption pairs. The results seen here also are consistent with results reported by Malek and Farooq (1997) on ethane and propane obtained from breakthrough experiments and a linear driving force mechanism.

The reproducibility of the experimental system was demonstrated by analyzing the standard deviation obtained from two experiments conducted with the same loading in this case chloroethane and BPL carbon. Figure X presents the adsorption data for these two experiments and the computed standard deviation as a function of time. During initial rapid uptake the deviation is larger, approximately 3%, while at longer times approaching saturation the standard deviation falls to approximately 0.5%.

A sensitivity analysis was conducted of the simulation model to confirm the underlying assumptions. A base case condition was selected, simulation of the uptake of chloroethane on 13X. The loading versus time profile was obtained using a fixed time interval. The simulation was then conducted at the same time profile with a differential change made to the input parameters in order to compute the deviation term for the adsorption step

$$\eta = \frac{\sum abs(n_{new} - n_{base})}{N} \tag{5.42}$$

The parameter sensitivity was defined as

$$\delta = \frac{\partial \eta}{\partial P} P \tag{5.43}$$

A 20% deviation parameters was chosen, derivatives were computed by difference. The results are listed in Table 5.6. The most significant parameter in the shape of the uptake curve is the micropore diffusivity, $\frac{D_\mu}{R_{mp}^{\ 2}}$, more than 10x greater than the next most sensitive parameters, particle diameter and temperature. This confirms the modeling approach and provides confidence in the accuracy of the reported micropore diffusivities.

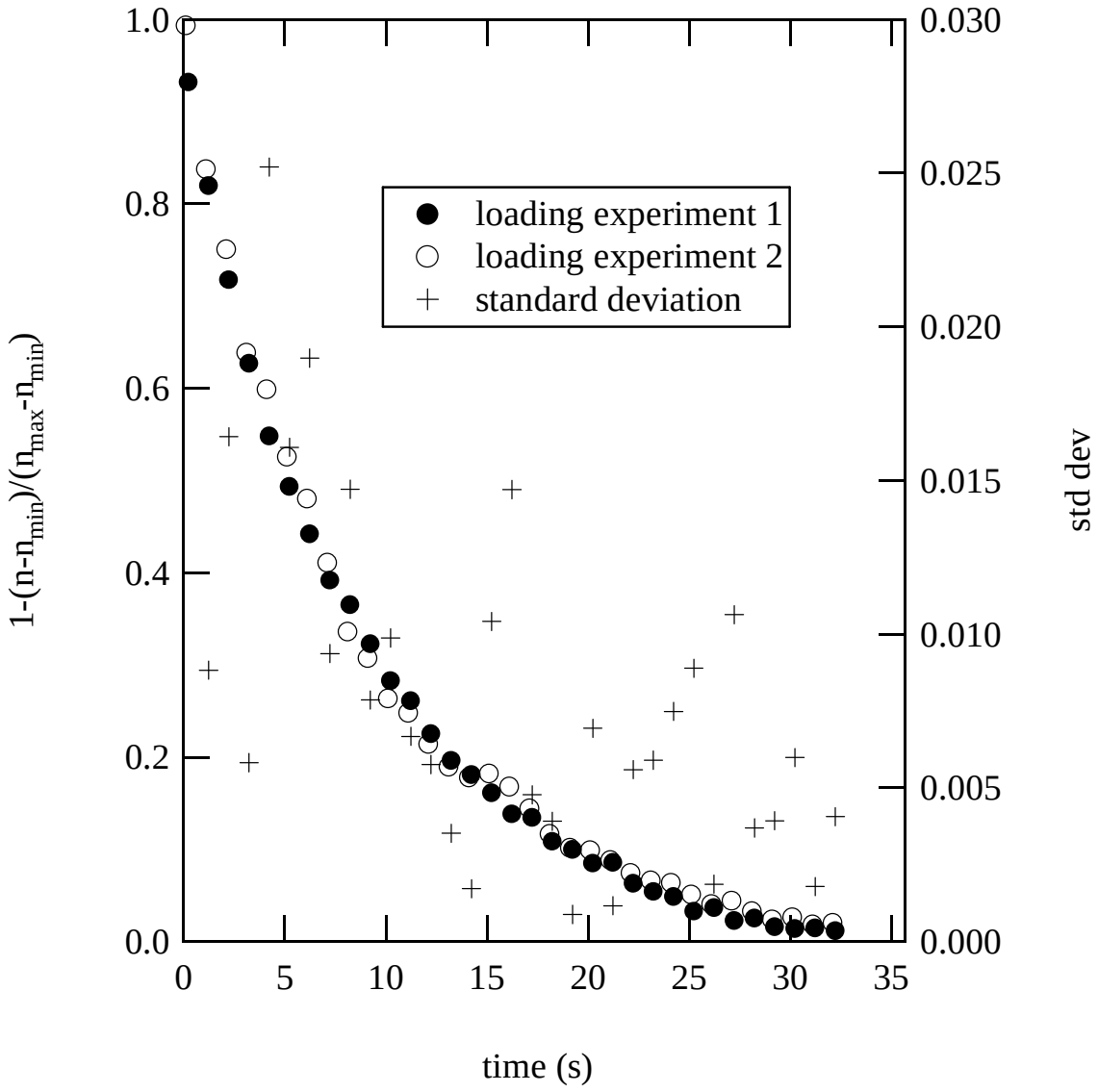

Figure 5-12 Two chloroethane on BPL uptake experiments and computed standard deviation in units of dimensionless loading.

Table 5.6 Sensitivity Values for Uptake Model

	Base Case Parameter Value	δ
$\frac{D_\mu}{R_{mp}^{\ 2}}$ (s^{-1})	0.0030	155
N*	7	0.024
NP**	12	0.003
$\frac{\beta E}{R}$ (K)	3692	4.3
D_p (cm^2/s)	0.3	2.2
N_{Sh}	3.3	1.4
N_{Nu}	2.6	0.35
Bead Diameter (mm)	1.0	11
T (K)	298.4	9.2

*number of collocation points microparticle

**number of collocation points bead

Further work is required to evaluate the rate behavior on activated carbon microparticles. It remains to be determined whether the observed diffusion resistance is associated with the micropore transport or possibly pore blockage of the microparticle due to application of binder, agglomeration and activation of the macropores.

5.6 Conclusions

An apparatus was constructed to conduct vapor phase gravimetric uptake experiments. In addition to weight, concentration and temperature measurements were reported. The results were analyzed by representing both adsorption and desorption behavior on a single plot. An excess of chemical challenge was used to minimize the effect of sample size.

A non-isothermal distributed parameter rate model was used to simulate the uptake behavior. External resistance was modeled using single particle correlations. Internal resistance was described by combined pore and surface diffusion. Excellent agreement between the model and the data are noted for adsorption. Desorption modeling was influenced by purge concentration effects. A surface diffusion coefficient obtained for BPL carbon when described in terms of microparticle dimensions results in a rate term that is of the appropriate magnitude as that typically described by zeolite systems. The micropore diffusion coefficient obtained for hexane was faster than chloroethane on both BPL carbon and 13X. A large discrepancy between the hexane diffusion coefficient on crystals and in a bead suggest the influence of a binder pore blockage.

Chapter 6: Recommendations and Conclusions

There are several major conclusions that can be drawn from this dissertation.

- A novel Type V adsorption model has been developed and shown to provide an analytical solution that was invertible in terms of loading and concentration. The model was shown to provide the correct Henry's Law limit and saturation limit. Correlation of water adsorption data was good for the model that contained only two fit parameters.
- A novel multicomponent adsorption equilibria model was developed. It was based on the enthalpy ratio approach. The effect of pore blocking on water adsorption was introduced using a hysteresis factor. Multicomponent adsorption equilibria data was measured for the system chloroethane and water. The model was shown to correlate the data measured here as well as literature data for adsorption on BPL carbon. No adjustable parameters are required for the model. The accuracy of the model was improved versus earlier models as a result of a better water isotherm correlation.
- Thermal swing adsorption model was developed for multicomponent adsorption of organic and water. An experimental TSA apparatus was described and the results of several experiments with the system of chloroethane and humidity with several activated carbon samples. Results showed that the approach of using one half the temperature difference to initiate the cooling was conservative in terms of cooling time. The model provided excellent agreement with the measured data.
- The uptake measurements provided a convenient method to determine internal particle scale rate parameters. A gravimetric apparatus was constructed to

measure uptake behavior of chloroethane and hexane on activated carbon and 13X molecular sieve. A non-isothermal distributed parameter model was written to describe uptake behavior with a microparticle resistance and microparticle resistance was shown to be the significant internal resistance. The dimensionless diffusivity was obtained by parameter optimization of the uptake curves. The diffusivity was made dimensional using a characteristic microparticle diameter. Comparison of the observed rates was then found to compare favorably with literature values.

Recommendations can be offered for future development of the concepts presented here.

- The Type V isotherm model can be evaluated for the hysteresis scanning curve correlation. An extension of the Type V isotherm model can be developed which solves for scanning curves. Further work is required to create a model that maintains current simplicity but employs parameters with more physical significance.
- The multicomponent model approach of enthalpy ratio should be validated with other data. It proved convenient for the present non-ideal system but it may provide an approach to correlate a wide rate of multicomponent behavior.
- The TSA model should be used compare a variety of heating methods and adsorption affinities. The scaling issues for the present model must be further analyzed especially with regard to heat losses at the column ends.
- The measurement of rate behavior on activated carbon microparticles should be conducted. This will provide a basis for a correct rate model for the activated

carbon systems. It is supposed that similar types of skin resistance will be identified as was discussed for zeolites (Kumar and Sircar (1986)).

References

Ahn, H. and Lee, C., 2003, Adsorption Dynamics of water in layered bed for air-drying tsa process. *A.I.Ch.E. J.*, **49**, 1601-1609.

Barton, S.S., Evans, M.J.B., and MacDonald J.A., 1992, An equation describing water vapor absorption on porous carbon. *Carbon*, **30(1)**, 123-124.

Bonjour, J., Chalfen, J., and Meunier, F., 2002, Temperature swing adsorption process with indirect cooling and heating. *Ind. Eng. Chem.*, **41**, 5802-5811.

Bonnissel, M., Luo, L., Tondeur, D., 2001, Rapid thermal swing adsorption. *Ind. Eng. Chem. Res*., **40**, 2322-2334.

Breck, D.W., (1974), *Zeolite Molecular Sieves*, Wiley-Interscience, New York.

Brennan, J.K., Bandosz, T.J., Thompson, K.T., and Gubbins, K.E., 2001, Water in porous carbons. *Colloids and Surfaces A: Physiochemical and Engineering Aspects*, **187-188**, 539-568.

Chen, A. and Wankat, P., 1991, Scaling rules and intensification of thermal swing adsorption, *A.I.Ch.E. J*., **37**, 785-789.

Choi, J., Do, D.D., and Do, H.D., 2001, Surface diffusion of adsorbed molecules in porous media: Monolayer, multilayer, and capillary condensation regimes, *Ind. Eng. Chem. Res.*, **40**, 4005-4031.

Davis, M.M. and LeVan, M.D., 1987, Equilibrium theory for complete adiabatic adsorption cycles. *AIChE Journal*, **33(3)**, 470-479.

Davis, M.M. and LeVan, M.D., 1989, Experiments on optimization of thermal swing adsorption. *Ind. Eng. Chem. Res*., **28**, 778-785.

Derbyshire, F., Jagtoyen, M. and Thwaites, M., 1995, "Activated Carbons-Production and Applications," in J.W. Patrick (Ed.), Porosity in Carbons Characterization and Applications, Halsted Press, New York. p. 235.

Ding, L.P., and Bhatia, S.K., 2003, Analysis of multicomponent adsorption kinetics on activated carbon. *A.I.Ch.E. J.*, **49**, 883-895.

Do, D.D., Do H.D., 2000, A model for water adsorption on activated carbon. *Carbon*, **38**, 767-773.

Do, H.D., Do, D.D., and Prasetyo, I., 2001, Surface diffusion and adsorption of hydrocarbons in activated carbon. *A.I.Ch.E. J.*, **47**, 2515-2525.

Doong, S.J. and Yang, R.T., 1987, Adsorption of mixtures of water vapor and hydrocarbons by activated carbon beds: thermodynamic model for equilibrium adsorption and adsorber dynamics, Chemical Systems Technology Center for Air Purification Publication No. 8, State University of New York at Buffalo.

Dubinin M.M., Serpinski, V.V., 1981, Isotherm equation for water adsorption by microporous carbonaceous adsorbents, *Carbon*, **19**, 402-403.

Eisseman, R. and Levan, M.D., 1993, Coadsorption of organic compounds and water vapor on BPL activated carbon. 2. 1,1,2-Trichloro-1,2,2-triflouroethane and dichloromethane. *Ind. and Eng. Chem. Res.*, **32**, 2752-2757.

Finlayson, B.A., (1980), *Nonlinear Analysis in Chemical Engineering*, McGraw-Hill, NewYork.

Friday, D.K. and LeVan, M.D., 1985, Hot purge gas regeneration of adsorption beds: Experimental studies. *A.I.Ch.E. J.*, **31**, 1322-1328.

Geankopolis, C., (1983), *Transport Processes and Unit Operations*, 2nd ed., Allyn and Bacon, Boston.

Gilliland, E.R., Baddour, R.F., Parkinson, G.P., and Sladek, K.J., 1974, Diffusion on surfaces. I. Effect of concentration on the diffusivity of physically adsorbed gases. *Ind. and Eng. Chem. Fund.*, **13(2)**, 95-99.

Gregg S.J., Sing K.S.W., (1982), *Adsorption, Surface Area and Porosity*, Academic Press, New York.

Guo, J., Shah, D.B., Talu, O., 1998, "Transport through a single commercial adsorbent pellet/bead by steady-state wilke-kallenbach technique," in F. Meunier (Ed.), Fundamentals of Adsorption 6, Elsevier, New York, NY.

Hassan, N.M., Ghosh, T.K., Hines, A.L., and Loyalka, S.K., 1991, Adsorption of water vapor on bpl activated carbon. *Carbon*, **29(45)**, 681-683.

Hsuen, H.K., 2000, An improved linear driving force approximation for intraparticle adsorption. *Chem. Eng. Sci.*, **55**, 3475-3480.

Hu, X., Do, D.D., Rao, G.N., 1999, Multicomponent adsorption kinetics of gases in activated carbon: effect of pore size distribution. *Langmuir*, **15**, 6428-6437.

Jorge, M., and Seaton, N.A., 2003, Predicting adsorption of water/organic mixtures using molecular simulation. *A.I.Ch.E. J.*, **49**, 2059-2070.

Kapoor, A., and Yang, R.T. 1991, Contribution of concentration-dependent surface diffusion to rate of adsorption. *Chem. Eng. Sci*., **46**, 1995-2000.

Ko, D., and Moon, I., 2002a, Multiobjective optimization of cyclic adsorption processes. *Ind. Eng. Chem.*, **41**, 93-104.

Ko, D., Kim, M., and Moon, I., 2001, Novel thermal swing adsorption process with a cooling jacket for benzene-toluene-p-xylene purification. *Ind. Eng. Chem.*, **40**, 4973-4982.

Ko, D., Moon, I., and Choi, D., 2002b, Analysis of the contact time in a cyclic thermal swing adsorption process. *Ind. Eng. Chem.*, **41**, 1603-1615.

Kodama, K., Kaguei, S. and Wakao,N., 1992, Batch adsorption of trichlortriflouroethane (freon 113) onto activated carbon – surface diffusivity and pore diffusivity. *Can. J. Chem. Eng.*, **70**, 244-249.

Krishna, R. and Wesselingh, J.A., 1997, The maxwell-stefan approach to mass transfer. *Chem. Eng. Sci*., **52(6)**, 861-911.

Kumar, R. and Sircar, S., 1986, Skin resistance for adsorbate mass transfer into extruded adsorbent pellets. *Chem. Eng. Sci.*, **41(9)**, 2215-2223.

LeVan, M.D., 1991, Multiple periodic states for thermal swing adsorption of gas mixtures. *I.E.C. Res.*, **29(4)**, 625-631.

LeVan, M.D. and Croft, D.T., 1995, Determination of periodic states of pressure swing adsorption cycles. *Gas Separation & Purification*, **9**, 13-16.

Linders, M. van der Weijst, M., van Bohhove, J., Kapteijin, F., and Moulijn, J., 2001, Design of an industrial adsorption process with activated carbon for the removal of hexaflouropropylene from wet air. *Ind. Eng. Chem.*, **40**, 3171-3180.

Lodewyckx P, Vansant EF., 1999, Water isotherms of activated carbons with small amounts of surface oxygen. *Carbon*, **37**, 1647-1649.

Mahle JJ, Friday DK., 1989, Water adsorption equilibria on microporous carbons correlated using a modification to the sircar isotherm. *Carbon*, **27(6)**, 835-843.

Mahle, J.J., 1997, A Henry's law limit for the DR and DA equations. *Carbon*, **35**, 432-435.

Malek, A., Farooq, S., 1997, Kinetics of hydrocarbon adsorption on activated carbon and silica gel. *A.I.Ch.E. J.*, **43**, 761-776.

Manes, M., 1983, "Estimation of the Effects of Humidity on the Adsorption on Activated Carbon of the Vapors of Water-Immiscible Organic Liquids," in A.L. Myers, and G. Belfort (Eds.) Fundamentals of Adsorption, Engineering Foundation, New York, 335-344.

Mantell, C.L., (1968), *Carbon and Graphite Handbook*, Wiley-Interscience, New York, p. 223.

Mann R., Yousef, H.N.S., Friday, D.K., Mahle J.J., 1995, Interpretation of water isotherm hysteresis for an activated carbon using stochastic pore networks. *Adsorption*, **1**, 253-264.

McCallum, C.L., Bandosz, T.J., McGrother, S.C., Muller, E.A., and Gubbins K.E., 1999, A molecular model for adsorption of water on activated carbon: comparison of simulation and experiment. *Langmuir*, **15**, 533-544.

Mota, J.P., Rodrigo, A., 2000, Calculations of multicomponent adsorption-column dynamics combining the potential and ideal adsorbed solution theories. *Ind. Eng. Chem. Res*., **39**, 2459-2467.

Petkovska, M., Tonduer, D., Grevillot, G, Granger, J., and Mitrovic, M., 1991, Temperature-swing gas separation with electrothermal desorption step. *Sep. Sci. and Tech*., **26**, 425-444.

Pigorini, G. and LeVan, M.D., 1997, Equilibrium theory for pressure swing adsorption. 2. Purification and enrichment in layered beds. *Ind. Eng. Chem.*, **36(6)**, 2296-2305.

Pre, P., Delage, F, and Le Cloirec, P., 2002, A model to predict the adsorber thermal behavior during treatment of volatile organic compounds onto wet activated carbon. *Environ, Sci., Tech*., **36**, 4681-4688.

Rudisill E.N., Hacskaylo, J.J., LeVan M.D., 1992, Coadsorption of hydrocarbons and water on bpl carbon. *I. and E.C. Res*., **31**, 1122-1130.

Rutherford, S.W. and Do, D.D., 2000, Permeation time lag and heterogeneity in adsorbed phase transport. *Chem. Eng. Sci.*, **55**, 3543-3551.

Rutherford, S.W., 2003, Application of cooperative multimolecular sorption theory for characterization of water adsorption equilibria in carbon. *Carbon*, **41**, 579-625.

Rudisill, E.N., and LeVan, M.D., 1992, Standard states for the adsorbed-solution theory. *Chem. Eng. Sci.*, **47(5)**, 1239-1245.

Russell, B.P. and LeVan, M.D., 1997, Coadsorption of organic compounds and water vapor on BPL activated carbon. 3. Ethane, propane, and mixing rules. *Ind. Eng. Chem.*, **36**, 2380-2389.

Ruthven, D., (1984), *Principles of Adsorption and Adsorption Processes*, Wiley-Interscience, New York.

Salame, I.I., Bandosz, T.J., 1999, Experimental study of water adsorption on activated carbons. *Langmuir*, **15**, 587-593.

Schweiger, T.A.J. and LeVan, M.D., 1993, Steam regeneration of solvent adsorbers. *Ind. and Eng. Chem. Res.*, **32**, 2418-2429.

Sladek, K.J., Gilliland, E.R., and Baddour, R.F., 1974, Diffusion on surfaces. II. Correlation of diffusivities of physically and chemically adsorbed species. *Ind. and Eng. Chem. Fund.*, **13**, 2, 100-105.

Stoeckli, F., Jakubov, T., Lavanchy, A., 1994, Water adsorption in active carbons described by the dubinin-astakhov equation. *J. Chem. Soc. Faraday Trans.*, **90(5)**, 783-786.

Striolo, A., Gubbins, K.E., Gruszkiewicz, M.S., Cole, D.R., Simonson, J.M., Chialvo, A.A., Cummings, P.T., Burchell, T.D., and More, K.L., 2005, Effect of temperature on the adsorption of water in porous carbons. *Langmuir*, **21**, 9457-9467.

Sward, B.K., and LeVan, M.D., (2003), Frequency response measurement of mass transfer rates in adsorbent via pressure perturbation. *Adsorption*, **9**, 37-54.

Talu, O., Meunier, F., 2001, Adsorption of associating molecules in micropores and application to water on carbon. *A.I.Ch.E. J.*, **42(3)**, 809-819.

Taqvi, S.M., Appel, W.S. and LeVan, M.D., 1999, Coadsorption of organic compounds and water on BPL activated carbon. 4. Methanol, ethanol, propanol, butanol, and modeling. *Ind. Eng. Chem. Res.*, **38,** 240-250.

Taqvi, S.M., Vishnoi, A., and LeVan, M.D., 1997, Effect of macropore convection on mass transfer in a bidisperse adsorbent particle. *Adsorption*, **3**, 127-136.

Turov, V.V., Gun'ko, V.M., Leboda, R., Bandosz, T.J., Skubiszewska-Zieba, J., Palijczuk, D., Tomaszewski, W., and Zietek, S., 2002, Influence of organics on the structure of water adsorbed on activated carbons. *J. Coll. Int. Sci.*, **253**, 23-34.

Van Den Broeke, L.J.P. and Krishna, R., 1995, Experimental verification of the maxwell-stefan theory for micropore diffusion. *Chem. Eng. Sci.*, **50**, 2507-2522.

Wankat, P., 1987, Intensification of sorption processes. *Ind. Eng. Chem.*, **26**, 1579-1585.

Yang, R.T., Doong, S.J., 1985, Gas separation by pressure-swing adsorption: A pore diffusion model for bulk separation. *A.I.Ch.E. J.*, **31**, 1829-1842.

Young, D.M., and Crowell, A.D., (1962), *Physical Adsorption of Gases*, Butterworths, London, 64-75.

Zhu, W., Kapeijn, F., Groen, J.C., Linders, M.J.G., and Moulijn, J.A., 2004, Adsorption of butane isomers and SF_6 on kureha activated carbon: 2. Kinetics, 2004, *Langmuir*, **20**, 1704-1710.

Zimny, T., Finqueneisel, G., Cossarutto, L., and Weber, J.V., 2005, Water vapor adsorption on activated carbon preadsorbed with naphthalene. *J. Coll. Int. Sci.*, **285**, 56-60.